Neutral Current Quasi Elastic Selection Study in the ND280 in T2K

Thesis submitted in accordance with the requirements of
the University of Liverpool for the degree of Doctor in Philosophy
by

Michail Lazos

August 2018

Contents

List of Figures

Acknowledgments

Dedicated to Dr. Barry King, to whom without his help and support this Thesis wouldn't exist. He will always be remembered and live in our hearts.

During my PhD, I had encountered personal problems and challenges. My family, was always by my side ready to support me and finish my degree, even though they couldn't understand my study and why this PhD was important. So first I would like to thank my parents Athena and Loukas for their endless help, support and love in my most difficult and desperate moments. They never stopped believing in me and this was giving me strength to continue.

Then I would like to thank my mentor, supervisor and closest person to me Professor Touramanis, for his guidance, advices and help to the end. Without him I wouldn't have the chance to start the PhD. He never stopped believing in me and supported me psychologically all those years of my study.

Then I would like to thank Prof. Neil McCauley for his help and corrections, as he was my main supervisor and he was attending the progress of this Thesis and with his corrections the Thesis was finished on time and was ready for submission.
From the Neutrio Group of the Liverpool University, high energy physics department, I would like to thank Dr. George Christodoulou, for his help from the first day until the day of submission. He was the person I could ask for advice for the day to day problems, and when I didn't know how to proceed.

Lastly, special thanks to Dr. Kostas Mavrokoridis of the Liquid Argon lab,

who helped me stand on my feet and kept me working on my Thesis. Near him I was a co author of a paper and i worked in his lab during my first year of my PhD.

Abstract

The T2K (Tokai to Kamioka) experiment long baseline neutrino experiment (295km baseline) with the goal to measure the neutrino oscillation parameters. To extrapolate the interaction rates, from the near detector ND280, with accuracy, requires precise measurements of these parameters. The ND280 is mainly made of scintillator, while the far detector, Super-Kamiokande, is water Cherenkov detector. Combining the measurements of the two detectors, we eliminate the uncertainties arising from carbon/oxygen differences. The ND280 consists of many sub detectors, and for this analysis the most important are the two Fine Grained Detectors (FGDs), the three Time Projection Chambers (TPCs), and the Electromagnetic Calorimeter (ECal). For the measurement I selected ν Neutral Current Quasi Elastic (NCQE) events, in an exposure of 2.4×10^{20} Protons On Target (POT). In this thesis I study the NCQE events, with a proton in the final stage, and I estimate the number of events to be 425 ± 12.75. The final measurement is the protons to neutrons NCQE ratio, and I predict to be $50.7\% \pm 3.01\%$.

The next generation neutrino detectors are designed underground with big tanks, filled with kilo tons of liquid Argon. They will use the intrinsic properties of the Argon to perform more accurate measurements, than the current detectors. In the LAr lab of the physics department in Liverpool, we have a 90 lt detector and recently finished building the 1ton detector (Ariadne), for research and development. The knowledge and the expertise we get, from our lab, is needed to build the detectors of the future experiments, like DUNE.

Chapter 1

Neutrino Oscillation

1.1 Introduction

The Standard Model (SM) is the most effective theory to describe the forces, the particles, and the interaction among them. According to the SM, the elementary particles, are fermions (like leptons, quarks) and bosons. The quarks make up the hadrons and mesons, which are usually heavier than the leptons. The bosons are force mediators, and there is at least one boson for every force. The SM has six quarks and six leptons, with their antiparticles, in three generations.

Generation	I	II	III
Quarks	u	c	t
Quarks	d	s	b
Neutrinos	ν_e	ν_μ	ν_τ
Leptons	e	μ	τ

The hadrons (like baryons and mesons) are particles consisting of quarks [10]. The baryons,like protons and neutrons, contain three quarks, and the mesons, like B and Kaons, two. There are four forces in nature according to the SM, and every one has an associated carrier particle, although the gravity is not included yet

- The electromagnetic is carried by photons.
- The strong nuclear force by gluons.
- The weak nuclear force is carried by Z^0 and $W^{\pm}$ particles.
- The gravitational force is carried by gravitons. This force is not included in the SM, and until now the graviton has not been discovered.

There are discrete symmetries in nature, those are transformations that preserve the metric and leave the Langrangian invariant.

- Parity operator : Flips the sign of the spatial element of the four-vector.
- Charge conjugation : This operator transforms a particle into its antiparticle without changing momentum or spin.
- Time reversal : It is an operator which reverses the time, momentum and spin.

A Lagrangian of a system which doesn't have only real components will not satisfy the CP symmetry. To have CP violation three generation of fermions are required. By studying decays and interactions we can calculate, with good precision, the CP violation. We know that CP is violated in barions, and we have indications of CP violation in leptons.

The neutrino is a lepton, an elementary sub atomic particle, and three kinds of neutrinos, with their anti-particles, have been discovered until now. The kinds are called flavours, the electron neutrino ν_e, the muon neutrino ν_μ and the tau neutrino ν_τ. The first indication of the existence of this particle was in 1930s, and it was suggested that a neutral particle should exist in order to preserve the conservation of energy in beta decay [11]. First they named this particle neutron, though later Enrico Fermi called it neutrino (small neutron in Italian) as James Chadwick discovered the neutron in 1932.

The neutrino was detected in 1956 by Frederick Reynes and Clyde Cowan while working in the "Project Poltergeist" [12]. They detected the emission of anti-neutrinos from a nuclear reactor via inverse β decay, a method still used today. In the inverse beta decay an anti-neutrino reacts with a proton and gives a positron and a neutron, $\bar{\nu}_e + p \rightarrow e^+ + n$, and Reynes was awarded with the Nobel prize for this discovery. By measuring the energy deposition of the neutron in the detector, and the photons from the positron annihilation with an electron it is possible to reconstruct the energy of the anti-neutrino [13].

Later in 1962 Leon Lederman, Mel Schwartz and Jack Steinberger, after detecting the ν_μ confirmed that the muon neutrino is different than the electron neutrino, in an experiment with the first artificial neutrino beam [14]. In this experiment a pion beam was created which would decay in to neutrinos and a muons. The results had shown, that the neutrinos generated this way were producing only muons when interacting with matter, and the three researchers got the Nobel prize for their discovery. In 2001 the DONUT collaboration observed directly the third neutrino generation, the tau neutrino [15]. In Fermilab, used 800GeV protons, interacted with tungsten beam dump 1m in length, located 36m from the emulsion target direction upstream. The main contribution of the ν_τ is the decay of $D_s \rightarrow \tau + \nu_\tau$. The other particles produced (mostly muons)from the proton interaction were reduced with the use of magnets, concrete and lead shielding.

In the standard model there is no explanation of the mechanism by which neutrinos gain masses (fig 1.2), and until recently neutrinos were considered massless. Now we know that the neutrinos have a very small mass, and the mass difference among the 3 generations is the reason for the oscillation I will explain later (fig 1.2). Also by studying the neutrinos we can understand the lepton CP violation, which is directly related to the matter anti matter asymmetry.

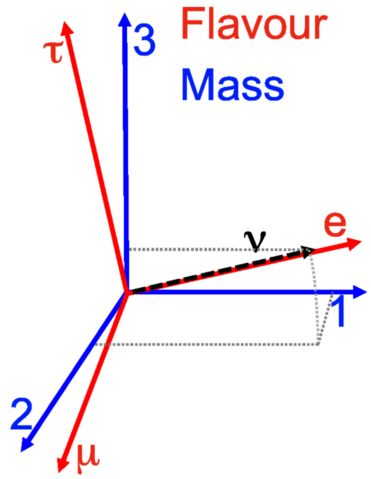

Figure 1.1: The neutrino masses, and flavours, eigenvectors.

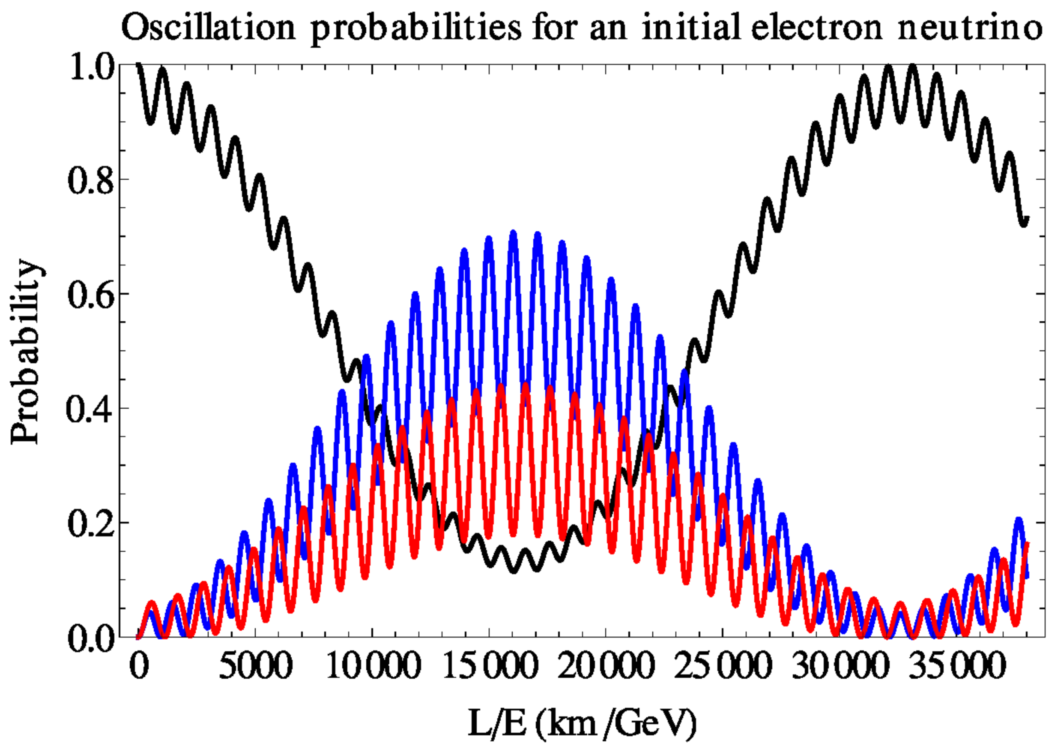

Figure 1.2: The neutrino oscillation in vacuum. The probability, for an electron neutrino to change flavour, versus the distance travelled in vacuum. The x-axis is the distance L, and the y-axis the probability of the neutrino flavour.

1.2 The Solar Neutrino Problem

A by product of the nuclear fusion in the sun are large number of neutrinos. Earth receives huge numbers of high energetic neutrinos, since the main process for the sun to have a hydrostatic equilibrium is through the fusion of two protons (PP chain).

$$
\begin{aligned}
{}^1_1H + {}^1_1H &\rightarrow {}^2_2He + \gamma \\
{}^2_2He &\rightarrow {}^2_1H + e^+ + \nu_e
\end{aligned}
$$

Among the first experiments to study solar neutrinos, was the Solar Neutrino Observatory located in South Dakota (SNO) [16], with the first results in 1964, electron neutrinos were detected, through the inverse beta decay process. The experiment is located about 1.5km underground where the tank with the tetrachloroethylene sits. An atmospheric neutrino interacting with the Cl, creates Ar and electron. the goal was to search for Argon atoms produced by the radioactive source ${}^{37}Ar$ ($\nu_e +^{37} Cl \rightarrow^{37} Ar + e^-(-0.814MeV)$). In 2002 the leader of the experiment Ray Davis was awarded the Nobel prize in physics, for his contribution of the cosmic neutrinos detection. The experiment ended in 1984 and after the analysis of the data, it was found that the standard model predictions were higher than the neutrino flux measured by the detector.

Later the Kamiokande [16] was able to look at the electron neutrino scattering, from solar neutrinos. The detector was built in an old mine and primarily was searching for proton decays. Though the most energetic solar neutrinos can recoil an electron with enough energy to produce Cherenkov light, therefore using the data from the detector was possible to reconstruct the energy and the direction of the event relative to the position of the sun on the sky at that instance. The Super Kamiokande was an upgraded version of the Kamiokande, and the design allowed the study of the atmospheric and the solar neutrinos. The Super-K verified the neutrino deficit coming from the sun.

While the mystery of the solar neutrinos was unsolved, a new experiment

SNO (Sadbury Neutrino Observatory) [17], was built to study solar and atmospheric neutrinos. Through three main processes the SNO was able to search for the missing solar neutrinos.

$$\text{Charged current } \nu + {}^2H \rightarrow 2p + e^-$$
$$\text{Neutral current } \nu + {}^2H \rightarrow \nu + p + n$$
$$\text{Elastic scattering } \nu + e^- \rightarrow \nu + e^-$$

From the above reactions, only the elastic scattering requires an electron neutrino, while the other two can be produced by any neutrino flavour. Therefore it was possible to measure simultaneously the electron neutrino and the total neutrino flux coming from the sun. Also the elastic scattering is very different kinematically, from the neutral and charged current, therefore easy to identify the event. In order to explain the data collected, the neutrino oscillation hypothesis had to be introduced. Knowing the distance to the sun, and the energy of the incoming neutrino it is possible to calculate the probability an electron neutrino to survive. Although the question was not fully answered, the neutrino oscillations provided a good explanation, and verified the neutrino oscillation coming from the sun (fig 1.3).

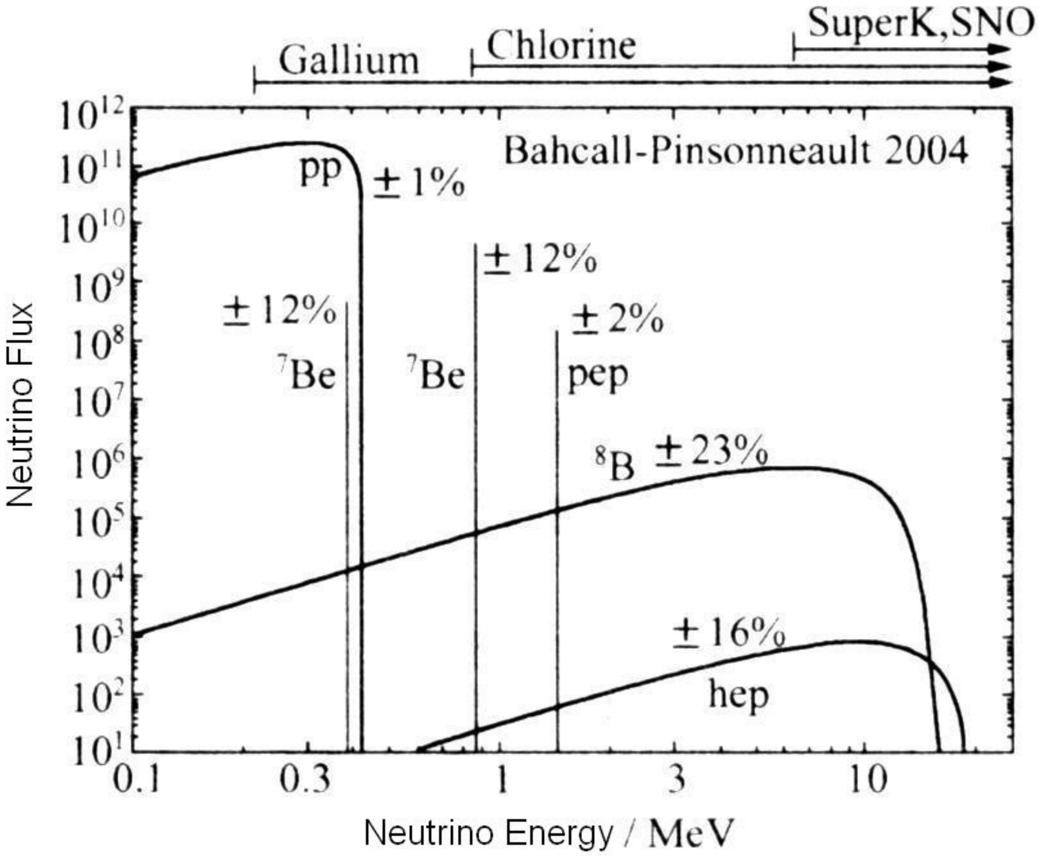

Figure 1.3: The Solar neutrino spectrum derived from theory, displaying the neutrino fluxes and error percentages. The neutrinos released from CNO cycling are not included [1].

1.3 The Atmospheric Neutrino Anomaly

The sun is a natural particle accelerator and produces particles and light that we call solar wind. The solar wind contains high energetic protons, and interact when they meet the Earth's upper atmosphere. From those interactions we get pions, which decay in to muons, and muon neutrinos. Next each of the muons decay in to an electron, and two neutrinos. Thus, from the theory, we expect the ratio ν_μ/ν_e (R-ratio) to be approximately two (fig 1.4).

The experiments studying the atmospheric neutrinos, try to measure this ratio to test the theoretical prediction, with the experimental results (fig 1.6). In the 80's and early 90's we have the first experiments, which measured a very low R-ratio (fig 1.5) which raised many questions [18]. This could mean that either more electron neutrinos were produced or fewer than expected muon neutrinos. Later the Kamiokande gave a precise measurement of the R-ratio, and measured the two neutrino fluxes with respect to directions of the neutrinos which are found to have differences. Then the Super Kamiokande found evidence for the neutrino muon disappearance[19] [20] [21], and verified the theoretical results we get from the two flavour approximation of the neutrino oscillations, where a muon neutrino changes in to a tau neutrino.

$$P_{\nu_\mu \to \nu_\tau}(E,L) = sin^2(2\theta) sin^2(\frac{\Delta m^2 L}{4E}) \tag{1.1}$$

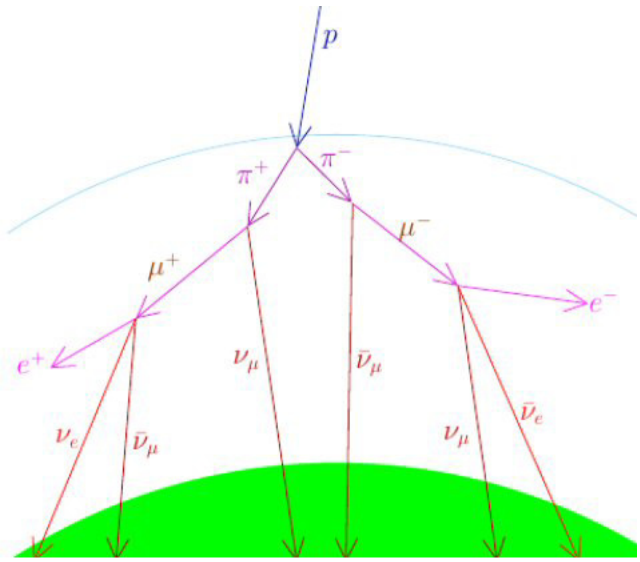

Figure 1.4: How the atmospheric neutrinos are produced.

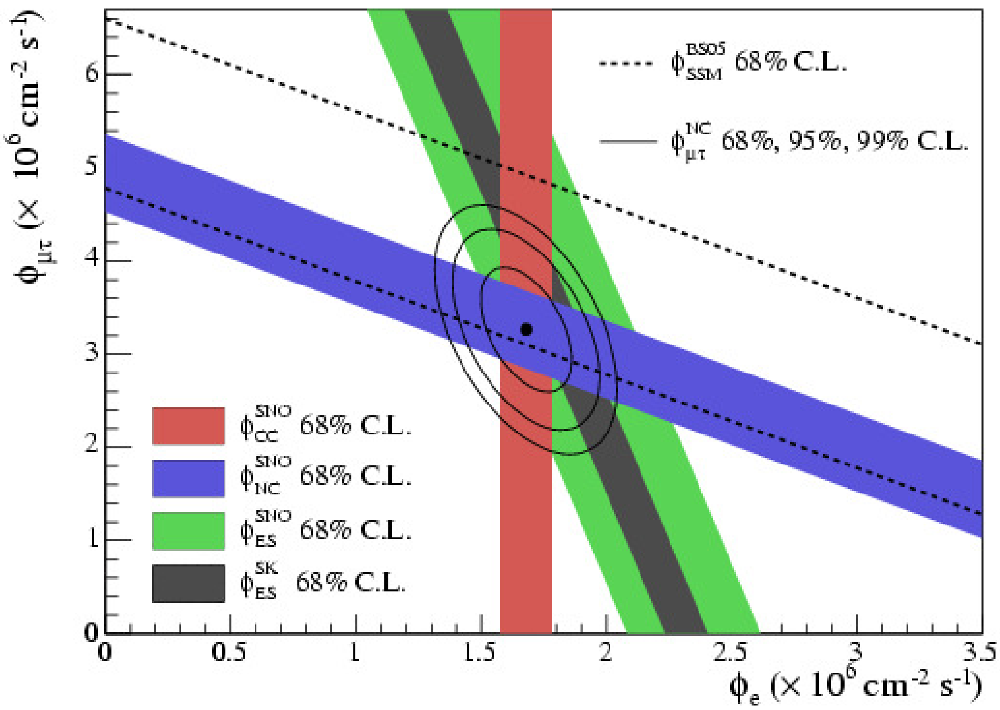

Figure 1.5: The neutrino rate of electron neutrinos versus muon and tau neutrinos. The data are from SNO [2].

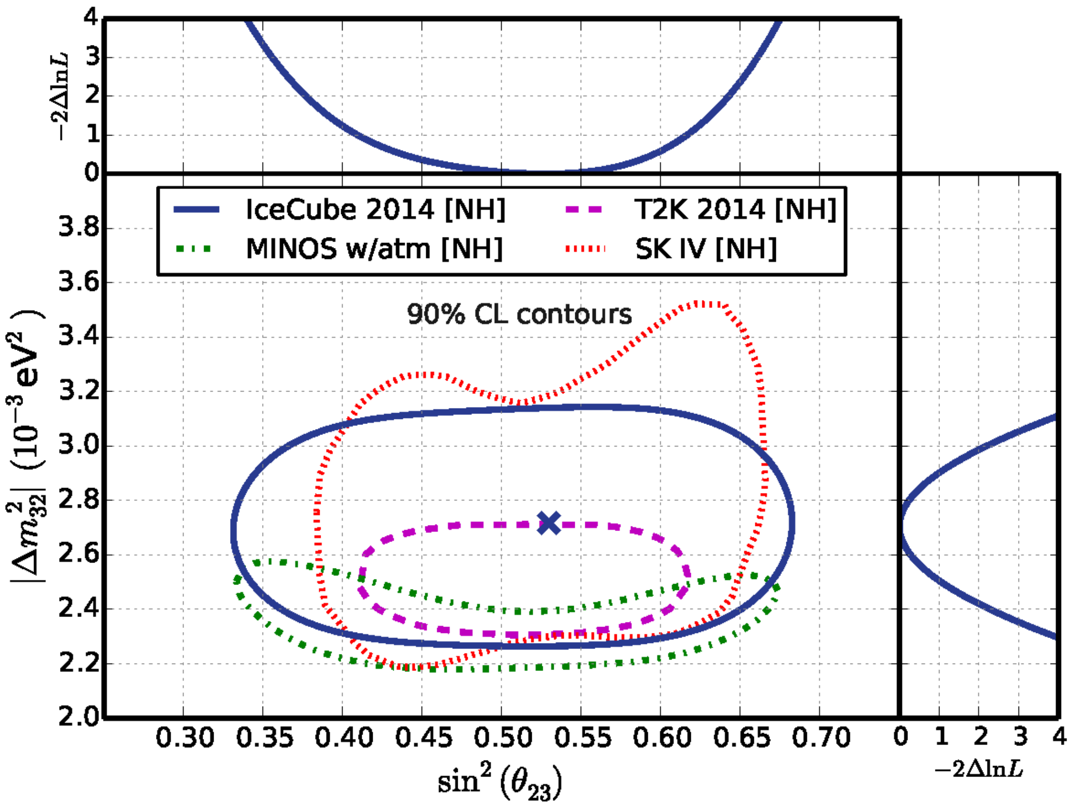

Figure 1.6: The likelihood profiles for the individual oscillation parameters in logarithmic scale. 90% confidence level contours. The normal mass hierarchy is assumed. The image taken from the iceCube collaboration [3].

1.4 The Reactor Neutrino Experiments

One of the by products produced naturally in a nuclear reactor are neutrinos (fig 1.8). During the nuclear fission a neutron is released which decays in to a proton, an electron and a electron antineutrino, $n \to p + e^- + \bar{\nu}_e$ (beta decay). The experiments created to detect those neutrinos use the inverse beta decay, and for low energies, since the mean value of the energy is around 4 MeV. An electron antineutrino reacting with a proton, should give a neutron and a positron, $\bar{\nu}_e + p \to e^+ n$ [22].

Among the first experiments were CHOOZ[23] and Palo Verde [24]. CHOOZ placed an upper limit to the angle θ_{13}, using liquid scintillation enriched with Gadolinium, to have a high neutron capture cross section. The Palo Verde made a precise measurement of the electron antineutrino flux, at a distance of 1km from the cores of the reactors. Neither of those two experiments could confirm, the disappearance of neutrinos though.

Among the current experiments, is Daya Bay [25] located in China, and they use multiple reactors to get their data, so they can reduce the systematics uncertainties and get more precise measurements of the neutrino flux and the energy spectrum. The Super Kamiokande doesn't study the electron neutrino appearance. It was a decision made due to the existing experiments which study this phenomenon.

KamLAND [4] is an experiment in Japan, studying reactor neutrinos, and is located about 180km from the majority of the nuclear reactors, and measured for the first time the disappearance of the electron anti neutrinos. KamLAND confirmed the results observed from the solar neutrinos [20]. Figure (1.7) shows neutrino oscillation results from different experiments.

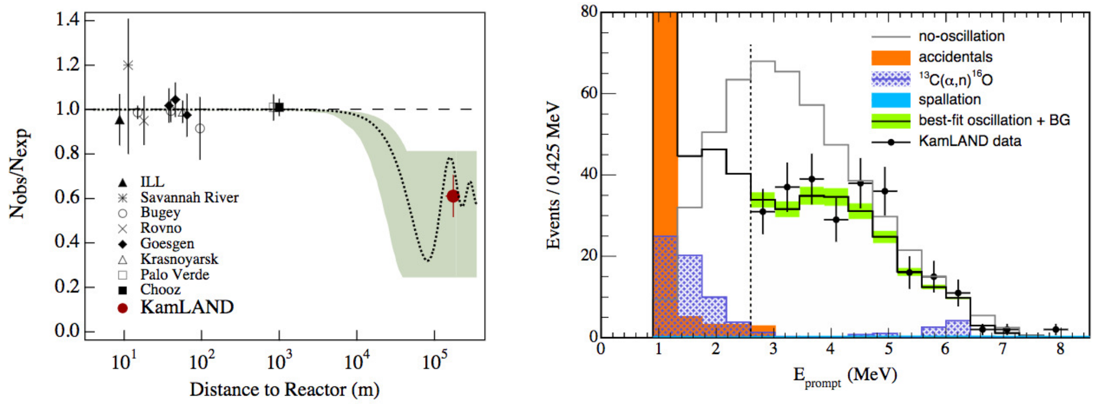

Figure 1.7: On the left we have a summary of all reactor neutrino experiments, displays the ratio of the observed number of neutrino events with respect to the case of no oscillation. The x-axis, is the distance of the detector, from the core of nuclear reactor. On the right results from the KamLAND with the neutrino oscillations measurements, with evidence of spectral distortion. Is displayed also the best fit of the oscillation spectrum with black, together with the energy spectrum [4].

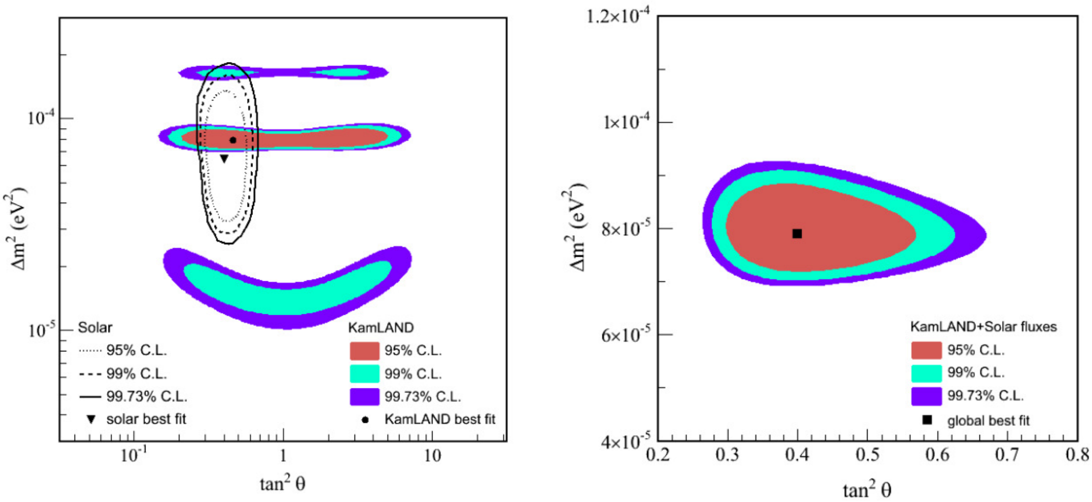

Figure 1.8: The allowed valued for the Δm^2_{12} and θ_{12}, with blue is the best fit assuming CPT. $\Delta m^2 = (7.9^{+0.6}_{-0.5}) \times 10^{-5}\ eV^2$ and $tan^2\theta = 0.4^{+0.1}_{-0.07}$ [4]

1.5 Neutrino Oscillations in Vacuum

Neutrino oscillation is a phenomenon where a neutrino constantly is changing flavours. For example a muon neutrino after travelling some distance has a probability to be detected as electron neutrino. Pontecorvo [26][27], in 1957, proposed this theory first and could reveal new physics if we understand this phenomenon. Also the neutrino oscillation requires the three neutrino flavours to have different masses, and this is already outside the standard model. In addition, in the case of three neutrino flavours we get three mixing angles and a CP violation phase similar to the quarks [28].

In general for a number k neutrino flavours the neutrino state is [29]

$$|\nu(t)\rangle = \sum_{j=1}^{k} U_{aj}^{*} e^{-iE_j t} |\nu_j\rangle \tag{1.2}$$

where $\nu_1, \nu_2, \nu_3, ..., \nu_k$ are the masses of each flavour, and U_{aj}^{*} the mixing matrix. Now the transition probability from one flavour in to another is [30]

$$P(\nu_\alpha \to \nu_\beta) = |\langle \nu_\beta | \nu(t) \rangle|^2 = |U_{\beta j} U_{\alpha j}^{*} e^{-im_j^2 t/2E}|^2 \tag{1.3}$$

If we have two neutrino flavours, the ν_e and ν_μ, the matrix that relates the flavour matrix to the mass basis is

$$U = \begin{pmatrix} cos(\theta) & sin(\theta) \\ -sin(\theta) & cos(\theta) \end{pmatrix} \tag{1.4}$$

where θ is the mixing angle. For example the oscillation probability with baseline L is

$$P(\nu_e \rightarrow \nu_\mu) = sin^2(2\theta) sin^2 \frac{\Delta m^2 L}{4E} \tag{1.5}$$

[30].

In the case of three neutrino flavours the mixing matrix is Pontecorvo-Maki-Nakagawa-Sakata (PMNS) mixing matrix. [28],

$$U = \begin{pmatrix} c_{12}c_{13} & s_{12}c_{13} & s_{13}e^{-i\delta} \\ -s_{12}c_{23} - c_{12}s_{23}s_{13}e^{i\delta} & c_{12}c_{23} - s_{12}s_{23}s_{13}e^{i\delta} & s_{23}c_{13} \\ s_{13}s_{23} - c_{12}c_{23}s_{13}e^{i\delta} & -c_{12}c_{23} - s_{12}c_{23}s_{13}e^{i\delta} & c_{23}c_{13} \end{pmatrix} \tag{1.6}$$

where $c_{ij} = cos(\theta_{ij})$, $s_{ij} = sin(\theta_{ij})$, $(\theta_{12}, \theta_{13}, \theta_{23})$ are the three mixing angles, and δ is the CP-violating phase.

The PMNS matrix can be analysed in to a multiplication of 3 rotation matrices, and each matrix has only one mixing angle. By doing so, we manage to separate the 3 mixing angles with this mathematical manipulation.

$$U = \begin{pmatrix} 1 & 0 & 0 \\ 0 & c_{23} & s_{23} \\ 0 & -s_{23} & c_{23} \end{pmatrix} \begin{pmatrix} c_{13} & 0 & s_{13}e^{i\delta} \\ 0 & 1 & 0 \\ -s_{13}e^{i\delta} & 0 & c_{13} \end{pmatrix} \begin{pmatrix} c_{12} & s_{12} & 0 \\ -s_{12} & c_{12} & 0 \\ 0 & 0 & 1 \end{pmatrix} \tag{1.7}$$

From the solar and the atmospheric neutrino experiments, we have values for the angles θ_{12} and θ_{23} [30], while the θ_{13} is confirmed to be non zero [30], it is possible with future experiments to confirm the CP violation in the leptons, by calculating the complex phase δ.

Three-flavour neutrino oscillation parameters

Parameter	Value	Primary measurement techniques
θ_{12}	$34^\circ \pm 1^\circ$	Solar ν_e disappearance, reactor $\bar{\nu}_e$ disappearance.
θ_{23}	$45^\circ \pm 8^\circ$	Atmospheric ν_μ disappearance, accelerator ν_μ disappearance
θ_{13}	$8.7^\circ \pm 0.4^\circ$	Reactor $\bar{\nu}_e$ disappearance, accelerator ν_e appearance
Δ^2_{21}	$7.5^{+0.19}_{-0.2} \times 10^{-5}\ eV^2$	Reactor $\bar{\nu}_e$ disappearance
Δ^2_{31}	$\pm(2.4 \pm 0.1) \times 10^3\ eV^2$	Accelerator ν_μ disappearance, reactor $\bar{\nu}_e$ disappearance
Δ^2_{32}	—"—	—"—
δ_{CP}	Unknown	Future experiments

In the three neutrino hypothesis, the eigenstates of the neutrino types, can be analysed on the three mass eigenstates with a coefficient matrix.

$$|\nu_i\rangle = \sum_j U_{ji} |\nu_j\rangle \tag{1.8}$$

and after multiplying with the hermitian conjugate, the neutrino types eigenstates have the mass eigenstates as components.

$$|\nu_j\rangle = \sum_i U^*_{ij} |\nu_i\rangle \tag{1.9}$$

Given that CPT is invariant, the flavour of the neutrino is the same with the lepton produced in the same vertex. So the neutrino and the lepton, in the same vertex, must be of the same kind. A neutrino which interacts with a hadron and produces an electron, must be electron neutrino. This is a very useful method to identify neutrino types, by identifying the charged lepton produced by that interaction.

To predict the neutrino oscillations in time, we have to use the time dependent Schrodinger equation for the mass eigenstate, which gives a plane wave solution

[31], $\psi = e^{-iE_k t}$. For this solution, we must assume that the different mass eigenstates, all have the same momentum, though this approximation gives the same result as the difference in the momentum for the different flavours is negligible.

$$|\nu_j(t)\rangle = \sum_i U^*_{ji} e^{-iE_k t} |\nu_i\rangle \tag{1.10}$$

and we need to introduce a second flavour eigenstate ($|\nu_i\rangle = \sum_j U_{ji}|\nu_j\rangle$) so to calculate the transition amplitude, from one flavour to another.

$$|\nu_j(t)\rangle = \sum_k^{e,\mu,\tau} \sum_i U^*_{ji} \psi U_k |\nu_k\rangle \tag{1.11}$$

The mass eigenvectors create an orthonormal basis, and the flavour eigenvectors as well. Therefore the dot product is 1 for parallel vectors and 0 for right angle vectors. Using the Kronecker delta with bra and ket notation, is expressed as $\langle \nu i|\nu_j\rangle = \delta_{ij}$. So the transition amplitude from flavour i to j is

$$A(\nu_i \to \nu_j) = \langle \nu j|\nu_i\rangle = \sum_k U^*_{ik} \psi U_{jk} \tag{1.12}$$

The matrix U^*_{ik}, is the transition amplitude for the neutrino from the state i to k, and the matrix U_{jk}, for state k to j. The ψ is the amplitude for the propagation of the wavefunction. To make the amplitude a probability we square it so we get.

$$P(\nu_i \to \nu_j) = |A(\nu_i \to \nu_j)|^2 = \sum_{km} U^*_{ik} U_{jk} U_{im} U^*_{jm} e^{-i(E_k - E_m)t} \tag{1.13}$$

We will assume relativistic speeds for the neutrinos, in order to make some approximations and simplify the probability amplitude. Since the neutrino masses are very small even compared to electron, can be half a million times smaller, we can assume the energy is the momentum magnitude of the neutrino ($E = |p|$). In addition we assumed a plane wave solution of the Schrodinger equation, therefore all neutrinos come with the same momentum. We know from relativity the total energy (where $c = 1$),

$$E_n = \sqrt{p^2 + m_n^2} = p + \frac{m_k^2}{2p} + O \approx E + \frac{m_n^2}{2E} \tag{1.14}$$

and using Taylor series, we expand it, and we take the two first terms, while the other higher order terms make very small contribution, so for this approximation it is correct to neglect them. Now we can calculate the exponential term of the probability amplitude.

$$E_k - E_m = \frac{m_k^2 - m_m^2}{2E} = \frac{\Delta m_{km}^2}{2E} \tag{1.15}$$

we substitute to the probability function, and we also include the propagation length, $t = L$ for the relativistic neutrino, and the probability becomes a function of the neutrino masses difference, the Energy and the propagation length.

$$P(\nu_i \to \nu_j) = |A(\nu_i \to \nu_j)|^2 = \sum_{km} U_{ik}^* U_{jk} U_{im} U_{jm}^* e^{-i\frac{\Delta m_{km}^2}{2E}L} \tag{1.16}$$

This is a 3 neutrino species hypothesis, and in theory a fourth neutrino might exist, and in that case the mixing matrix is 4×4. An example is the sterile neutrino, a theoretical neutrino which doesn't interact with matter and oscillates like the other three known neutrinos. To make more precise measurements, we need a next generation detector and a very good candidate is the liquid Argon detectors.

A very useful approximation of the probability amplitude, is for two flavours, where we neglect completely the 3rd neutrino kind, and it can be used by experiments which the third neutrino plays almost no role. For example in the atmospheric neutrinos, the electron neutrino can be ignored $\nu_\mu \leftrightarrow \nu_\tau$, while in the solar neutrinos experiments, we have electron neutrinos, and a neutrino in superposition of the muon and tau neutrinos, $\nu_e \leftrightarrow \nu_x$ and x is the superposition of ν_μ and ν_τ. We can do this approximation since the two of the three mass states have very small difference, and the mixing angle θ_{13} is small ($\approx 10^\circ$).

Thus for the two flavour approximation the mixing matrix loses one dimension and becomes two by two.

$$U = \begin{pmatrix} cos(\theta) & sin(\theta) \\ -sin(\theta) & cos(\theta) \end{pmatrix} \tag{1.17}$$

and the probability function is

$$P(\nu_i \to \nu_j) = sin^2(2\theta) sin^2(\frac{\Delta m^2 L}{4E}) \tag{1.18}$$

from that we can derive the probability the initial state remains unchanged, using the fact that the probability for the neutrino to change, and the probability not to change must give one when added. Thus the probability to have an unchanged neutrino is 1 minus the probability to change flavour.

$$P(\nu_i \to \nu_i) = 1 - sin^2(2\theta) sin^2(\frac{\Delta m^2 L}{4E}) \tag{1.19}$$

The last equation is very useful, since we can calculate the L/E parameter which gives maximum probability, and use it to find the optimal distance, from the beam, to place the detector.

The collaboration of the T2K is particularly interested in the disappearance probability of the muon neutrino, $1 - P(\nu_\mu \rightarrow \nu_\mu)$, and the appearance of the electron neutrino, $P(\nu_\mu \rightarrow \nu_e)$, also we don't use the two flavour approximation. The probabilities depend on some unknown parameters, the mixing angle θ_{13}, and the CP violating phase δ. In the mixing matrix the δ is associated with $sin(\theta_{13})$, therefore the T2K can put some constraints to this parameter if the angle θ_{13}, is relatively large. In order to find the mass hierarchy we need a long baseline, and to be sensitive to matter effects, given that the angle θ_{13} is not zero. However the T2K is not sensitive to the matter effects. The amplitude of the neutrino oscillation with matter effects depends on the sign of the neutrino mass ordering. So without sensitivity to the matter effects we can't find the neutrino mass hierarchy.

1.6 Neutrino Oscillations In Matter

The neutrino oscillations in matter can give different results than in vacuum, since the matter can have an effect on the oscillation. When the neutrino scatters with quarks, inside the hadrons, a Z^0 is always exchanged, known as neutral current interaction. This interaction has a small scattering amplitude, independent of the neutrino flavour. On the other hand, the scattering with an electron involves the exchange of a $W^{\pm}$ (charged current), or a Z^0. If the neutrino scattering with the electron is a neutral current then the results are the same regardless of the neutrino flavour, but for the charged current we get different results depending on the neutrino flavour. Therefore in the Hamiltonian we have an extra potential, where G_F is the Fermi constant, E is the neutrino energy and N_e is the density of the electrons in the medium.

$$V_e = \pm\sqrt{2}G_F E N_e \tag{1.20}$$

When neutrinos travel through a medium, the scattering from particles in the medium can change their propagation significantly. If the neutrinos interact with electrons through the charged current they can change flavour, and this mechanism is called MSW [31] (after Mikhaev, Smirnov and Wolfenstein). Also according to MSW mechanism there is a relation between the neutrino interactions with matter, when neutrinos do not change flavour, and neutrino mass mixing. That is due to the electron neutrinos and electron anti neutrinos, having different interactions with matter in comparison to the other neutrino flavours. For the two flavour approximation the Hamiltonian in matter H_m contains an extra term

$$H_m = \frac{\Delta m^2}{4E}\begin{pmatrix} -cos(2\theta) & sin(2\theta) \\ sin(2\theta) & cos(2\theta) \end{pmatrix} + \begin{pmatrix} V_e & 0 \\ 0 & 0 \end{pmatrix} \tag{1.21}$$

We create the $\frac{\Delta m^2}{4E}$ a common factor and the Hamiltonian becomes

$$H_m = \frac{\Delta m^2}{4E} \begin{pmatrix} -cos(2\theta) + A & sin(2\theta) \\ sin(2\theta) & cos(2\theta) - A \end{pmatrix} \tag{1.22}$$

Where $A = \pm\frac{2\sqrt{2}G_F E N_e}{\Delta m^2}$. When the density of the medium is constant the solution of the Schroedinger equation is simple. Using a rotation matrix, we can make diagonal the H_m and derive the mixing matrix and the mass eigenstates. The θ_m is the mixing angle in matter, and the difference of the masses squared is noted as Δm_m^2. So the new Hamiltonian is,

$$H_m = \frac{\Delta m_m^2}{4E} \begin{pmatrix} -cos(2\theta_m) & sin(2\theta_m) \\ sin(2\theta_m) & cos(2\theta_m) - A \end{pmatrix} \tag{1.23}$$

and the oscillation probability

$$H_m = sin^2(2\theta_m) sin^2(\frac{\Delta m_m^2}{4E}) \tag{1.24}$$

By equating the Hamiltonian before and after the transformation we derive the mixing parameters in matter.

$$\Delta m_m^2 = C \Delta m^2 \tag{1.25}$$

$$sin(2\theta_m) = \frac{sin(2\theta)}{C} \tag{1.26}$$

$$C = sqrt(cos(2\theta - A^2) + sin^2(2\theta) \tag{1.27}$$

If we read the parameters carefully, we can see the consequences of the MSW effect. To have observable matter effects, we need either long base lines or very high density of the matter. Also the oscillations can have high amplitude if $cos2\theta = A$, thus $L_v = L_e cos2\theta$. In addition, the oscillation probabilities can be different for the neutrinos and the anti neutrinos due to matter effects (due to the $\pm A$). And lastly if $A > 0$, it depends on the sign of Δm^2, and it can be used to determine the mass hierarchy (fig 1.9).

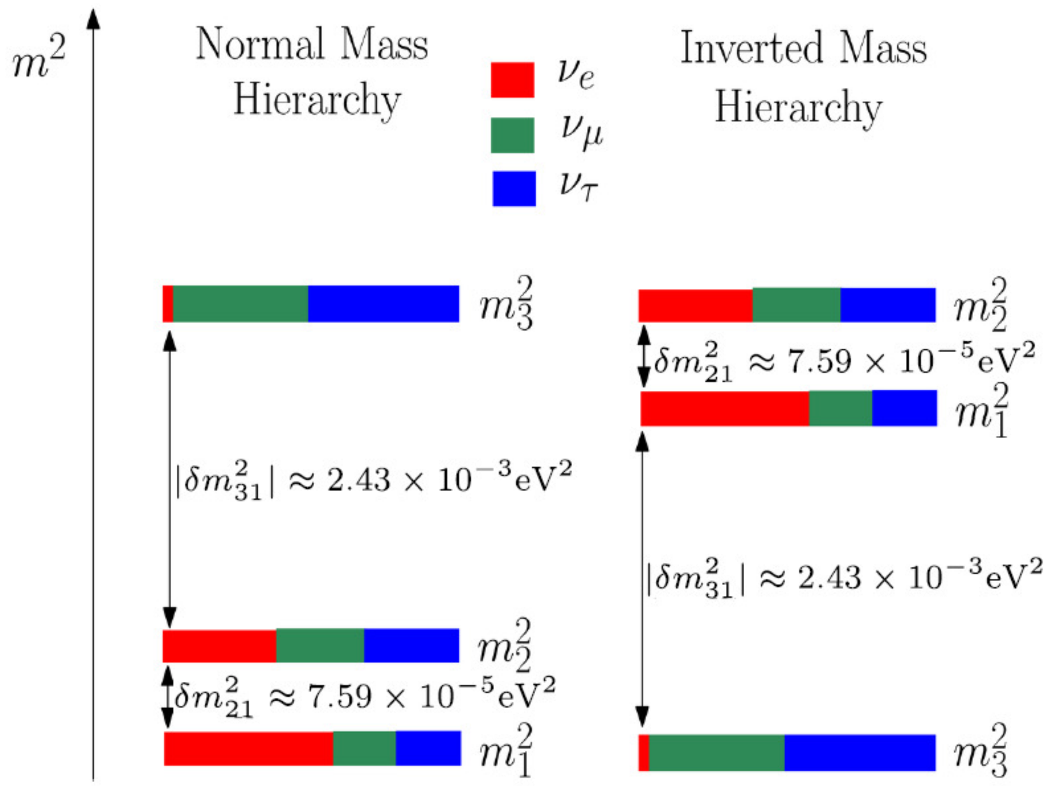

Figure 1.9: The "*normal*" and the "*inverted*" mass hierarchies.

1.7 Sterile and Fourth Generation Neutrinos

According to the results from the neutrino experiments there exist three neutrino flavours, though to explain all the results we must modify the accepted neutrino model. Three neutrino oscillations have been verified [32], the ν_μ neutrino dis-appearance in the atmospheric neutrinos, the ν_e oscillations in the solar neutrinos, and the $\bar{\nu}_e$ appearance in a $\bar{\nu}_\mu$ beam observed by the Liquid Scintillator Neutrino Detector (LSND), a short-baseline, accelerator-based experiment. The oscillations indicate three neutrino masses, although it is not enough to explain all the results.

In order to explain the experimental data we could accept that neutrinos and antineutrinos have different masses, and violate CPT (Charge-Parity-Time) symmetry. In order for CPT to hold, we need an additional generation of neutrinos, which do not interact, and they are often called "sterile neutrinos”. Also one sterile neutrino is not enough to explain the results, therefore at least two are required, each of them with a different mass [32].

In FermiLab the MiniBoone experiment tried to test independently the LSND results, and it did not refute the results, thus more research is required in this field. Since the "sterile neutrinos” do not interact with matter in the detector we should have a deficit, thus we could search for them by comparing neutrino counts between two detectors aligned with a neutrino source. If we find a deficit that would be an indication for sterile neutrinos due to neutrino oscillation. The standard model does not predict another neutrino generation, and such a discovery will expand our knowledge and will reveal NP (New Physics).

Chapter 2

T2K long baseline neutrino oscillation experiment

2.1 The T2K Experiment

For the study of the neutrino oscillations, and in collaboration with the Super Kamiokande, a new facility was built, the T2K, which is a second generation long baseline neutrino experiment situated in Japan. T2K stands for Tokai to Kamioka for the locations of the the near detector and the SuperK (fig 2.1). The near detector has 2.5° off axis angle, with beam energy about $0.7GeV$ at the oscillation maximum for the distance between the detectors which is $295km$. The T2K was completed in 2009 and initially was scheduled to operate for 5 years with a possibility of an extension. We are in 2017 and the experiment is still performing analysis. The near detector has two parts, the INGRID, located on-axis of the neutrino beam, and the off-axis ND280.INGRID monitors the neutrino beam, while ND280 takes precise measurements, and measures various cross sections.

The T2K has three major goals [5] :

- To find the mixing angle θ_{13} by studying the rare oscillations $\nu_{\mu} \rightarrow \nu_{e}$.

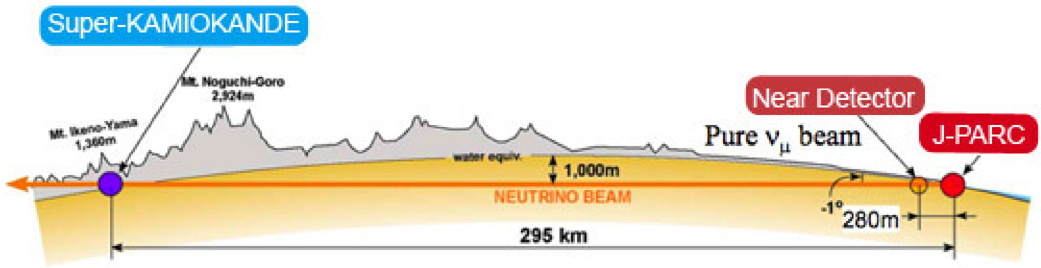

Figure 2.1: T2K

- To get precise measurements of the muon neutrino disappearance, measure the θ_{23} and $|\Delta m^2_{32}|$.
- To find leptonic CP violation if the mixing angle is large enough.

The T2K is using a neutrino beam produced at J-PARC, by hitting protons on a target. From the interaction pions come out which decay in to muons and muon neutrinos. The pions are focused by magnets, called the electromagnetic horns, and they decay inside the decay volume, which is part of the accelerator. Thus a pure muon neutrino beam is created, and by changing the polarity we can produce a muon anti-neutrino beam. Due to muon kinematics the off axis 2.5° angle maximize the flux at the energy of $0.7GeV$, also the background is smaller since there are fewer high energy neutrinos, and last minimize the electron neutrino contamination due to different kinematics [5]. In the next chapter I will describe in detail the off axis near detector ND280.

2.2 The T2K Neutrino Beam at the J-Parc Accelerator Complex

The J-PARC Linear accelerator (LINAC) creates a proton beam with peak energy at 190MeV, then the protons are accelerated at 3 GeV inside the Rapid Cycling Synchrotron (RCS) which enter next. At the last stage the protons enter in to the Proton Synchrotron (PS) and reach the maximum energy of 30 GeV (fig 2.2). Superconducting magnets with two and four poles bent the beam and enters in the arc section. The frequency of the proton pulses is $0.31Hz$, with designed intensity 3.3×10^{14} protons/pulse. The beam is divided in to time spills of length $5.6\mu s$ and every spill is divided in to 8 bunches of νs. For the Run-I there are six bunches while in Run-II there are eight bunches.

The target for the protons is a cylinder made of graphite, in a high pressure, cooled with liquid helium, and dimensions $0.3cm$ by $90cm$. The target is located inside a magnetic horn, out of the three in total, which are used to focus the positive particles, mostly pions and kaons. The produced pions create a focused beam and are sent through a helium tank of one atmosphere, and length $110m$, so to minimise the pion absorption and the tritium production. The pions that do not stop on the walls of the decay volume will produce muon neutrinos. Some muons will also decay producing anti muons neutrinos, contaminating the neutrino beam.

$$\pi^+ \rightarrow \mu^+ + \nu_\mu$$

$$\mu^+ \rightarrow e^+ + \nu_e + \overline{\nu}_\mu$$

A part of the Kaons also will decay and produce electron neutrinos and anti neutrinos adding to the total contamination.

$$K^+ \rightarrow \pi^0 + e^+ + \nu_e$$

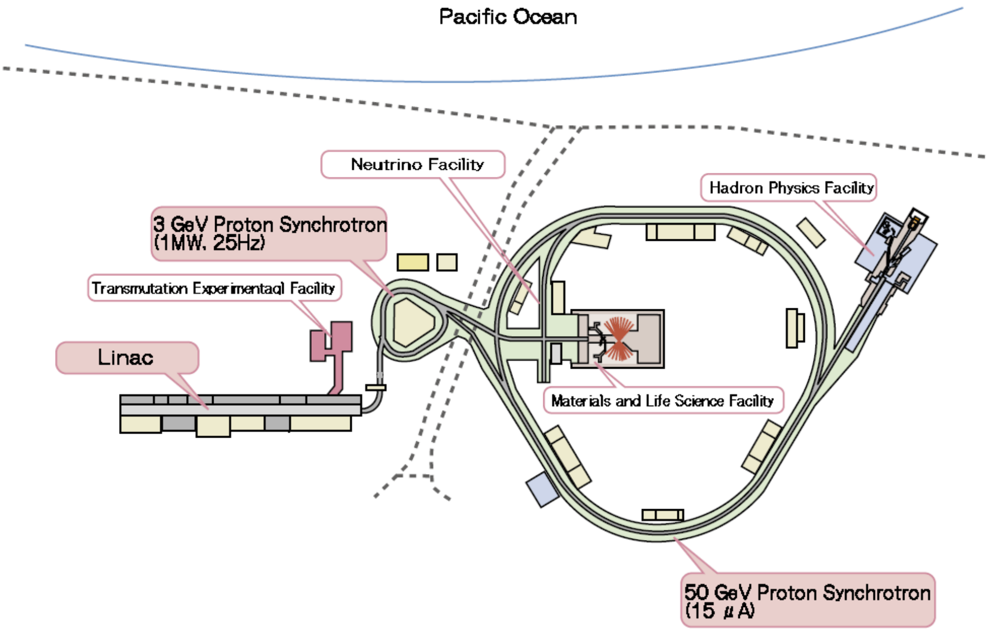

(a) T2K J-PARC

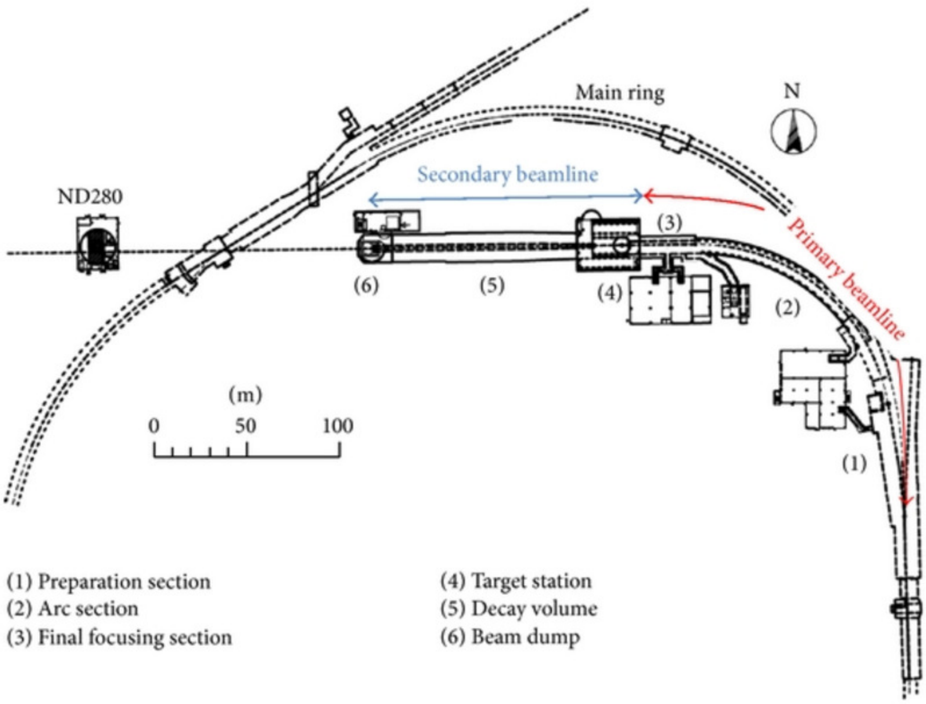

(b) T2K Beam

Figure 2.2: T2K Beam Complex [5].

$$K_L^0 \rightarrow \pi^+ + e^- + \bar{\nu}_e$$

$$K_L^0 \rightarrow \pi^- + e^+ + \nu_e$$

The ν_e contamination at high energies come mostly from the Kaons decay while at lower energies the contamination is created mostly from muon decay. The decay volume has the optimal length for minimum muon decay and maximum pion decay. In order to stop the remaining hadrons that did not decay, graphite blocks are used, with water cooling, through aluminium pipes.

At the end of the beam line, there is the Muon Monitor (MUMON) which is a detector for high energy muons, and it consists of silicon detectors and ionization chambers. This component can be used to monitor the proton and the neutrino beam, and calculate direction. In addition it can be used to check the target and the magnetic horns status. From the calculated kinematics of the pion decay, there is a narrow neutrino beam with peak energy at 0.7 GeV, and off axis angle at 2.5°, and this is the direction of the detector.

2.3 The Far Detector : Super-Kamiokande

The other important part of the T2K experiment is the Super Kamiokande (SK) which is located two hundred and ninety five kilo meters south east of the J-PARC facilities in an old mine, inside the Ike mountain. There is located a big cylindrical tank of forty 41.4 meters height and thirty 39.3 meters in diameter. It is a water Cerenkov detector, which holds 50 kt of water and is the largest in the world.

The detector is composed of two distinct parts, the internal part of the detector and the external. They are separated by plastic sheets and they can both detect events. The internal part is cylindrical with height 36.2, and diameter 33.8 meters. Also a cut of the fiducial volume of 22.5kilo tons, is applied to reduce the background generated by cosmic muon events and the natural radioactivity of the ground around the detector. In addition, if the outer part of the detector records an event without having triggered the components in the internal part, the event is rejected as background, since it was generated outside the detector (fig 2.3).

The Super-K has 11446 photo multipliers (PMTs) installed, each 50.8 cm in diameter, with orientation to the center of the detector. Additionally 1885 PMTs are installed in the outer part of the detector, all facing outwards, with 20.32 *cm* diameter. All the PMTs are connected to the top of the detector where all the electronics, monitors, computers and rooms are located.

The detector is using the Cherenkov radiation to detect particles entering the fiducial volume. A particle with speed higher than the speed of light in a medium (water for T2K), will create a cone of light, which the PMTs will read as rings. The angle of the cone is derived by the refraction formula.

$$cos\theta = \frac{1}{\beta\, n}$$

where $\beta = \frac{u}{c}$, and n is the refraction index (1.34 for water). From observation muons and pions produce sharp rings while the electrons produce a shower, therefore the ring doesn't have well defined edges. Michel electrons from the decay of muons (and pions) can be identified via the time coincidence of the signals, providing further identification of interactions producing muons and pions. The neutral pions decay in to two photons so the shape is different than the muon and electron rings (fig 2.4).

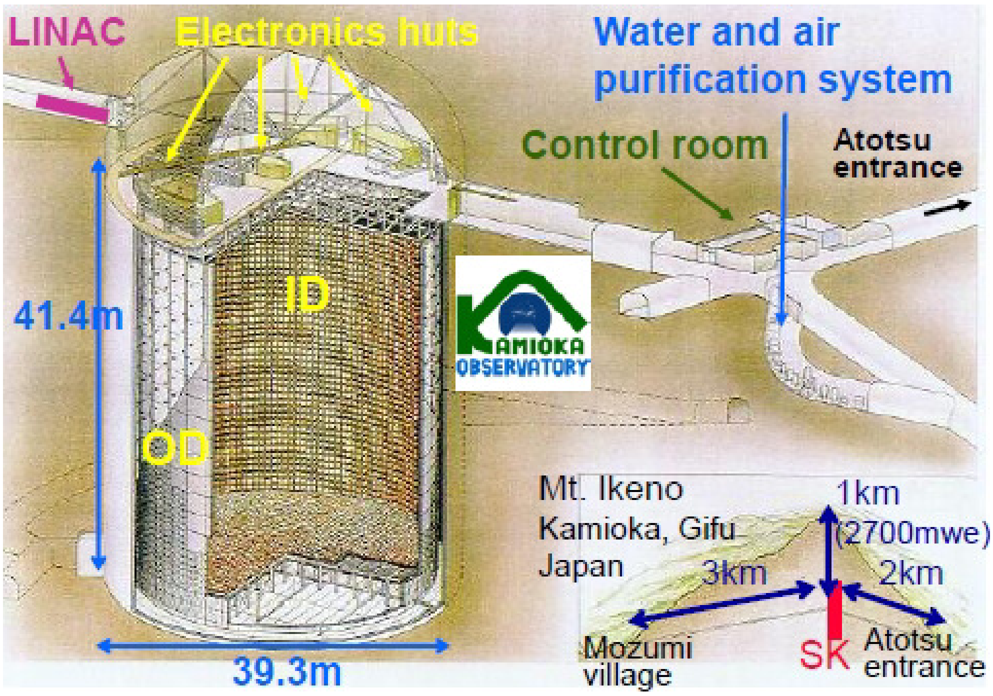

(a) Super-K detector

(b) Inside look of the Super-K

Figure 2.3: Super-K detector [6].

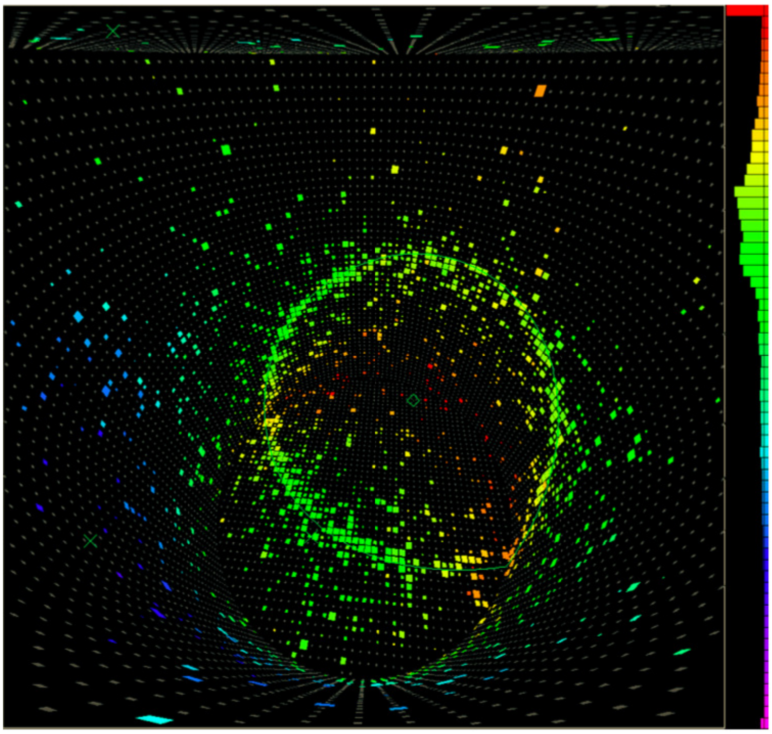

(a) A muon like ring.

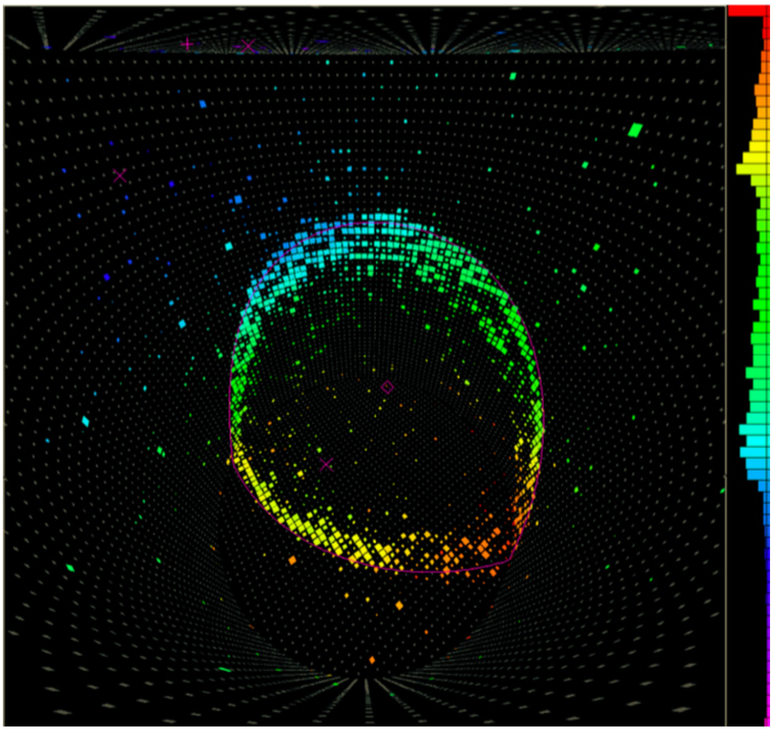

(b) An electron like ring.

Figure 2.4: The muon produces a sharp, well defined ring by emmiting Cerenkov light, as it travels through ultra pure water. Contrary to the electron that creates diffused rings [7].

2.4 The on axis Near Detector, INGRID

Right after the target, on axis, and at distance of two hundred meters away from the target, sits the Interactive Neutrino Grid (INGRID), and is a mosaic of 16 independent detectors forming a seven by seven cross with a double centre, aligned to the neutrino beam (fig 2.6). The last two detectors are placed on the two opposite corners of the cross and the line that connects them passes through the centre. They are placed in this way to check the symmetry of the beam profile.

Each module of the INGRID has 11 layers of plastic scintillating bars that alternate 9 layers of thick iron, forming a cube with each side 1 meter (fig 2.5). The INGRID was made to monitor daily the neutrino beam flux with 1mrad error which is equivalent to 2% of the total neutrino flux of the off-axis spectrum.

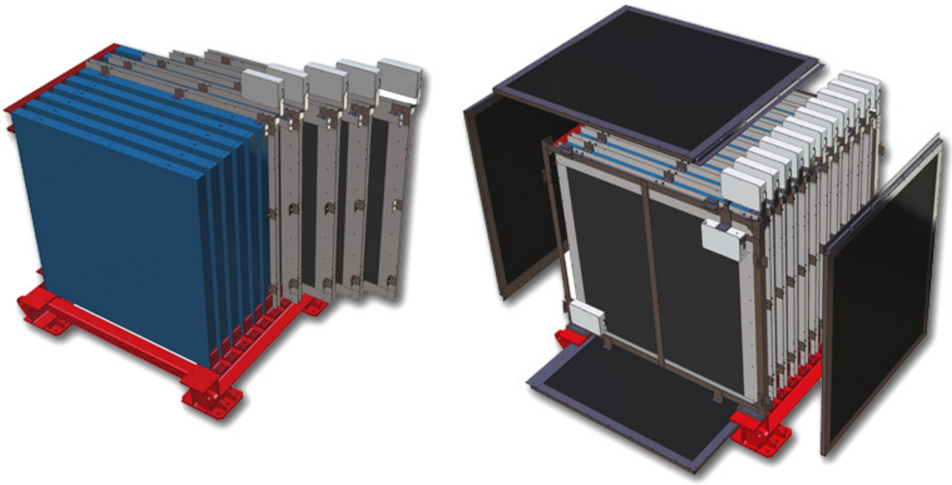

Figure 2.5: INGRID module [5].

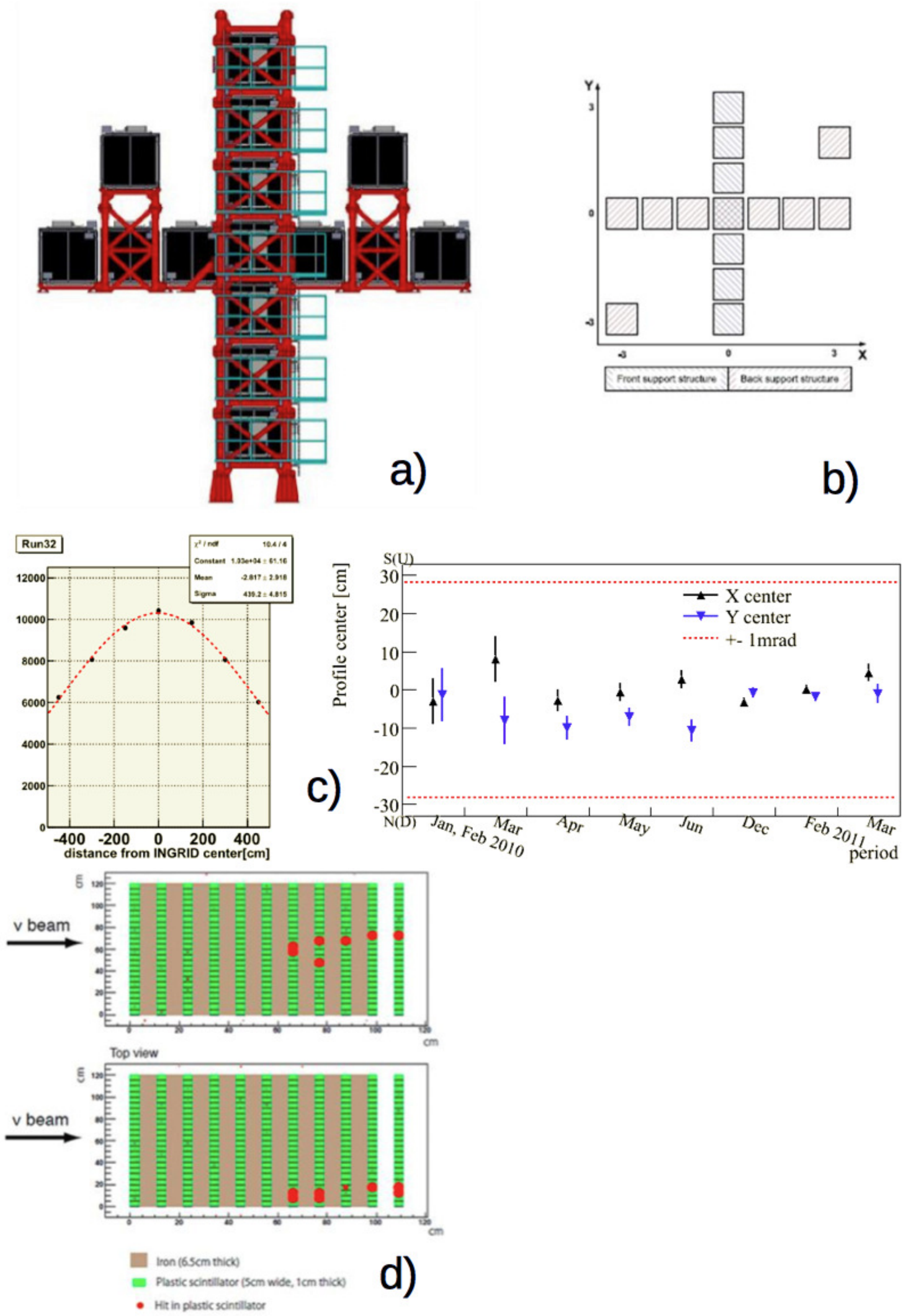

Figure 2.6: INGRID detector. The figure a) shows the positions of the modules. The figure b) shows the cross with the two extra modules positioned opposite to each other. The figure c) is the neutrino beam monitor with respect to time. The figure d) shows the beam direction versus the position from the centre.

2.5 The off axis Near Detector ND280

In this chapter I will describe the off-axis near detector ND280, I will list all the parts, with a short description and their use.

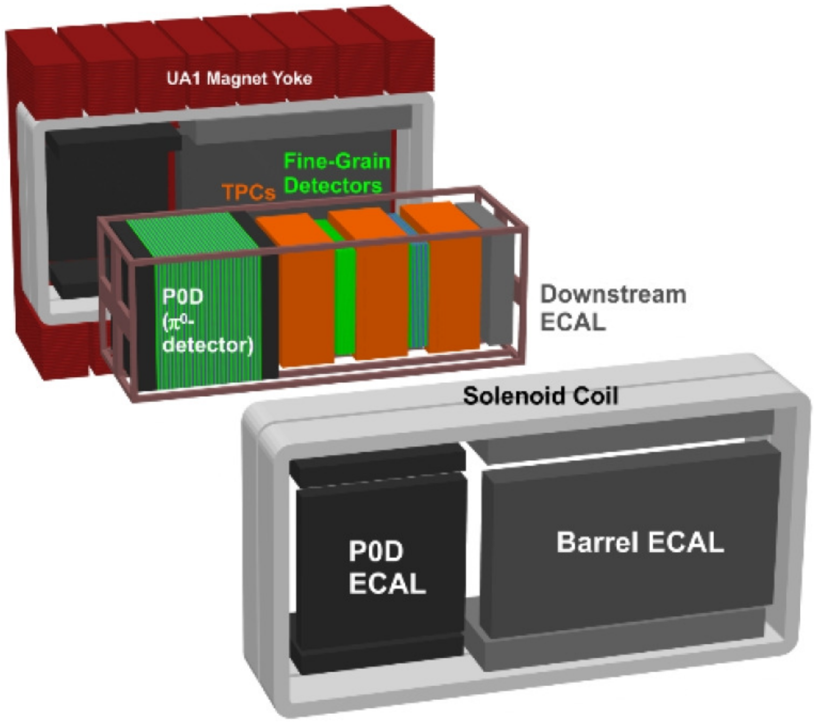

Figure 2.7: ND280 near detector

The components of the detector are illustrated in (fig 2.7) :

- UA1 Magnet
  The magnet is the same type used in CERN, with dimensions $3.5m \times 3.6m \times 7.0m$. It operates at 0.2T to measure the momenta of charged particles produced by neutrino interactions.
- P0D
  This is the Pi-zero detector, it is optimized for the neutral current π_0 interactions, and is measuring the rate. It is a box covered by the calorimeter. It is composed

of plastic scintillating bars with lead foil in between, and has layers of water between the scintillators to measure interactions with oxygen.

- Tracker
  The tracker has two parts :

  1. TPC
     There are three "Time Projection Chambers” that measure the energy loss of charged particles, and measure the momentum of a particle, by tracking the curvature of the particle’s trajectory. Thus we can know the charge and the momentum of a particle, and also by using the Bethe-Bloch formula for the energy loss, the TPC can identify muons, pions and electrons.
  2. FGD
     The "Fine-Grained Detectors” modules are placed between the TPCs and are made of scintillating bars. The first has only scintillating bars, and the second has scintillating bars with water to measure cross section on carbon and water. This component can identify recoil-protons and by using the information from the TPC, can discriminate between charged current and non charged current interactions.

- ECAL
  The "Electromagnetic Calorimeter” is consisted of three parts, the DSECAL (downstream), BRECAL (barrel), and P0DECAL. The calorimeter surrounds the POD and the tracker, is made of Pb scintillators, their main purpose is to measure γ-rays, and it is very important for the reconstruction of the π^0 decays.

- SMRD
  This is the "Side Muon Range Detector", plastic scintillator bars in the sides of the magnet to fill the Air gap and measures the muons at the sides of the detector. Also can identify particle entering in to the detector from the sides so it can identify cosmic particles, and it is also a trigger to calibrate the detector.

2.6 The π^0 Detector (P0D)

The detector for the pions, (P0D, π^0 Detector) (fig 2.8), focusing specifically on the single neutral current (NC) π^0 channel, to measure this cross section. This type of interaction is the major background channel for the Super-Kamiokande analysis to study the ν_e oscillation. By taking two measurements, one with the detector empty and the other filled with water, we can deduce the event rate on water by subtracting the events of the empty detector.

This component of the ND280 is located upstream with dimensions $220 \times 234 \times 242cm$ and consists of a water target area that sits in the middle of two electromagnetic calorimeters. Inside the water are located many distinctive modules. We have 26 tracking modules in total and after every tracking module, a water module follows, with a thin layer of brass, $1.6mm$, for heat dissipation. In addition, in each water module, sit two water tanks. Furthermore inside each electromagnetic calorimeter we have 7 tracking modules, separated with a thick layer of lead, $4mm$ width, and functions as a radiator as well. The lead has a greater stopping power for the particles due to the nature of the element.

Inside the water area, there are modules each with 26 triangular scintillator bars which alternate with water modules. Every bar is $33.6\ cm \times 17.25\ cm$ and the total dimension of each module is $220\ cm \times 234\ cm \times 3.9\ cm$. The P0D can be drained and refilled if needed, so to calculate with more precision the contribution of water to interactions in the fiducial volumes. The scintillator bars create a grid, with horizontal and perpendicular bars, creating a layer. The bars with orientation on the x-axis are 126 while the bars with y-axis orientation are 134. Every layer is separated with a lead foil, acting as radiator. Every two layers are tightened using a PVC frame. The readout of the P0D are MPPCs connected to a TFB board, and the scintillator bars are connected with MPPCs using WLS fibres.

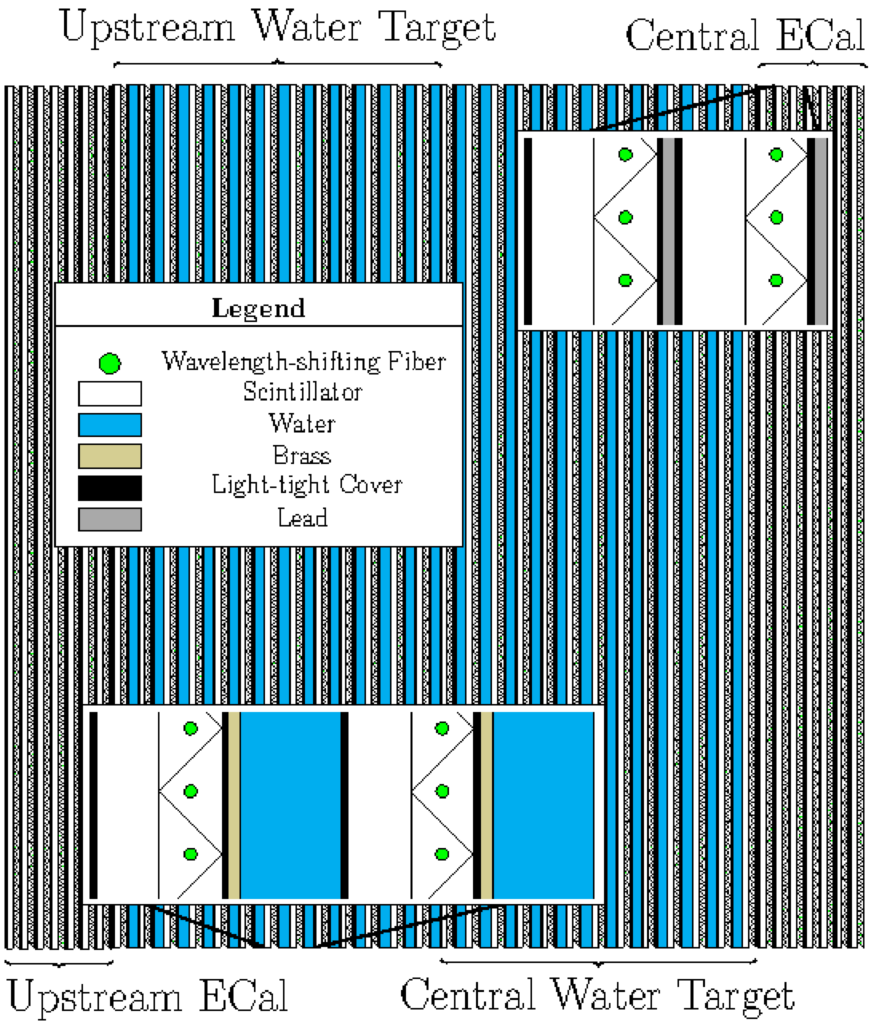

Figure 2.8: Side view of the π^0 detector (P0D) design.

2.7 The Time Projection Chamber (TPC)

For an event reconstruction we need to know the momentum and the Time Projection Chamber (TPC) can measure the momentum of the charged particles inside the magnetic field. From the Bethe-Bloch formula we know the mean energy loss of a particle travelling through a medium. Each type of particle has a distinct curve separated from the others.

$$\frac{dE}{dx} = -4\pi N_A r_e^2 m_e c^2 z^2 \frac{Z}{A\beta^2}(\frac{1}{2}ln\frac{2m_e c^2\beta^2\gamma^2 T_{max}}{I^2} - \beta^2 - \frac{\delta}{2}) \tag{2.1}$$

A charged particle that enters in the TPC will interact with the electrons of the molecules of the gas and by exchanging virtual photons, lose energy. Some of the electrons can produce secondary electrons by interacting with secondary molecules. The escaping electrons coming through this process is called δ-ray.

The spread of a free electron or particle in a vaporous medium is additionally influenced by effects like drift and diffusion. Both drift and diffusion rely upon the electric and magnetic fields while is propagating in the detector. The drift is more apparent to electrons rather to ions, as the ions are heavier and loses energy faster during the collisions thus the distance covered is a lot shorter. The diffusion of the particle velocity is affected by the electric field E, the distance covered l, and the thermal energy ε, and is related to the ratio $\frac{\varepsilon\, l}{E}$, and expresses the deviation from the average velocity (fig 2.10).

The near detector ND280 has three TPCs, filled with gas, each with dimensions $1 \times 2.5 \times 2.5\ m^3$, and are located after the P0D, between the two FGDs and the last before the downstream electromagnetic calorimeter. The TPCs use Argon gas approximately 95%, with impurities CF_4 about 3%, and C_4H_{10} about 2%. The C_4H_{10} gas is there to absorb the high energy photons created by electrons, so to avoid extra ionisation and more photons, and by doing so we reduce the background noise. The second gas, CF_4, helps to increase the drift velocity of the charged particle, while traversing the drift region.

The TPCs have a homogeneous electric field with potential 200 V/cm, and the electrons produced by ionisation are forced to move towards the side walls. Then Micromegas record the charge, thus the electrons, and send the signal to a front-end electronic card (FEC). The Micromegas have a grid 36×48, and each module has an array of pads, with overall dimensions $6.8mm \times 9.7mm$ (fig 2.9).

After the installation of the TPCs, and before to use it, was calibrated using an ultra violet laser with wavelength 266 nm, guiding the light inside the TPC using an optical fibre. It was mounted on the central cathode and produced electrons due to photoelectric effect. Knowing the exact specification of the laser, and the power produced, a real time calibration was possible. Also the distortion of the electro magnetic fields was calculated, along with the relation between the drift velocity with the temperature and pressure and the gain was corrected.

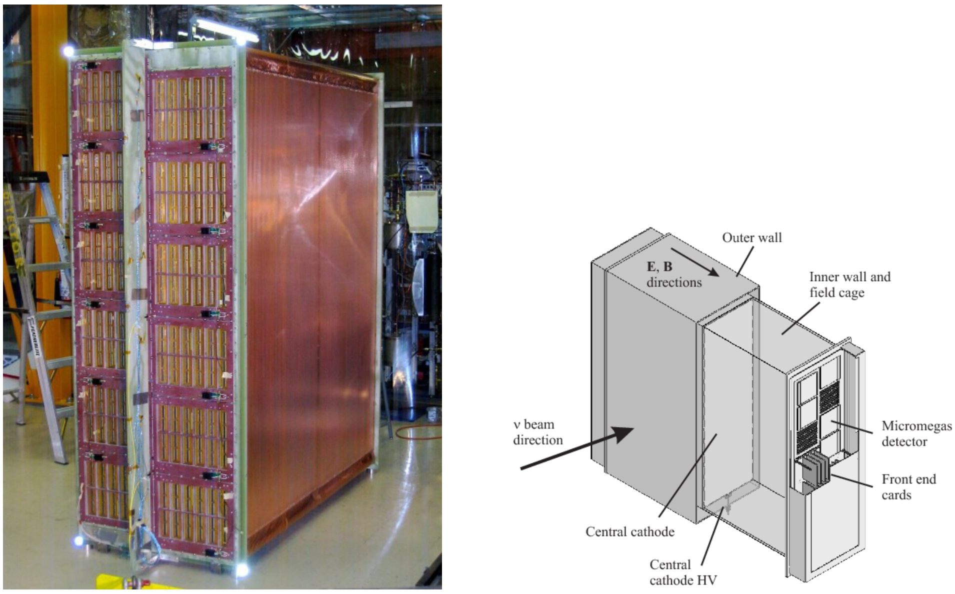

(a) TPC module

(b) TPC deisgn

Figure 2.9: TPC module of the ND280.

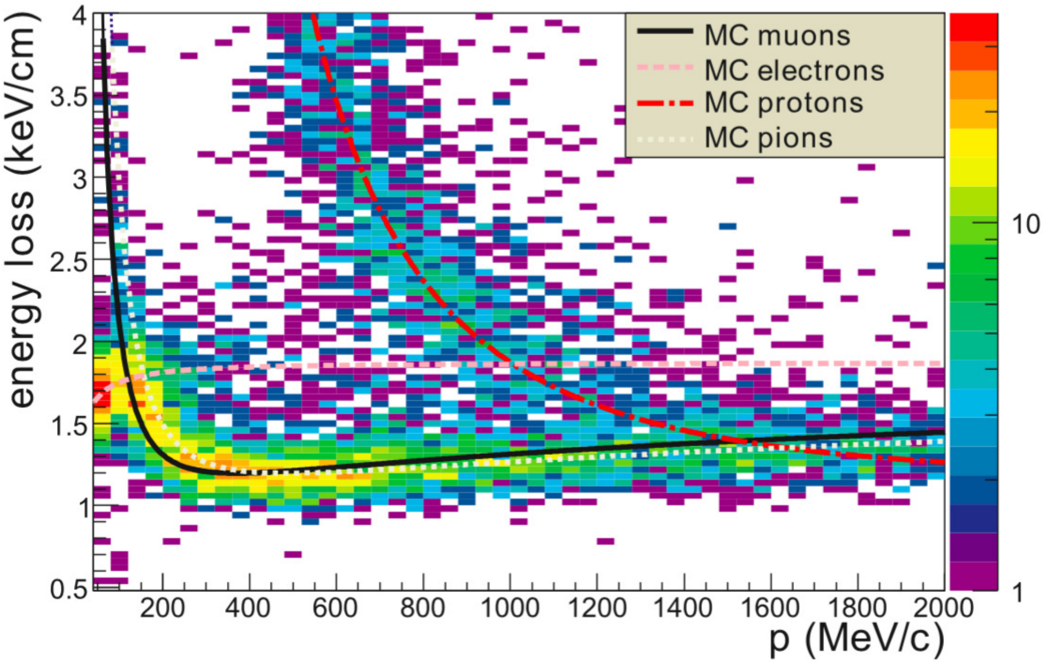

Figure 2.10: The deposited energy from the particle versus the distance travelled inside the TPC, dE/dx. Above 800 MeV/c the TPC can not distinguish the particles, since they all deposit the same energy, the curves for the four particles merge.

2.8 The Fine Grained Detector (FGD)

The part of the detector I use for my analysis, apart from the calorimeters is the Fine Grain Detector (FGD) and is designed to measure particles with small path like protons from recoils. Combining the information from the time projection chambers which follow we can characterize the charged particles created by the neutrino interactions.

There are two FGDs in the ND280, the first is a purely scintillator detector while the second has a part filled with water also. Inside the FGD with the scintillators only, are located 192 horizontal and the same number of vertical bars creating a layer of $X-Y$ grid, and there are 30 layers in total. The dimensions of the scintillator bars are $0.96cm \times 0.96cm \times 184.3cm$, and a WLS fibre is going through each bar, and all the fibres have one end connected to a MPPC which is the read out, and the other end has a mirror made of aluminium to confine the signal.

The other FGD has 6 modules filled with water, each with width $2.5cm$, and has 7 layers of scintillator bars. The dimensions of the two FGDs are the same, $230cm \times 240 \times 36.5cm$, with contained material about 1.1 tonnes approximately. Also for both FGDs the first and the last layer are consisted of scintillator bars (fig 2.11).

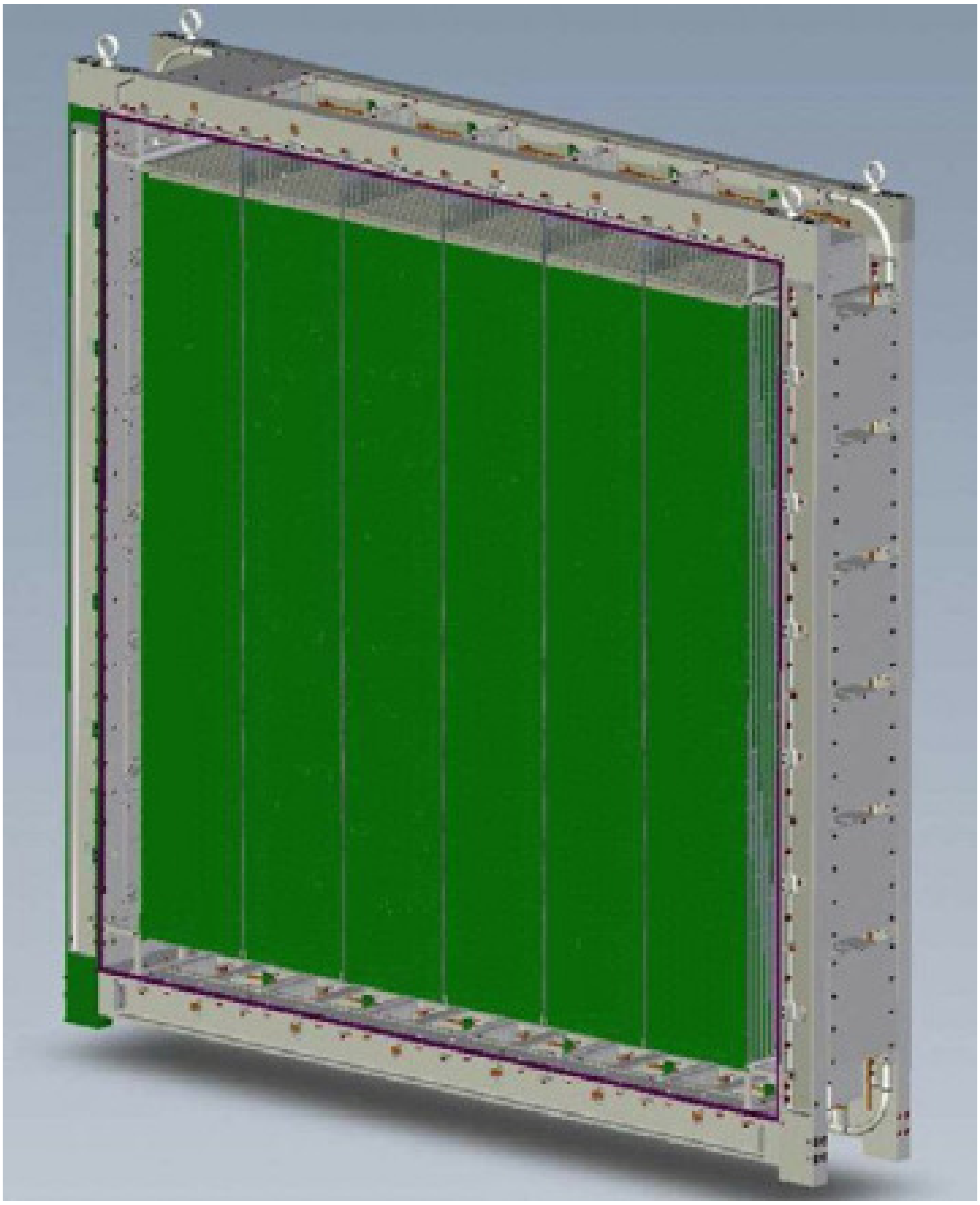

Figure 2.11: Side view of a Fine Grain Detector detector (FGD).

2.9 The Electromagnetic Calorimeters (ECals)

The electromagnetic calorimeter is consisted of three parts. The downstream, (DsECal), the barrel (BrECal) and the P0D electromagnetic calorimeter.

- DsECal This component is at the far end of the ND280 detector, after the last TPC, with direction downstream of the beam. The DsECal is composed of 34 layers with each layer containing 50 scintillator bars. The layers are separated with sheets made of lead and width 1.75 *mm*. Every bar has a wavelength shifting optic fibre, which connects to the MPPC, and all the scrintillator bars in the DsECal have double ended readout. The overall dimension of this module is $2m \times 2m \times 0.5m$. It was the first module to be installed in the basket and plays an important role for the charged current analysis.

- BrECal The construction of this component is similar to the DsECal, but bigger in dimensions, with six modules in total, and are surrounding the region with the FGDs and the TPCs. Half of the layers of each module, are single ended read-out, and the rest are double. The single ended read-out scintillator bars, have one end mirror coated to reflect the light back to the end with the read-out, so to reduce the light loss.

- P0DECAL This part of the detector has six modules in total and sit inside the the magnet's iron yoke, and confine the P0D detector. The construction of each module is similar to the other two parts of the ECal, with scintillator bars forming 6 layers. The layers are separated with 5 sheets of lead and 4 *mm* thickness. The side panels have 58 scintillator bars per layer, while the top and the bottom have 35. The P0DECal has single-end, read out, scintillator bars and the other end has mirror coating. Although, due to the small number of scintillator bar layers, a full π^0 reconstruction is not possible, it can tag the photons coming from the P0D with large opening angles.

2.10 The Side Muon Range Detector (SMRD)

The magnet yoke of the ND280 is a donation of CERN and inside it sits the Side Muon Range Detector (SMRD) a scintillator detector. This part came from the UA1/NOMAD experiment and it's primary task is to measure muon tracks produced from neutrino interactions in the tracker region. In addition it can be used to identify neutrino interactions outside the detector and cosmic muons and can also be used to calibrate the triggering of the ND280. If an event comes from the side and enters the ND280, the SMRD can detect it so it is possible to test the rest of the components while the beam is down.

The SMRD has the shape of the magnet and sits inside the slits of the magnet yoke, which is made of two C shape parts. Each part of the magnet has 8 sections and each section has a scintillator unit of the SMRD, with dimensions 870mm, 170mm and 0.7mm. The SMRD has in total 440 scintillation units and the read out is using MPPCs and WLS fibers (fig 2.14).

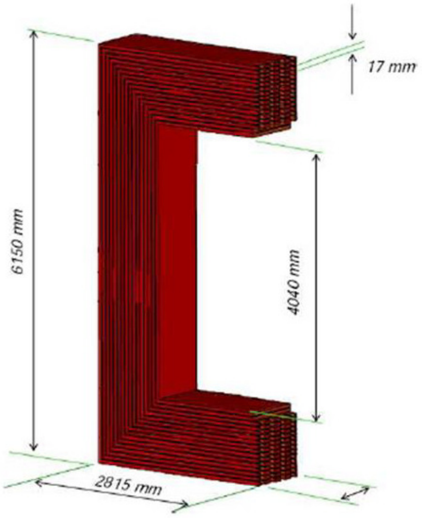

Figure 2.12: SMRD dimensions.

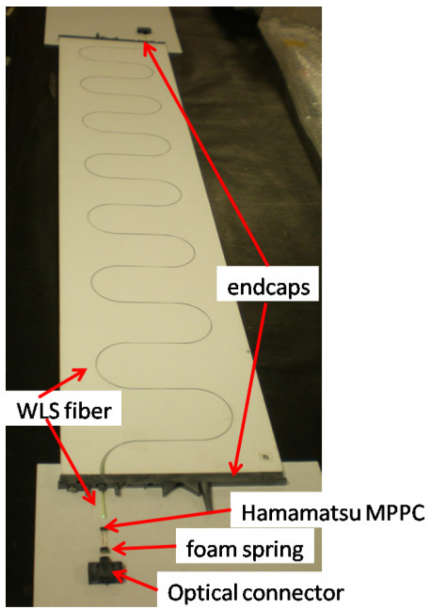

Figure 2.13: Scintillator.

Figure 2.14: SMRD components.

Chapter 3

Signal Selection

3.1 Motivation for the measurement

3.1.1 History of the Weak Neutral Currents

The concept of the weak force carrier, the charged boson, was proposed in 1949 [33], to describe weak interactions. Not until later, in the 1960s, the modern theory, which includes the $W^{\pm}$ and Z^0 bosons for charged and neutral current respectively, was developed (Glashow-Weinberg- Salam) [34] and therefore, realised that the weak neutral current (WNC) was a possible interaction.

The search for this interaction started in the Alternating Gradient Synchotron facility at the Brookhaven National Laboratory (BNL), and in CERN at the Proton Synchrotron facility, with the production of high energy neutrino beams. The results though were discouraging, and the Heavy Liquid Bubble Chamber experiment, placed an upper limit to the $NC/CC < 3\%$ [35].

Until 1973, the Gargamelle experiment at CERN, first observed the NC [36], and later was confirmed by the HPWF experiment (Harvard-Penn-Wisconsin-

Fermilab) at FNAL [37]. The Gargamelle was searching for neutrino and antineutrino, elastic scattering off atomic electrons, at low energies (less than 300 MeV), with the angle, between reconstructed electron direction and the neutrino beam direction, less than 5°.

$$\bar{\nu}_\mu + e^- \rightarrow \bar{\nu}_\mu + e^-, \text{ and}$$
$$\nu_\mu + e^- \rightarrow \nu_\mu + e^-.$$

They managed to detect one event [38], though they needed more than one to prove the existence of this channel. The same experiment found probable events, of neutral current deep inelastic scattering, between a neutrino and a nucleus [39].

$$\nu + N \rightarrow \nu + X, \text{ where X is the hadronic final state [40].}$$

3.1.2 The Neutral Current Elastic Interaction on Free Nucleons

One of the results of the WNC discovery, was that, the neutrino and antineutrino with a proton neutral current elastic scattering (NCEL p fig 3.1), was very useful for looking at the structure of the protons and neutrons (nucleons)

$$\nu + N \rightarrow \nu + N \text{ and,}$$
$$\bar{\nu} + N \rightarrow \bar{\nu} + N$$

This type of interaction is sensitive to the strange quarks inside the nucleons. The first experiments to observe NCEL p scattering were the Columbia-Illinois-Rockefeller, and HPWF [41] [42], in 1976 [43]. Not until the 1980s, the BNL E734 experiment, had relatively high statistics, for the NCEL p, in both neutrinos and antineurinos modes. With the cross section measured, the strange quark contribution to the nucleus spin was evaluated to be [44]

$$\Delta s = -0.21 \pm 0.1 \tag{3.1}$$

.

Later the European Muon Collaboration (EMC) experiment [45], with the proton spin debate, still an unanswered question, brought a lot of interest to measurements of the neutral current elastic channel with a proton in the final state. The more recent experiments are not designed specifically to measure the NCEL p, though both the MiniBooNE, and the SciBooNE had measured this channel with very high statistics. In the T2K until recently there were not many studies [46] on this specific channel and a cross section measurement would be a great contribution to the experiment.

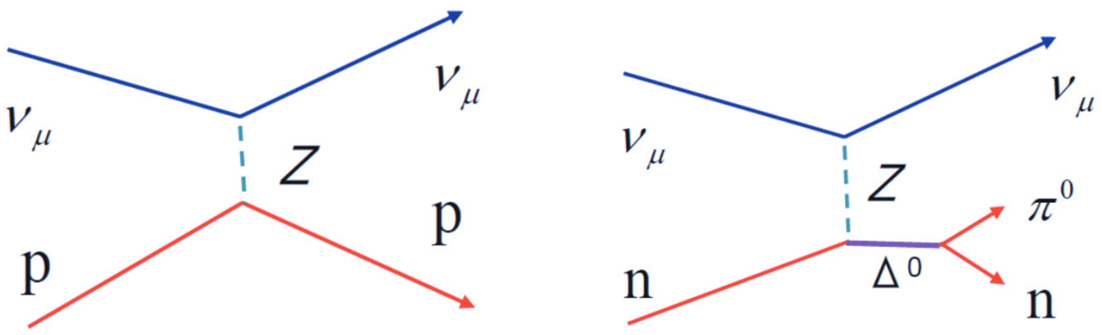

Figure 3.1: The feynman diagrams for the Neutral Current neutrino nucleon scattering.

3.1.3 NCEL Cross Section

The equation for the neutral weak current of the nucleon is,

$$J_\mu = \langle N(p')|F_1(Q^2)\gamma_\mu + F_2(Q^2)\sigma_{\mu\nu}q^\nu + G_A(Q^2)\gamma_\mu\gamma_5|N(p)\rangle \tag{3.2}$$

where the nucleon form factors are $F_1(Q^2)$, $F_2(Q^2)$ and $G_A(Q^2)$ [47] [48]. The first two terms, are the vector part, while the third is the axial vector part. The differential cross section can be written as a function of Q^2,

$$\frac{d\sigma}{dQ^2} = \frac{1}{64\pi E_\nu^2 M_N^2}|J^2| \tag{3.3}$$

the matrix J is the neutral weak current of the nucleon, and the differential cross section in Llewellyn-Smith formalism [49] is

$$\frac{d\sigma}{dQ^2} = \frac{M_N^2 G_F^2}{8\pi E_\nu^2}[A(Q^2) \pm B(Q^2)\frac{s-u}{M_N^2} + C(Q^2)\frac{(s-u)^2}{M_N^4}] \tag{3.4}$$

where $s-u = 4M_N E_\nu - Q^2$, the G_F is the Fermi constant, the sign $+$ is for neutrinos and the $-$ for antineutrinos.

$$A(Q^2) = \frac{Q^2}{M_N^2}[G_A^2(1+\frac{Q^2}{4M_N^2}) - F_1^2(1-\frac{Q^2}{4M_N^2}) + F_2^2(1-\frac{Q^2}{4M_N^2})\frac{Q^2}{4M_N^2} + F_1F_2\frac{Q^2}{M_N^2}] \tag{3.5}$$

$$B(Q^2) = \frac{Q^2}{M_N^2}G_A(F_1+F_2) \tag{3.6}$$

$$C(Q^2) = \frac{1}{4}[G_A^2 + F_1^2 + F_2^2 \frac{Q^2}{4M_N^2}] \quad (3.7)$$

The term $C(Q^2)$ is dominant, at low Q^2 and in terms of the recoil proton energy the Q^2 is,

$$Q^2 = 2M_p T_p \quad (3.8)$$

and T_p is the kinetic energy of the recoil proton. In the ND280, the proton track can be easily separated from the other charged particles, and the kinetic energy can be reconstructed easily using the deposited energy in the calorimeter. In addition, using kinematics we can derive the equation for the energy of the incident neutrino.

In the kinematics diagram of a lepton-nucleus scattering (fig 3.2), the incoming lepton has 4-momentum $K^\mu = (\varepsilon, k)$ and energy $\varepsilon = \sqrt{m^2 + k^2}$. The outgoing lepton has 4-momentum $K'^\mu = (\varepsilon', k')$, and energy $\varepsilon' = \sqrt{m'^2 + k'^2}$. The exchanged vector boson has 4-momentum $Q^\mu = K^\mu - K'^\mu$.

3.1.4 NCEL p Kinematics and Neutrino Energy

In the case of NCEL p, the incoming lepton is a neutrino with negligible mass compared to the proton mass and the energy of the neutrino. The contribution of the neutrino mass to the total relativistic neutrino energy is almost zero, $|m| << |k| \rightarrow m^2 + k^2 \approxeq k^2$, therefore it is safe to assume m, and m' to be equal to zero. In the laboratory frame of reference, the initial nucleus 4-momentum is $P_A^\mu = (M_A^0, 0)$, with the final hadronic state is either a proton or a neutron with 4-momentum $P_{N=p\ or\ n}^\mu = (E_N, \mathbf{p}_N)$, and there is a daughter nucleus, which is not observed, with 4-momentum $P_B^\mu = (E_B, \mathbf{p}_B)$. We have also to include the excitation energy $\varepsilon \equiv E_B - E_B^0$, where

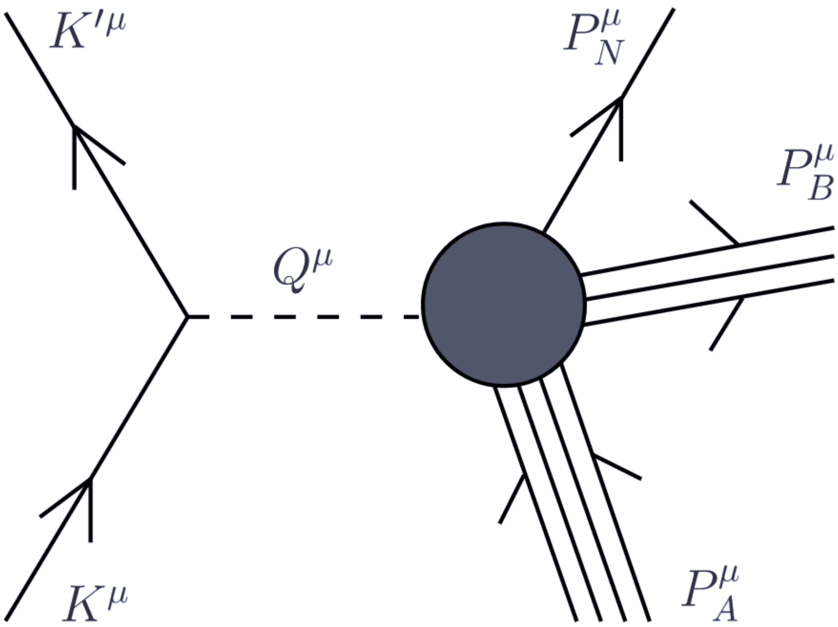

Figure 3.2: The momentum diagram for the Neutral Current Quasi Elastic neutrino nucleon scattering.

$E_B^0 = sqrt(M_B^0)^2 + p^2$, and M_B^0 is the ground state of the residual nucleus, and the missing momentum $\mathbf{p} \equiv -\mathbf{p}_B$.

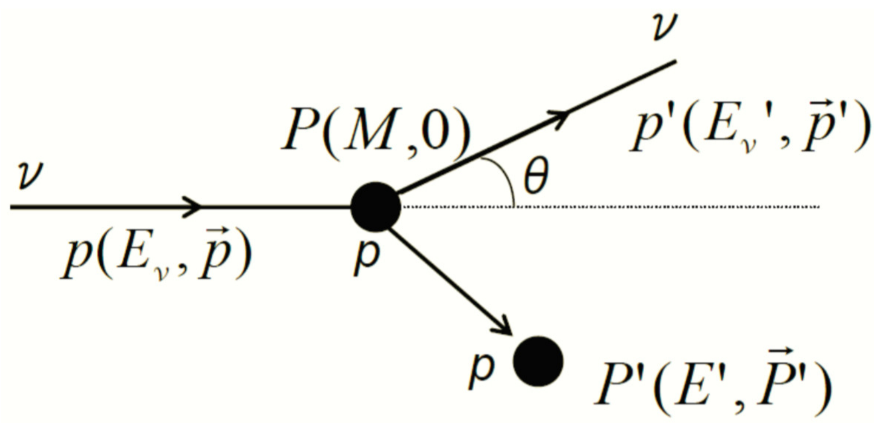

Figure 3.3: The NCEL $\nu p \to \nu p$ scattering, kinematics.

From the kinematics of $\nu p \to \nu p$ scattering (fig 3.3), the 4-momentum of the incoming neutrino is $p = (E_\nu, 0, 0, E_\nu)$ moving on $\overrightarrow{k} - axis$, and for the outgoing neutrino $|\overrightarrow{p}'| = \sqrt{E_\nu^2 - m_\nu^2}$. In the lab frame of reference, and from the 4-momentum transfer, the scattering angle of the proton with respect to $\overrightarrow{k}-axis$, is

$$cos(\theta_p) = -\frac{Q^2 + m_\nu^2 - 2E_\nu E'_\nu}{2E_\nu|\overrightarrow{k}'|}, \tag{3.9}$$

by rearranging and substituting, the energy of the incoming neutrino is,

$$\varepsilon_\nu = -\frac{m_p}{cos(\theta_p)(1+2m_p/T_p)^{1/2} - 1} \tag{3.10}$$

where the angle θ_p is the angle of the outgoing proton, m_p is the proton mass and T_p is the proton kinetic energy, which can be measured from the detector.

3.1.5 Summary

This type of interaction has not been studied thoroughly in the T2K, even though we can derive very interesting results especially by measuring the cross section. Using neutrinos we can derive a value for the strangeness component of the nucleon spin. Also we can reconstruct the neutrino energy by measuring the energy deposited by the recoil proton, thus it can be used to check the neutrino beam. Also because it is an interaction the S-Kamiokande is sensitive to, we can use it to compare the number of events with the ND280, and see if we have differences we can not reconcile. Lastly we can use the results of the cross section to find if there is any deficit in the ND280 spectrum, something we would expect if there was a sterile unknown neutrino.

3.2 Data Sample and Monte Carlo

3.2.1 Data sample

The data in the T2K are divided in to sets, known as physics runs(fig 3.4). Each run, is roughly about one year of operation, and at the end of each run, the J-Parc concludes the annual operation. Usually every year the J-Parc makes improvements to the proton beam thus we have an increase of the energy, so the data each year is different than the previous. In this analysis the data used are from Run II and Run III, and collected from November 2010 until June 2012. The Run I data are not used since it would require to evaluate extra systematics and during that period only the DsECal was installed. Even without Run I, we have enough data and the statistical uncertainty is not affected.

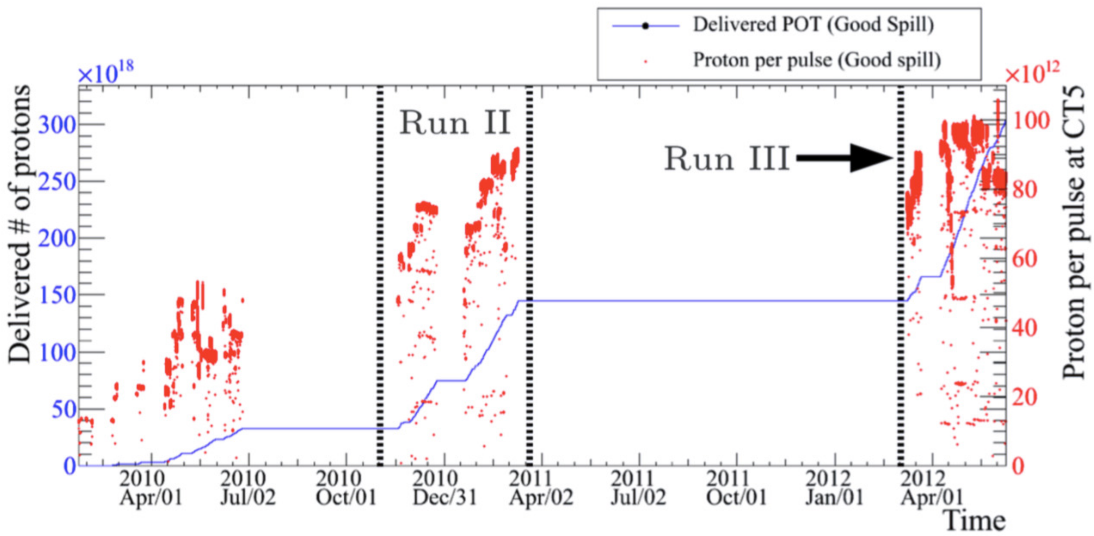

Figure 3.4: The integrated number of POT for the runs I to III, and the number of protons per pulse. The data are from the fifth current transformer (CT5) beam monitor. The image taken from the T2K collaboration.

3.2.2 Data quality requirements

There are some requirements that each beam spill must pass, to be accepted as good quality. First we ensure that the beamline parameters are normal and that the proton beam characteristics are as expected, by checking the beamline monitor data.We want all the hardware components to work properly. The horns currents should be within 5 kA of the mean current value. We want the beam angle not to exceed 1 mrad difference from the mean value, and the total measured, muon yield to be within 5 % of the mean.

In the ND280 we have a dedicated group of specialists, and their duty is to monitor the data quality. They are responsible to provide a boolean flag for each sub detector if they collect good quality data. In this analysis we want all the sub detectors to work properly, except the P0D and the SMRD, which are not used for our selection.

3.2.3 Monte Carlo (MC) Sample

The Monte Carlo data, was created by the NEUT neutrino generator, with 5.5×10^{20} POT (protons on target). The generator, in order to match the characteristics of the physics Run II, simulated a proton beam with 120 kW power. For the Run III, the power of the simulated proton, was 178 kW. The expected interactions for the Run II is 8 per spill, and for the Run III we expect 9.5 neutrino interactions per spill.

3.3 Monte Carlo Study to select NCES events in the ND280

In the chapter of the description of the near detector ND280, we have seen the limitations of the TPCs regarding particle identification. From the "Bethe-Bloch formula" (fig 3.5) we can draw the energy loss curve for each particle and, compare it with the measurement we get from the events. Each particle should have the measured values of the deposited energy, around its expected value. The main drawback using the TPC is that it can identify protons in the momentum range between $[0-900\ MeV/c]$. Above this value the curves for each particle are indistinguishable, the particles p, μ, e, π all deposit the same amount of energy, thus we cant discriminate the proton.

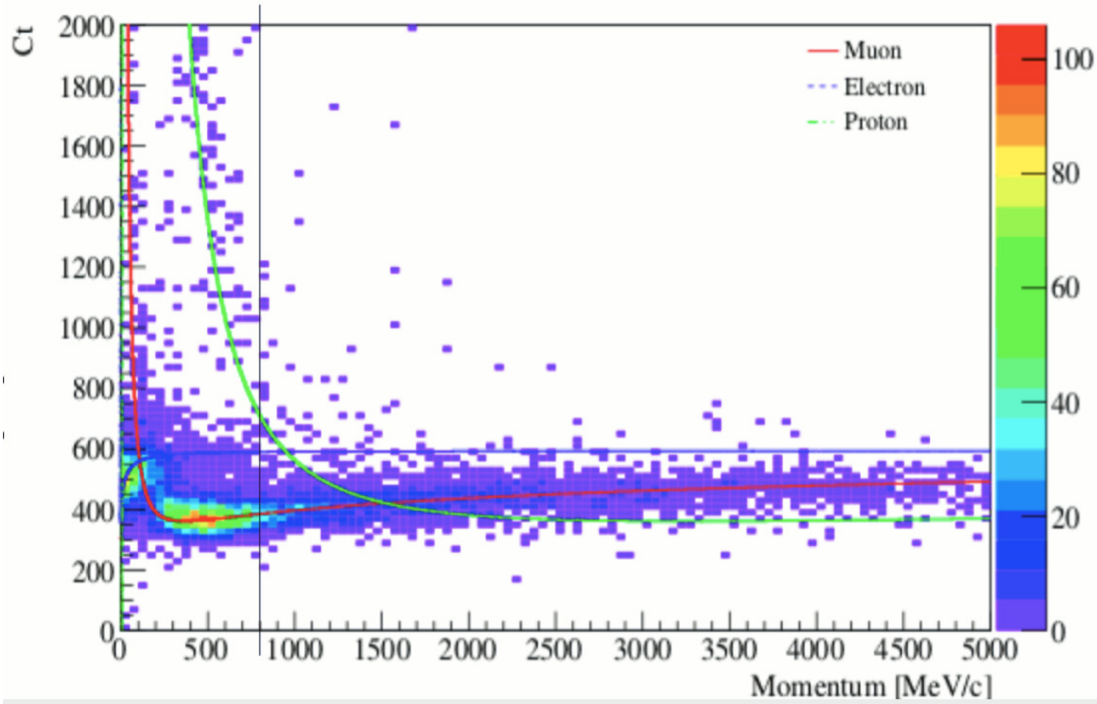

Figure 3.5: The "Bethe-Bloch" energy loss curves for p, μ, e, π.

After studying the MC, for NC interaction with a single proton in the final state, we see that most of the events ($\sim 80\%$) are in the range $[0-900\ MeV/c]$. A simple approach would be to make a hard momentum cut and ignore the events outside that region, but we lose data, and since the NC channel already is only a small fraction

($\sim 7\%$, table~3.1) of all the interactions, we decided to use the ECal for the protons with higher momentum (900 MeV/c and above). Using the ECal we can reduce the background and obtain a clean signal in all momentum range. Thus we will have two regions in our momentum spectrum, for $[0 - 900\ MeV/c]$ we can use the TPC and for 900 MeV/c and above the ECal with the Neural Network (fig 3.6) (Chapter 4).

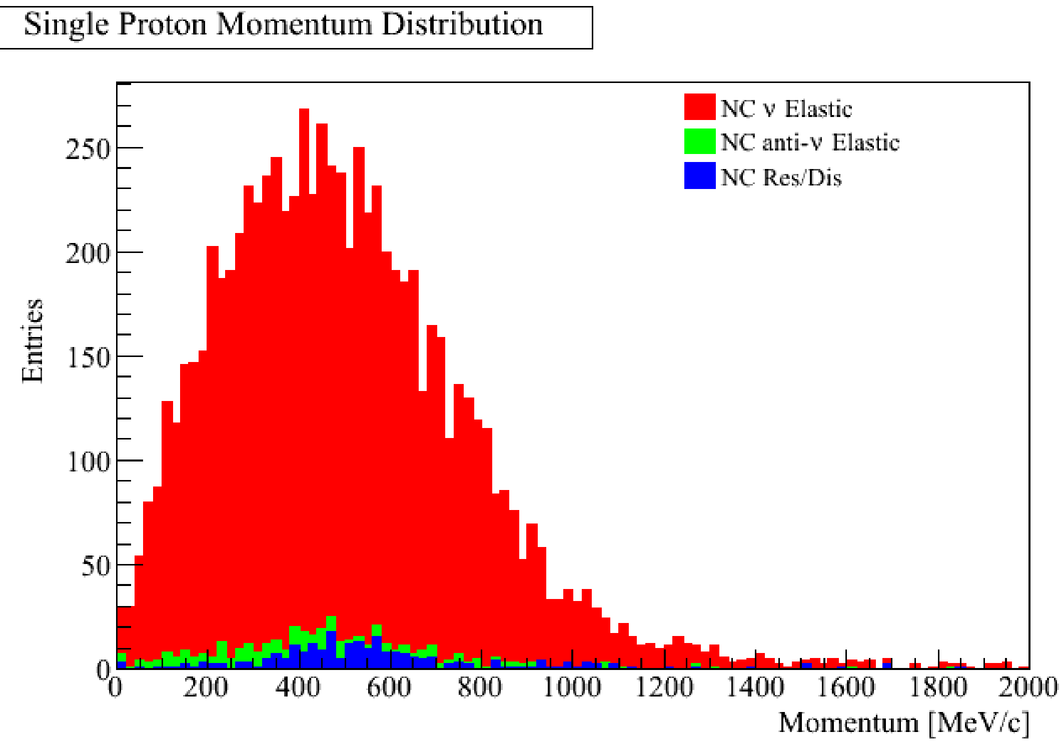

Figure 3.6: The MC momentum histogram, for single proton NC interaction.

The signal we are studying should be a single track (fig 3.7) without any other secondary particles, and in time with the beam. We run the analysis in each time bunch separately, so we do not mix events from different time bunches. We want a good reconstructed single and positive track (since we look for protons with positive charge), with the vertex in the FGD, and one track per vertex. In addition we do not want unclassified, or backward tracks, and no Michel electrons since the last is an indication we are not looking at a proton. Furthermore we want the event to stop inside the detector, thus the ECal layers with activity should be less than 30. Lastly we have to apply some cuts in the fiducial volume in order not to have bad reconstructed events, and those are the standard cuts everyone has to use in the T2K collaboration not

Table 3.1: Results for ν_μ GENIE generator for 4.46×10^{20} protons on target. For the NCQE Data, the events are between 400-500.

Neutral Current (NC)	Charged Current (CC)
Quasi Elastic (QES) neutrons 8.9%	Quasi Elastic (QES) 37.7%
Quasi Elastic (QES) protons 7.5%	
Resonance (RES) 7.4%	Resonance (RES) 19.9%
Deep Inelastic Scattering (DIS) 4.7%	Deep Inelastic Scattering (DIS) 13.8%
Coherent (COH) 0.31%	Coherent (COH) 0.41%

to have discrepancies in the different studies. This analysis is blind, and the expected number of events for the NCQE data are 400 to 500.

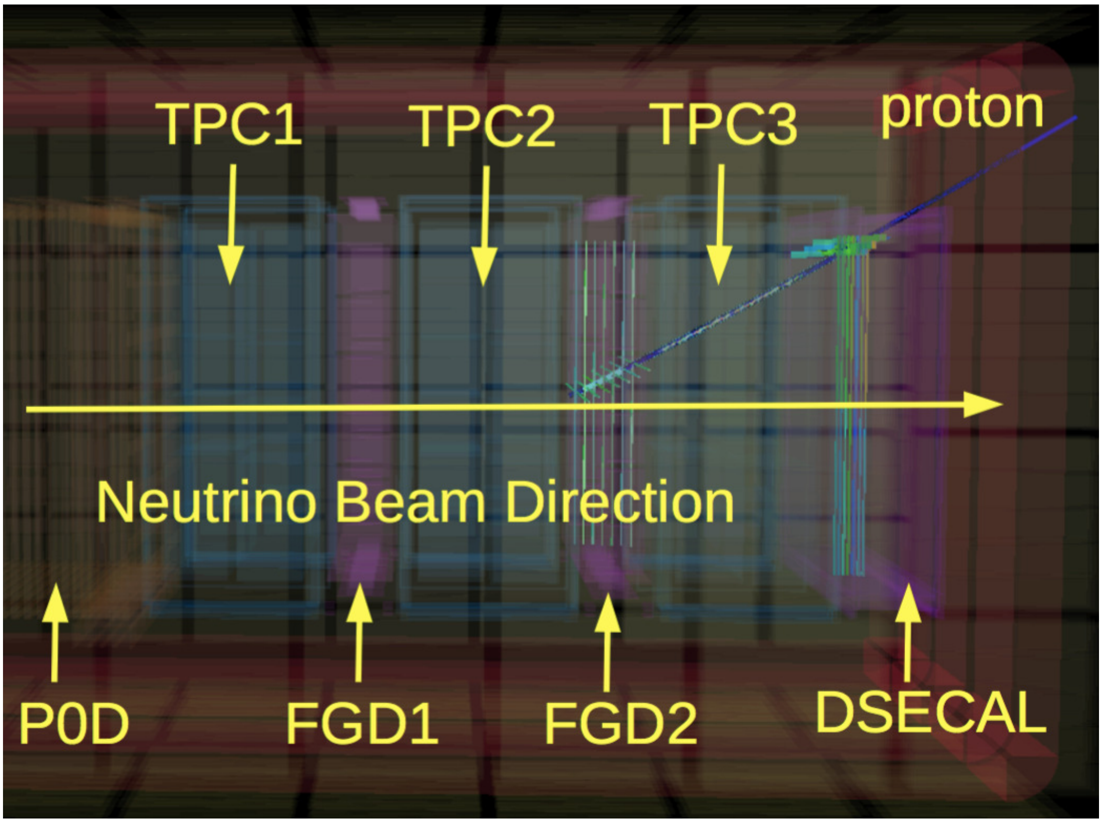

Figure 3.7: A cutaway side view of a proton track inside the ND280.

3.3.1 Time bunches

The neutrino beam in the J-Parc facility comes in 8 distinct time bunches (fig 3.8), thus all the analyses must take this in to account. In order not to mix daughter particles generated from neutrinos, coming from the previous time bunch, we have to put time limits and repeat the same analysis 8 times, each for every time bunch. Between the MC and the data, there is an offset in time, which is known and does not affect the analysis, if we stay within the same time bunch. We just need to use different times for the MC and data, though the duration of each time bunch, and the time separation between two consecutive, are the same in MC and data.

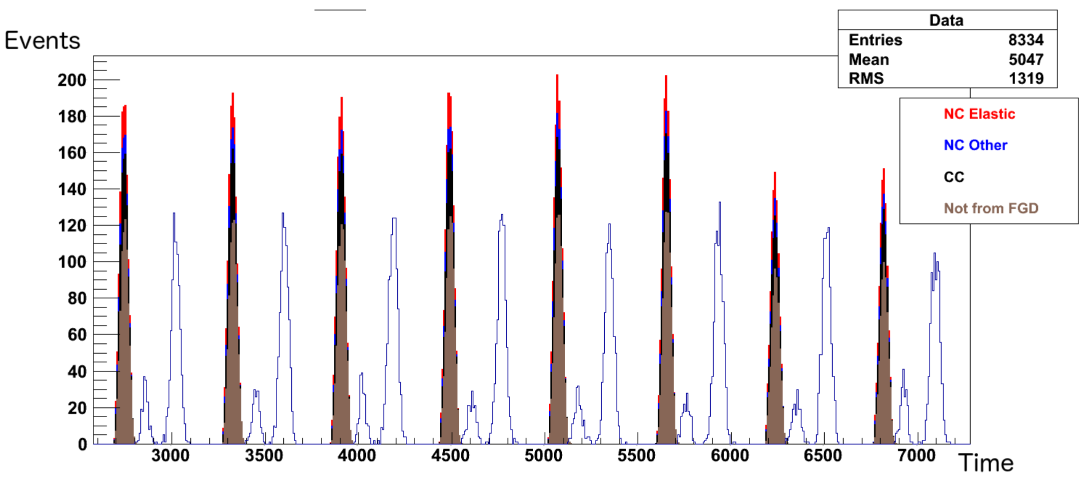

Figure 3.8: The 8 time bunches of the netrino beam, MC vs Data.

3.3.2 Fiducial Volume Cuts

The reconstruction of an event requires good measurements therefore we reduce the fiducial volume of the detector and we only take events with the vertex within the limits we set. This has to be done for the x,y and z direction separately. Events with the vertex outside the limits are rejected. Those constraints are standard in the collaboration and everyone is using the same values for the fiducial volume. For the x-axis we choose for this analysis ($|X| < 970$) (fig 3.9), and for the y-axis ($|Y| < 970$) (fig 3.10). When we apply this cut we also remove a good portion of charged current and other type events, without losing neutral current events. For the z-axis, we need only to include the two FGDs, since we look at events with vertex inside one of the two FGDs. Thus the z-axis cut we choose to be ($160 < Z < 425$ and $1425 < Z < 1800$) (fig 3.11).

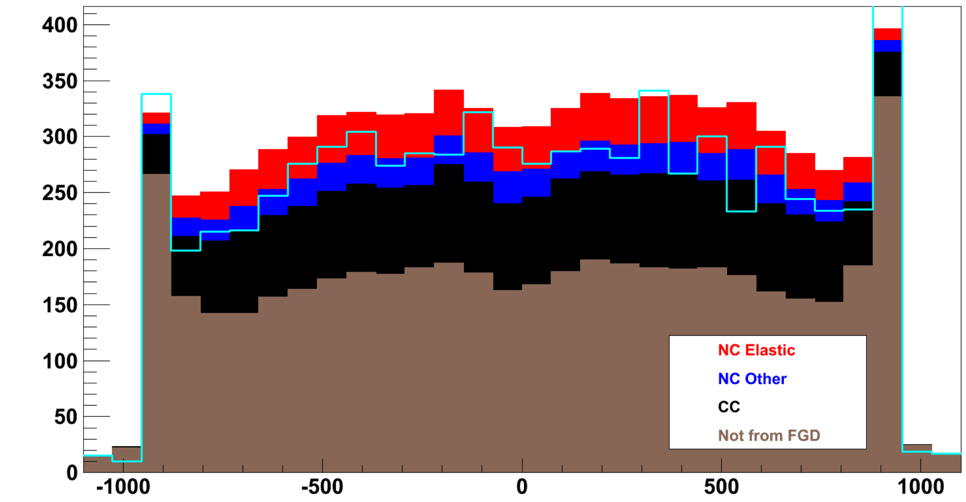

Figure 3.9: The reconstructed position on the x-axis for the main interaction types.

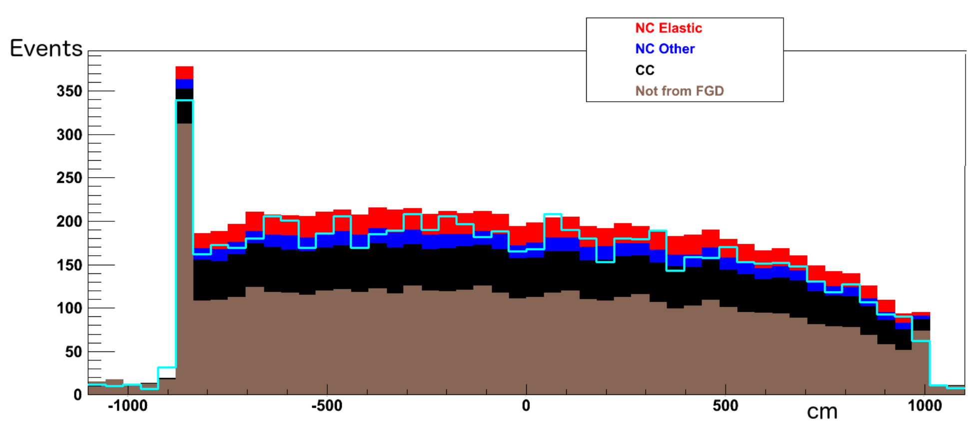

Figure 3.10: The reconstructed position on the y-axis for the main interaction types.

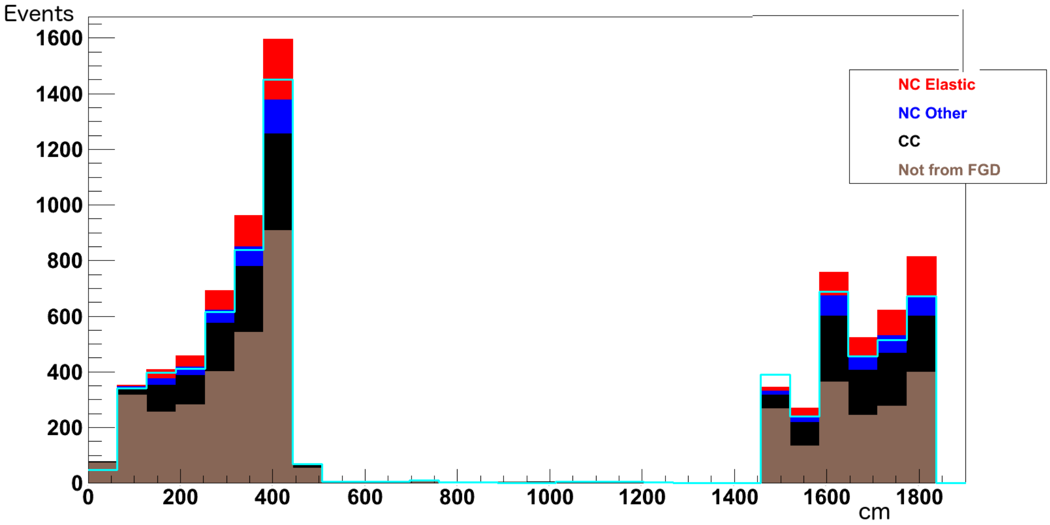

Figure 3.11: The reconstructed position on the z-axis for the main interaction types.

3.3.3 Initial Cuts

First we use general cuts, without using yet the TPC or other components of the ND280. In this part we choose events with a single track, therefore we reject events with more than 1 tracks (fig 3.12,3.18). Then we want activity in the TPC, thus any events that don't include at least one TPC are rejected as well (fig 3.13). The third cut has to do with the number of vertices, since we want only one vertex (fig 3.19), following another cut to include only particles with positive charge (fig 3.14,3.21). Also we do not want events that start in P0D detector, so we reject events that have triggered the P0D (fig 3.15). The P0D is on the front of the detector so if an event has triggered it, we can conclude that we see at a daughter particle of an interaction inside the P0D. Lastly we reject backward tracks and unidentified events (fig 3.16,3.17,3.20,3.22).

In order to quantify the quality of each cut, and relate it with figure of merit, so we can compare it with before and after the cut, we will use the statistical function $efficiency \times purity$. It is an objective method for quality check of each cut, verify the cut has a positive contribution to the selection. The purity is defined as ,

$$purity = \frac{Number\ of\ events\ passing\ the\ cuts\ (protons)}{Total\ number\ of\ events\ (All\ particles)} \tag{3.11}$$

and efficiency is,

$$Efficiency = \frac{Number\ of\ true\ events\ that\ pass\ the\ selection\ criteria\ (selected\ NCQE\ protons)}{Total\ number\ of\ true\ events\ (All\ NCQE\ protons)} \tag{3.12}$$

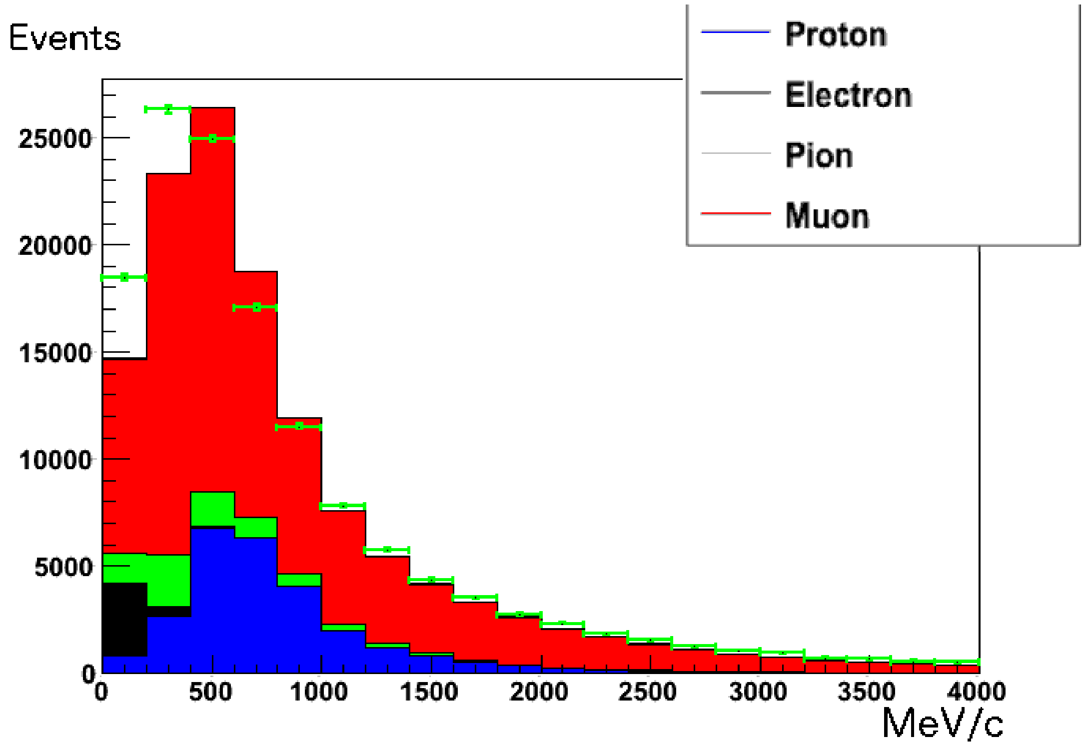

Figure 3.12: The momentum distribution for the p, μ, π, e for single tracks and vertex in the TPC. The points with error bars (green), show the data.

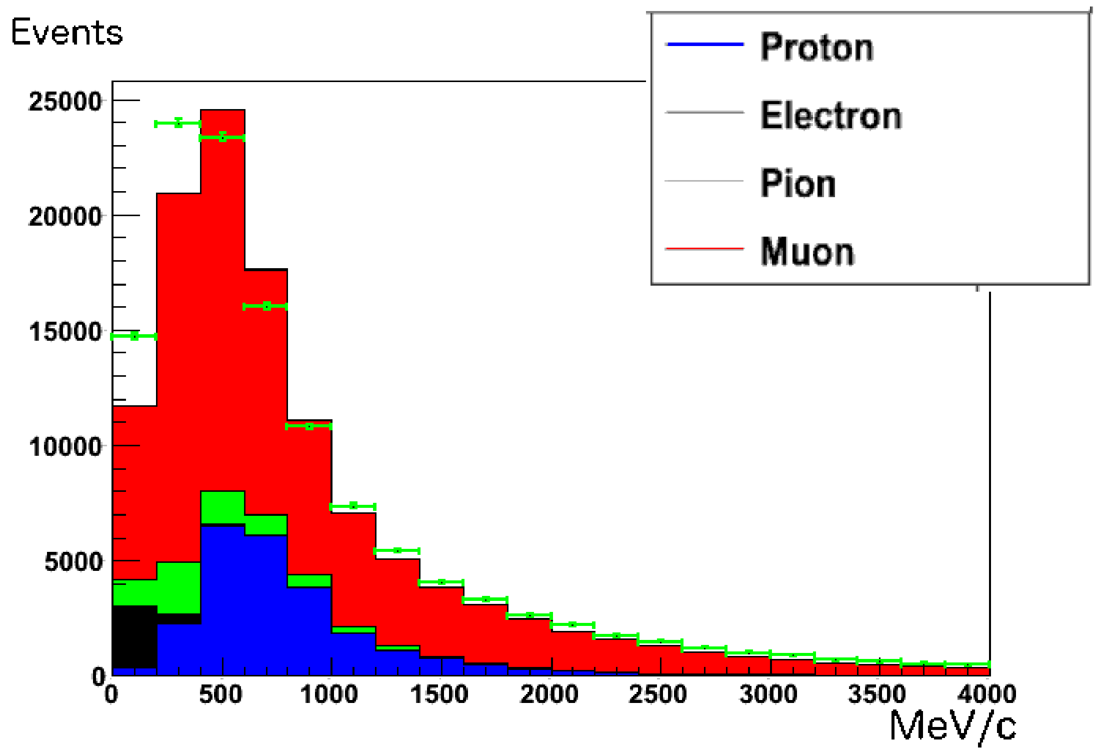

Figure 3.13: The momentum distribution for the p, μ, π, e for single tracks and vertex in the TPC. Also we want the event to hit more than 18 layers in the TPC for good event reconstruction. the points with error bars (green), show the data.

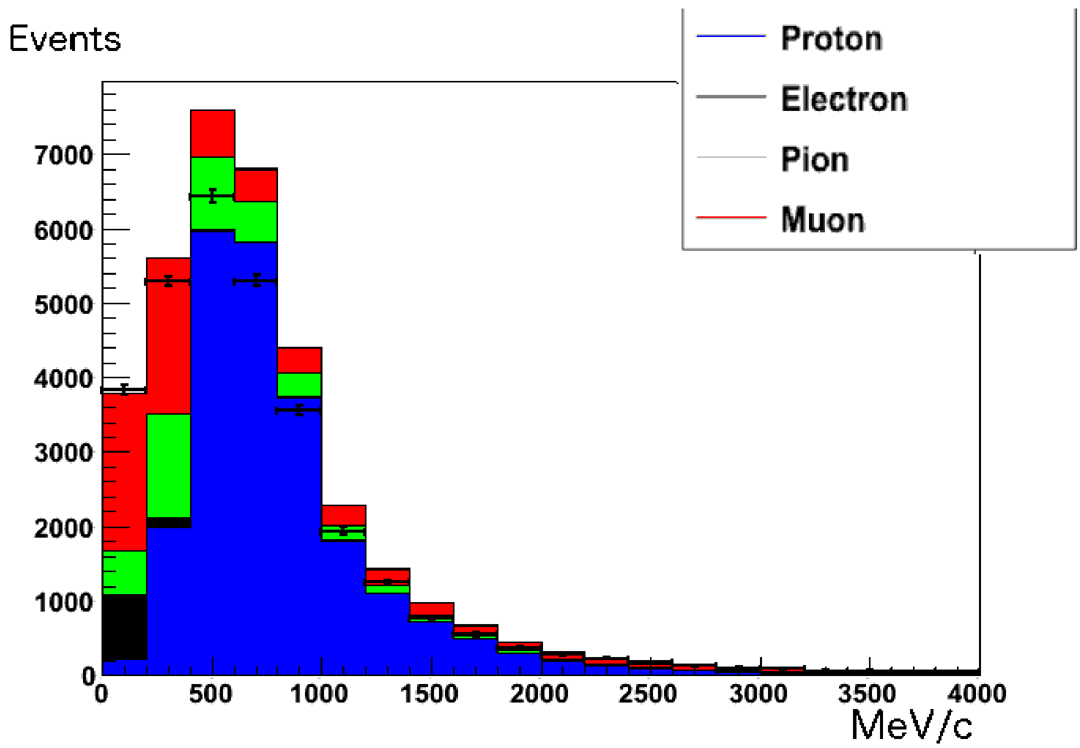

Figure 3.14: The momentum distribution for the p, μ, π, e for single tracks and vertex in the TPC. Also we want the event to hit more than 18 layers in the TPC for good event reconstruction.We take only the tracks for the positive charged particles. the points with error bars (black), show the data.

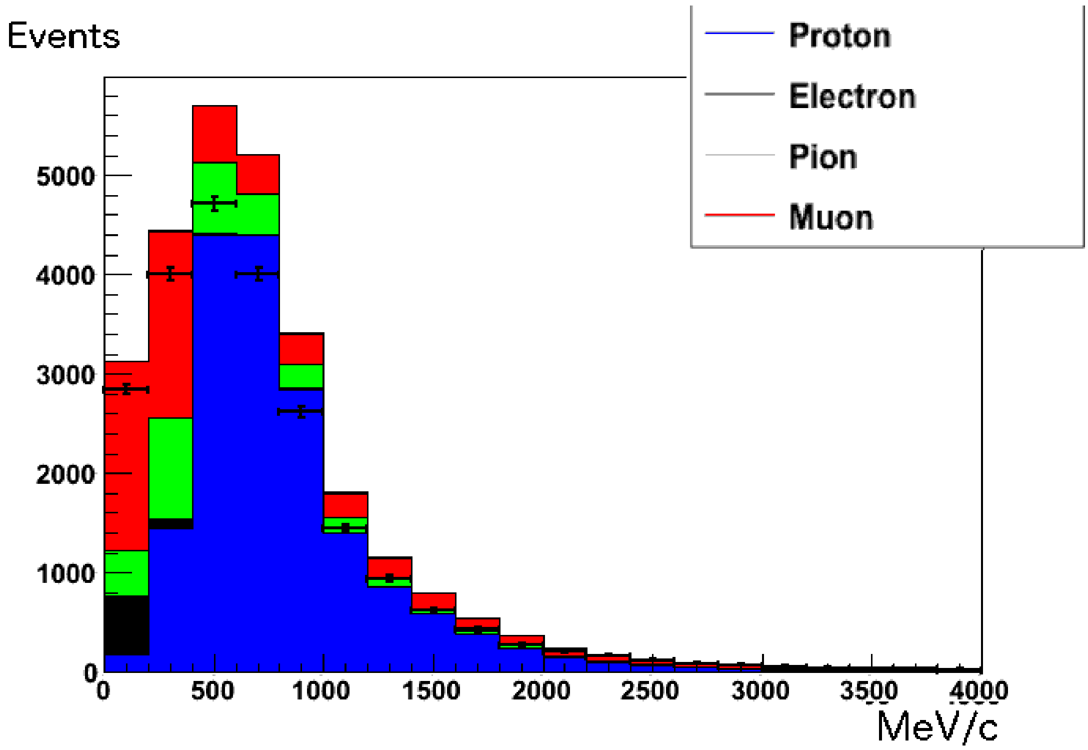

Figure 3.15: The momentum distribution for the p, μ, π, e for single tracks and vertex in the TPC. Also we want the event to hit more than 18 layers in the TPC for good event reconstruction.We take only the tracks for the positive charged particles. In addition we reject the events with P0D activity. the points with error bars (black), show the data.

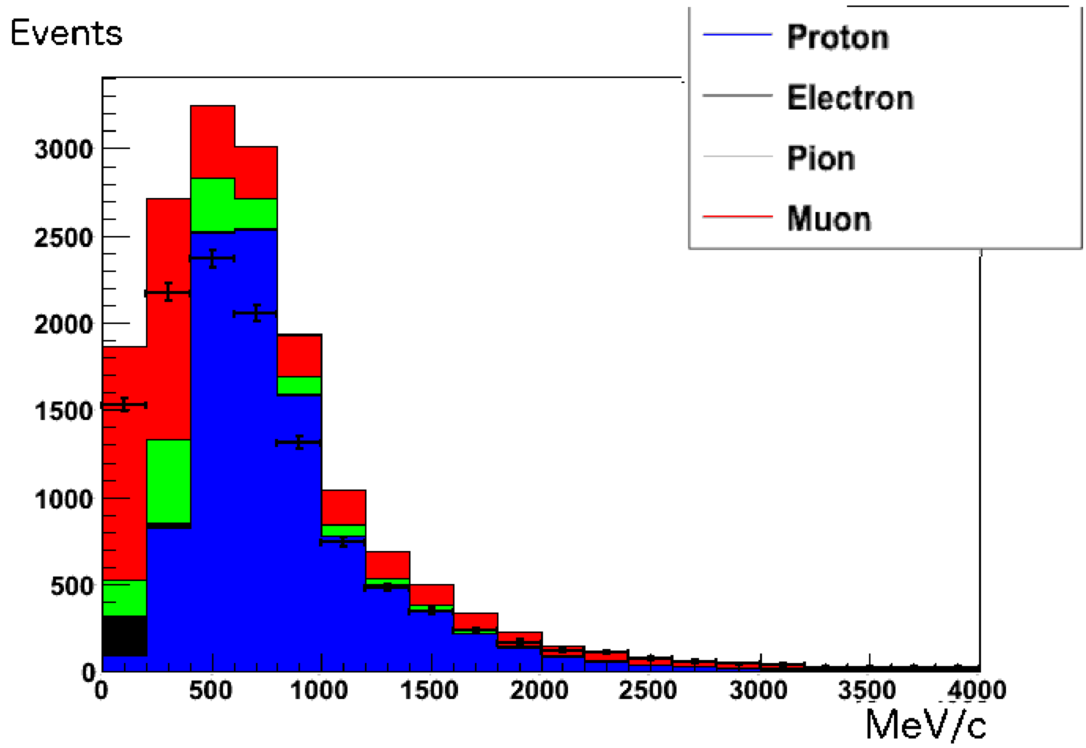

Figure 3.16: The momentum distribution for the p, μ, π, e for single tracks and vertex in the TPC. Also we want the event to hit more than 18 layers in the TPC for good event reconstruction.We take only the tracks for the positive charged particles. In addition we reject the events with P0D activity. Also we reject unclassified events. the points with error bars (black), show the data.

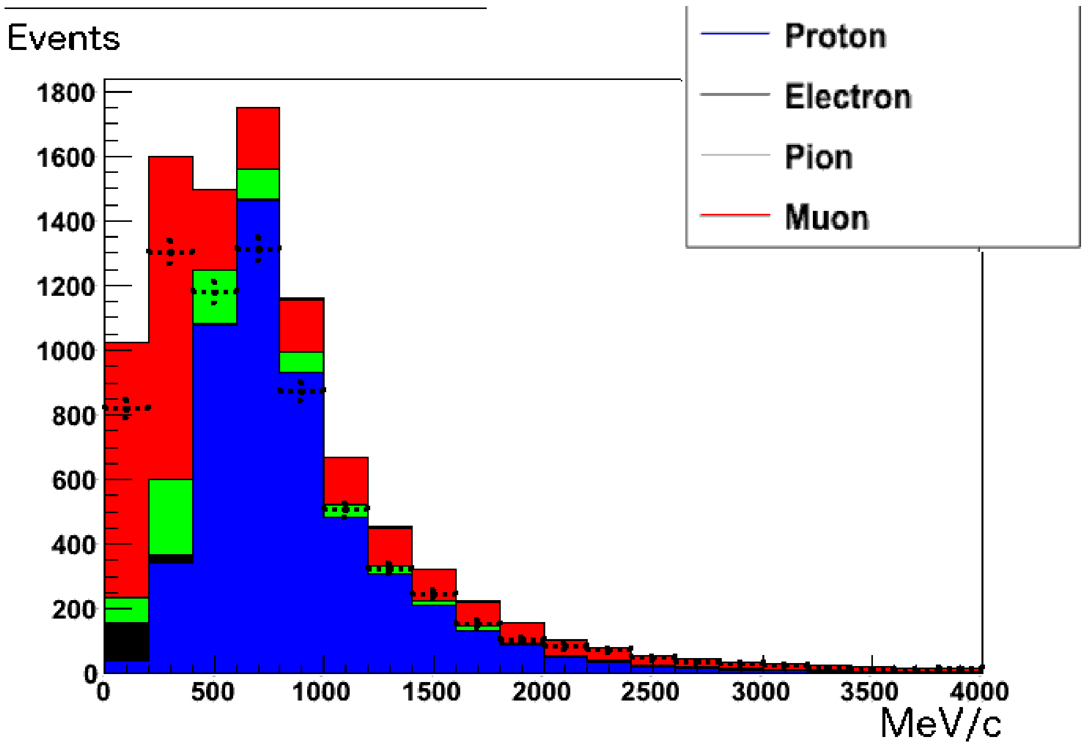

Figure 3.17: The momentum distribution for the p, μ, π, e for single tracks and vertex in the TPC. Also we want the event to hit more than 18 layers in the TPC for good event reconstruction.We take only the tracks for the positive charged particles. In addition we reject the events with P0D activity. Also we reject unclassified events. the points with error bars (black), show the data.

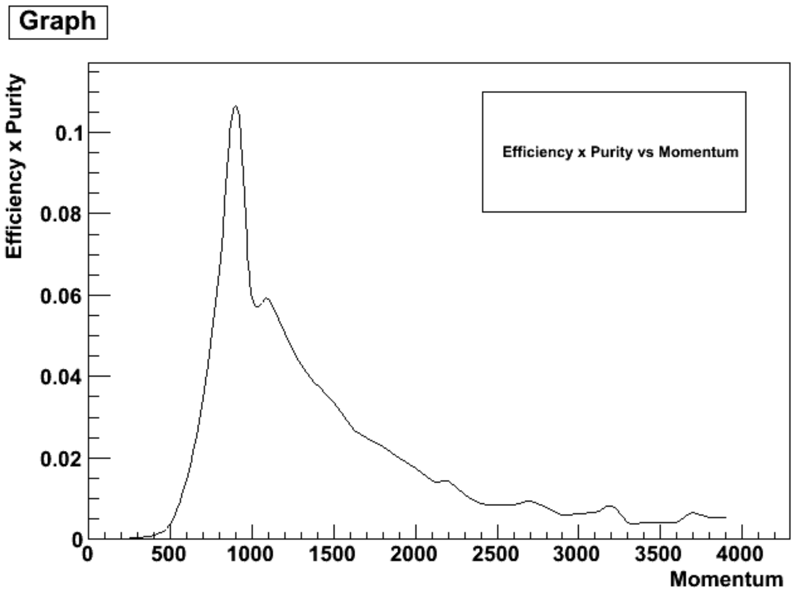

Figure 3.18: Purity×Efficiency for single tracks.

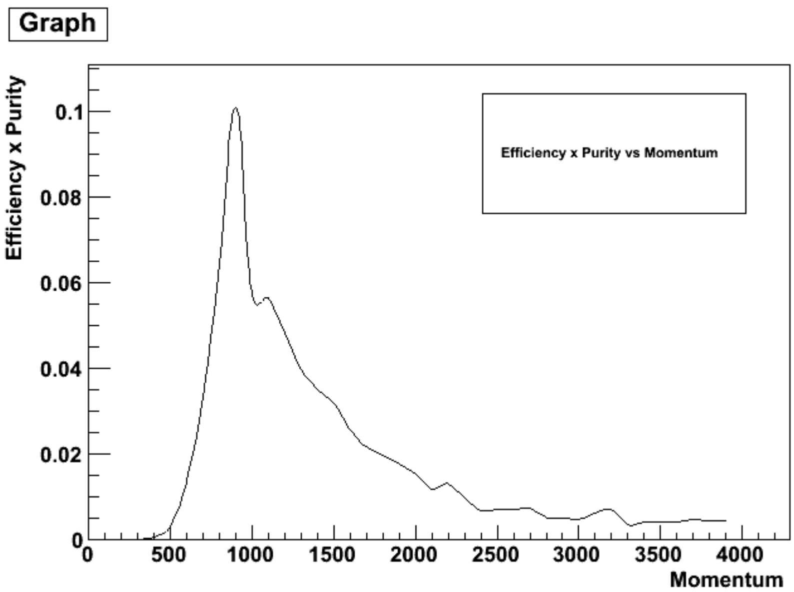

Figure 3.19: Purity×Efficiency for single tracks, with TPC activity and more than 18 hits.

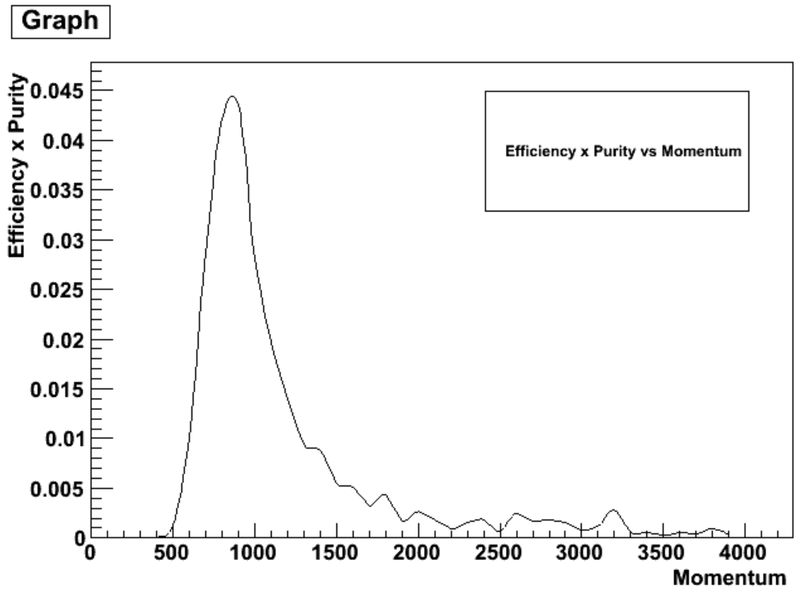

Figure 3.20: Purity×Efficiency for single tracks, with TPC activity, more than 18 hits and one vertex.

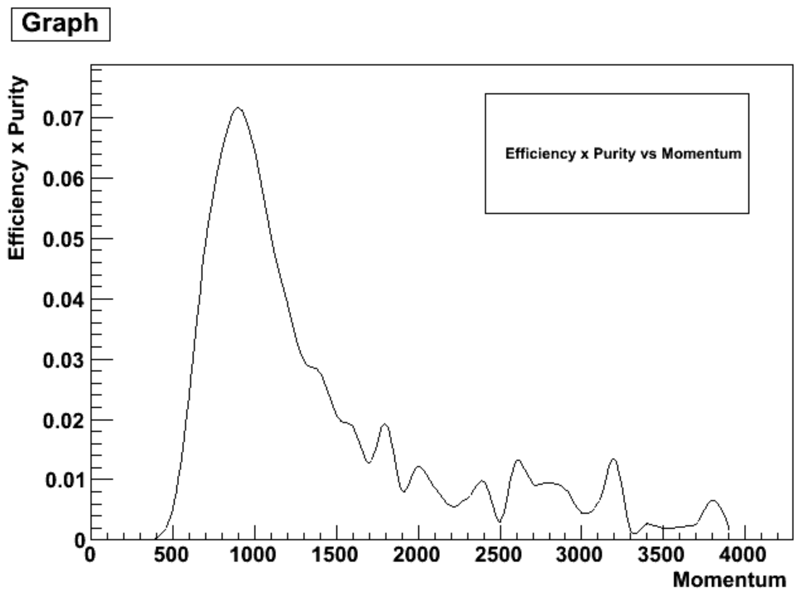

Figure 3.21: Purity×Efficiency for positive, single tracks, with TPC activity, more than 18 hits and one vertex.

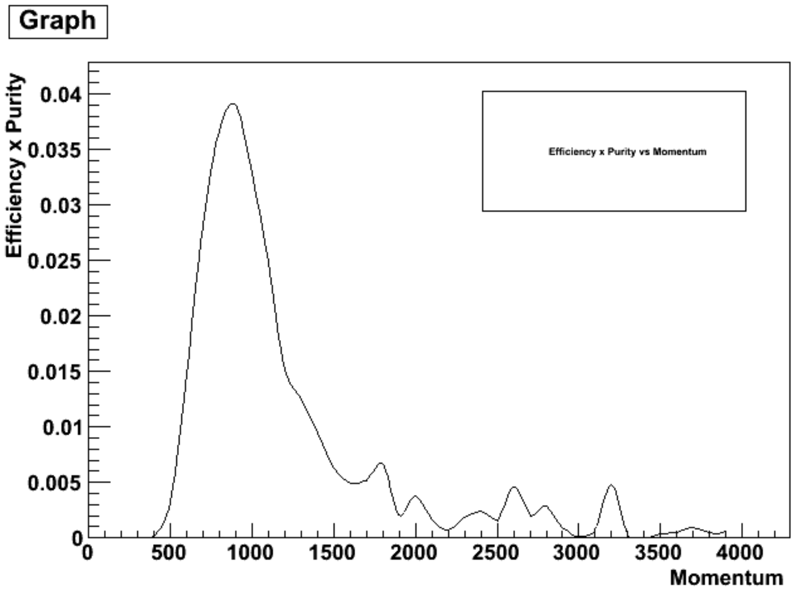

Figure 3.22: Purity×Efficiency for positive, single tracks, with TPC activity, more than 18 hits, single vertex, and without P0D activity.

3.4 Selection optimisation

At this point we have finished with the preliminary selection and we will try to reduce the background (non NCEL p interactions) using information from the TPC and the ECal. The previous cuts helped to improve our signal/background ratio, and we did not lose a lot of events, thus did not affect much our statistics.

3.4.1 Proton Pull optimisation

The next step is to use the available information we have from the TPC and the ECal. Also we did not treat differently the two momentum regions. The preliminary cuts applied equally to all protons regardless their momentum. At this point we will define the pull, using the measured energy a particle deposits in the TPC.

$$pull = \frac{expected\ dE/dx - measured\ dE/dx}{\sigma} \tag{3.13}$$

Where σ is the standard error and the pull is a hypothesis test. Assuming the particle is a proton, how far is the measured dE/dx, from the expected dE/dx. It is a good tool to discriminate protons when there is enough separation between the curves in the "Bethe-Bloch" formula (fig 3.23, 3.24).

To this problem there were two approaches, we can either apply a cut on the proton pull, or make a cut to the pull of the particles which contribute heavily to the background (e, π, μ). In order to take an objective decision we used the $efficiency \times purity$ function and we also used it to choose the optimum value for the pull cut. So we tested the two hypotheses (fig 3.25), and the optimum proton pull cut is $|proton\ pull| < 2.5$.

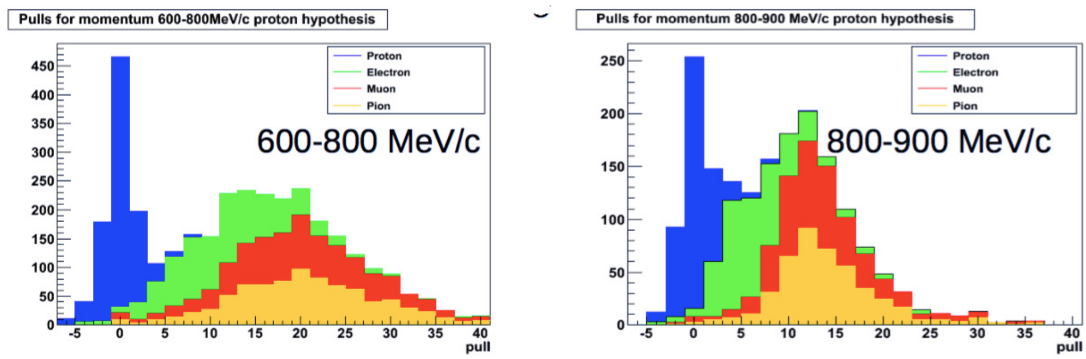

Figure 3.23: The pull, for a true proton hypothesis, for the momentum region $0-800\ MeV/c$ and $0-900\ MeV/c$, for the $p(blue\ colour), e, \mu, \pi$.

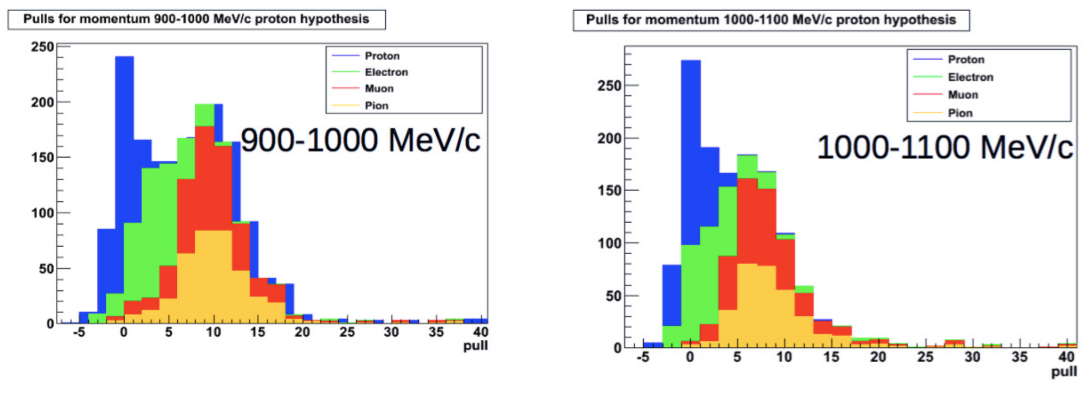

Figure 3.24: The pull, for a true proton hypothesis, for the momentum region $900-1000\ MeV/c$ and above1000 MeV/c, for the $p(blue\ colour), e, \mu, \pi$.

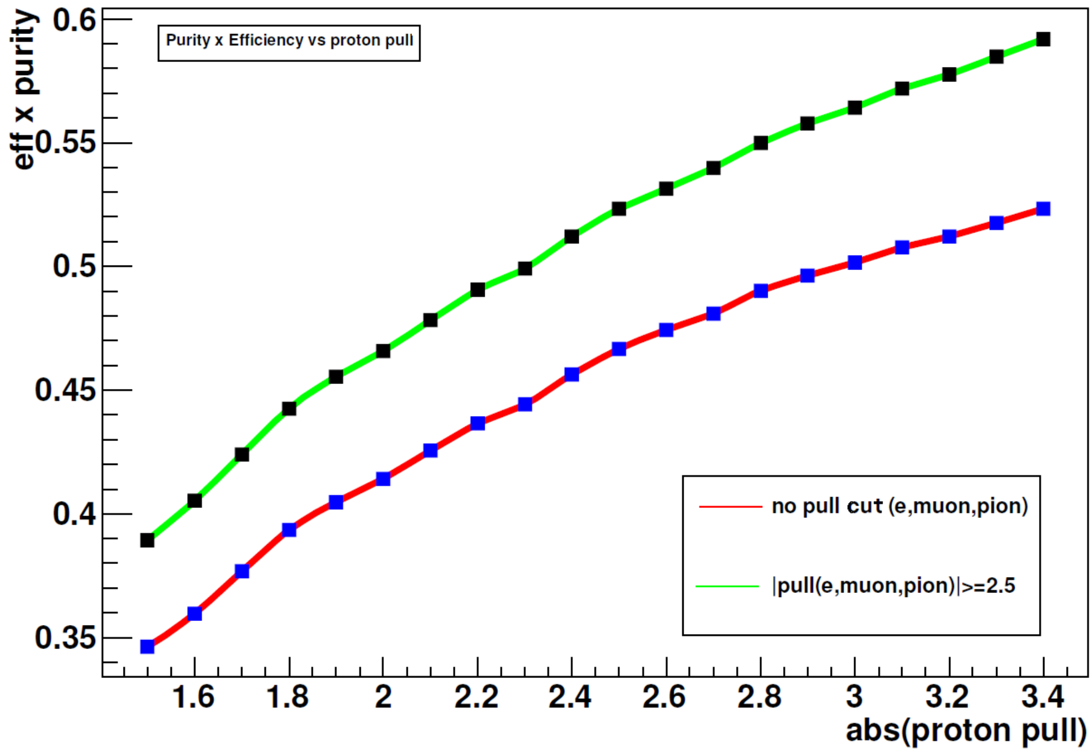

Figure 3.25: The $efficiency \times purity$ against the pull cut, for two cases. In the first (red) we apply cuts on the proton pull only, and the second (green) we make cuts on the pull of the (e, π, μ) and proton.

The last variable we will use for the selection is the track length inside the calorimeter. Most of the protons with momentum above 900 MeV/c, enter in the ECal (fig 3.26) and by observation we see that the majority of the particles with more than 30 hits, are not protons. Thus we use this value to increase the proton purity without losing much in the efficiency. For the BrECal (fig 3.27), the optimum value for the cut is not obvious, so after looking at the purity vs track length in the BrECal, we concluded that the optimum upper limit for this variable is 20 (fig 3.28).

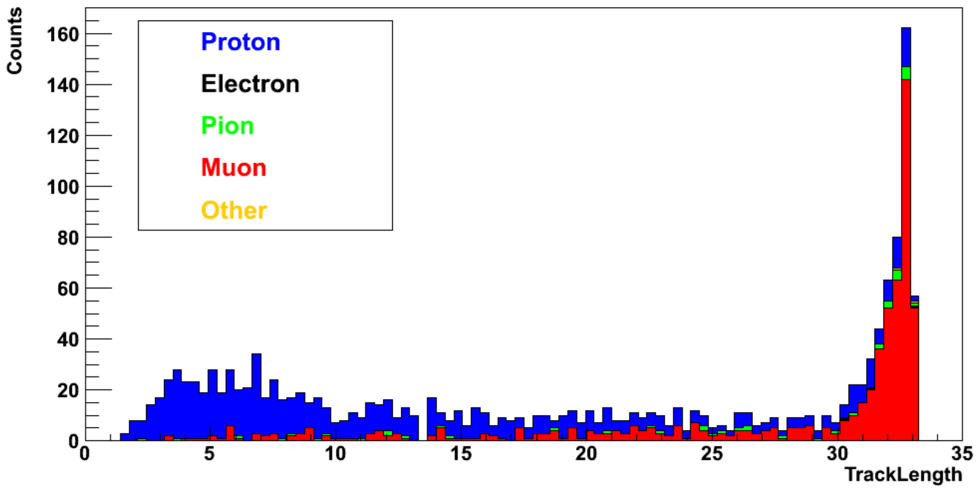

Figure 3.26: The ECal track length for p, e, μ, π.

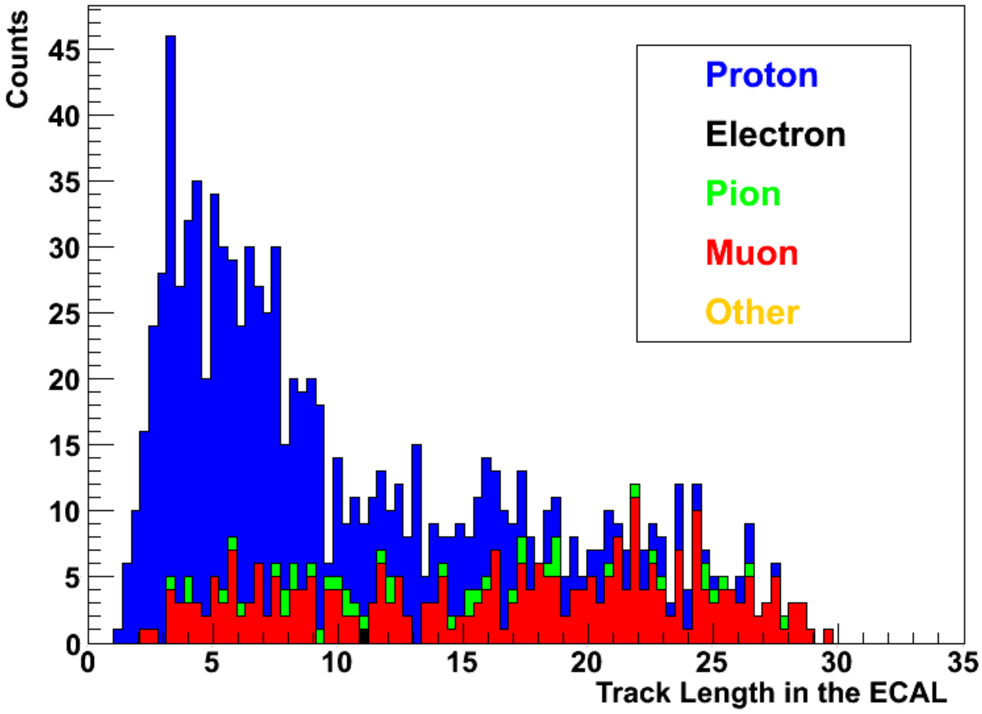

Figure 3.27: The BrECal track length for p, e, μ, π.

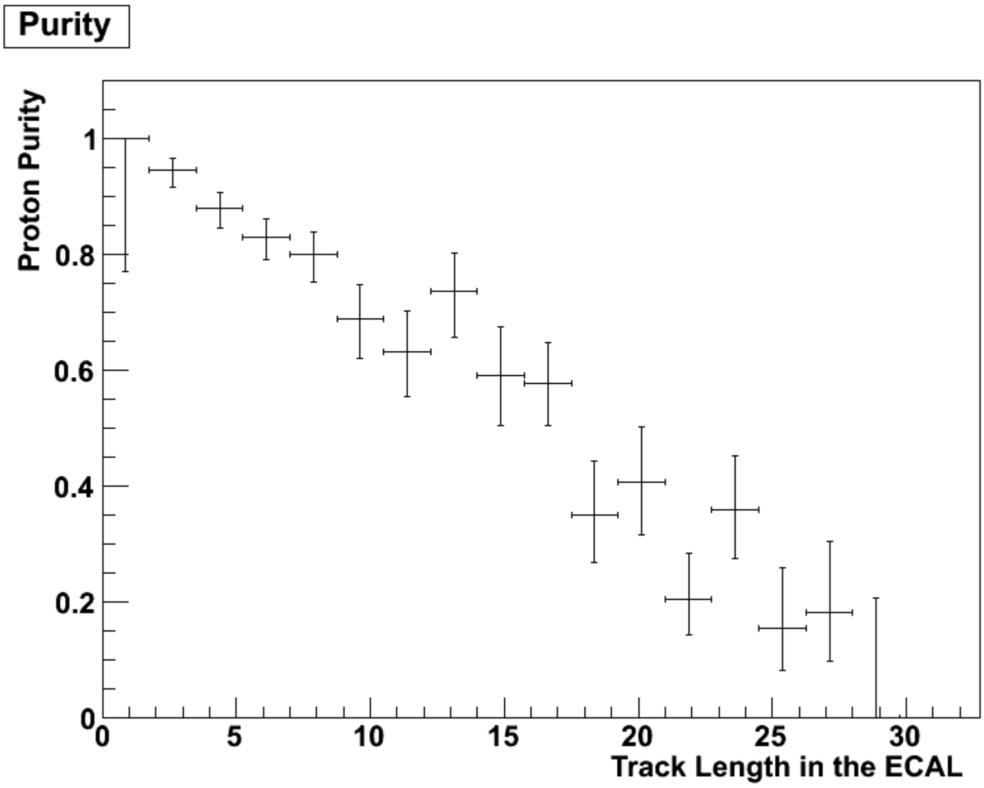

Figure 3.28: The purity vs BrECal track length..

3.5 Final Event Selection and Results

The event selection is concluded with good results. After the preliminary cuts we applied to all data, we split the data in to two sets with different momentum. The lower momentum data use mostly the information from the TPC to discriminate the protons, while the second set with higher momentum events, is sent to the Neural Network, in order to improve the selection and reject more background. Then the results from the Neural network and the TPC are joined again to create one final sample and the results can be seen in the Neural network chapter.

Chapter 4

Neural Network for the ECAL

4.1 The Two Populations Problem

The neural network was developed to identify single protons interacting in the FGD's, with momentum higher than 900 MeV/c. In this region the TPC alone can not distinguish the protons among the other particles. The neural network is optimised to select events with protons and reject the other events, which is the background. With this method, we see the signal and the background as two data sets, and only a multivariate analysis can find the optimum way to separate the two populations. The problem of the two populations is difficult to tackle, and although there are many mathematical tools, none of them is perfect.

To understand this better we should see an example. In the figure 4.1 we see a visualisation of the problem, which has been described above. We clearly see two data set populations, with one of them being our signal (blue colour) and the other the background (colour). The variable X is an input to the neural network to visualise see how it works in theory. The main issue here is that the two populations overlap, later we will see this is repeated in every single variable we use. The area the two sets overlap pose a problem, since events that fall in that region give similar output in our variable.

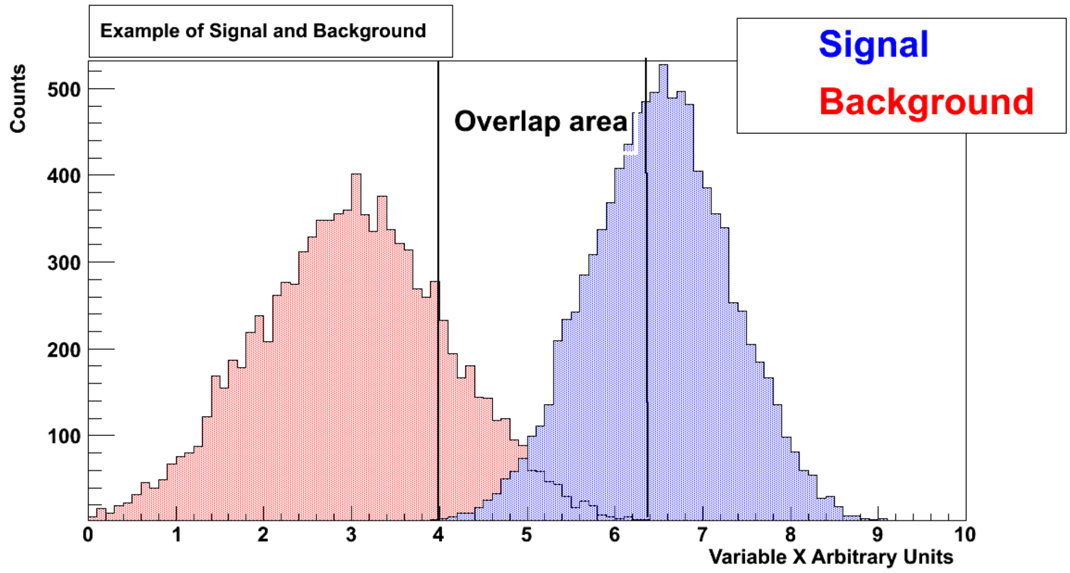

Figure 4.1: When two populations overlap, we need a multivariate analysis to separate them in the overlap region.

In this case, since the problem is simplified for illustrative purposes, we can choose a value on variable X, to reject the background. Though this method will work here, we will see later that it will not be always so simple, and then choosing a simple cut can be an impossible task. In many cases the overlap area is much larger, and most of the signal is merged with the background. In addition if we reject a big portion of our signal, we have an efficiency loss. To extract safe results one should have data from all the regions of the variable.

In general, we use many parameters for each event, and to make things even worse, those variables almost always will not be independent of each other. This means, choosing a value, for one variable, to cut, affects the other variables. So we could go on an infinite cycle where cutting variables change the outcome a lot and therefore, we will need to make new cuts. Also making a cut on one variable has actually unpredictable results on our analysis. Our main goal is to keep the signal, thus to increase the "purity" of our data, to have data where the background is rejected.

With all the above arguments, I believe the reader is now convinced that we need to apply other methods to clear our data from the background (noise). In this analysis, the neural network was chosen as the tool of choice. This is, of course, not the only method, at the end of the chapter we will see the reasons for choosing a neural network, among other methods. The neural network is a decision algorithm, reading the inputs, and after performing calculations, is telling you how likely is the event to be part of the signal or the background. The advantages of this method is that can characterise events that happens to be in the region where signal and background overlapping (fig 4.2). This is particularly useful in a case where the number of events is expected to be low, and is important to collect as much of the signal as possible.

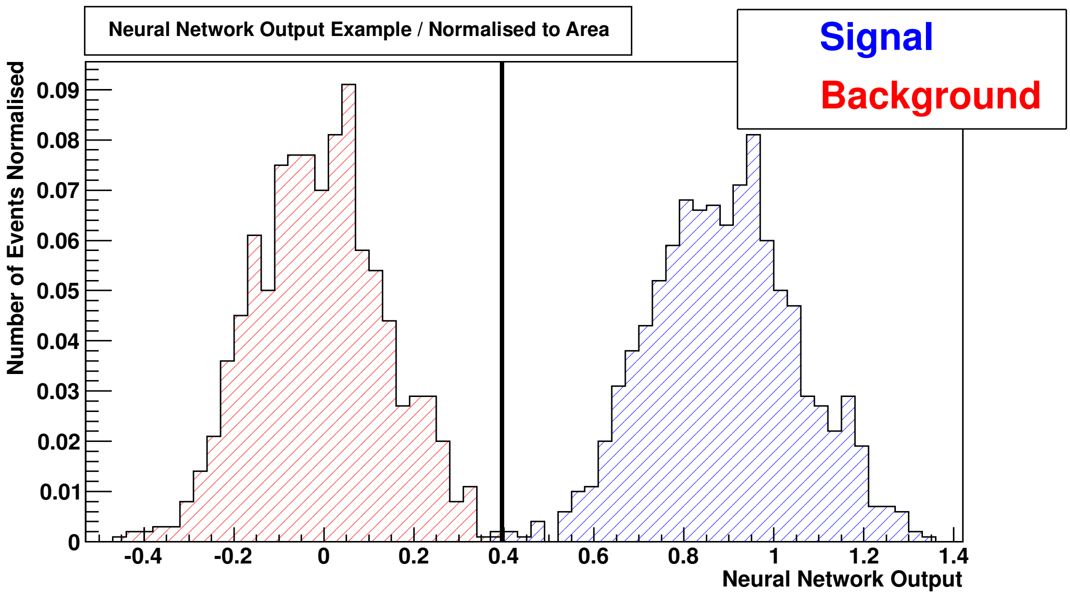

Figure 4.2: Example of NNA output.

The neural network is a mathematical method which can optimise multidimensional analysis, and this is its main strength. Each variable is a dimension of our system, the neural network can give an optimum cut, therefore can improve the discrimination between signal and background. Ideally the output should have a wide space between the two populations, but in most cases collects the events that are similar to the signal on one end of the axis, while collects the rest of the events on the other. As a result, the events that overlap should be a lot less, and the distinction between signal and background becomes clear. Finally we can find, the optimum value of the neural network output to cut. Therefore we can avoid making multiple cuts on individual variables for each event, and instead we can make one single final cut on the output of the neural network (fig 4.2).

Another example where the traditional methods can not give a positive result, is when the data do not follow any pattern, and is impossible to find a linear cut between signal and background(fig 4.3). This is a very common problem and can be solved only with pattern recognition algorithms, such as neural networks, which they can find a non linear multidimensional cut. Here we conclude the discussion for the motivation and the usefulness of this method.

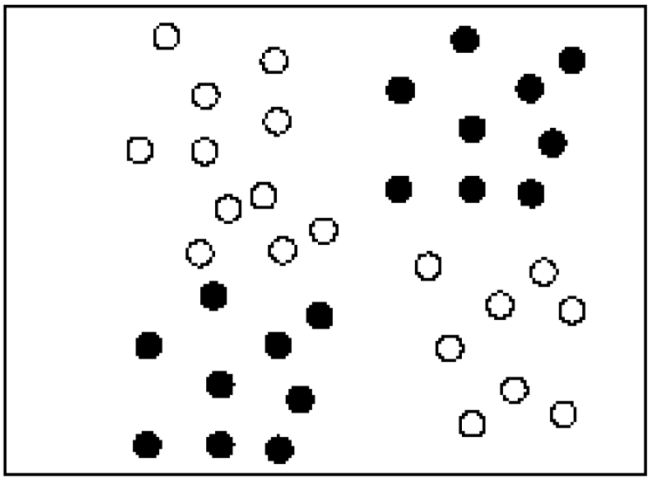

Figure 4.3: Example of data points we can't separate with a linear cut, while a Neural Network can find a non linear cut.

4.2 Neural Network Introduction

The Artificial Neural Network (ANN) is an algorithm that is loosely modelled after the biological nervous system, such as the brain. One of the inventors of neuro-computers, Dr Robert Hecht-Nielsen [50] defines a neural network as: "...a computing system made up of a number of simple, highly interconnected processing elements, which process information by their dynamic state response to external inputs”. It is composed of interconnected elements, called neurons, working as a unit to solve specific problems.

In biological systems like the brain, there are billion of neurons while in an ANN we have processing units. The processing power of the biological systems increase in magnitude of their overall interaction. So the ANN is designed to mimic this behaviour, although researchers do not try to accurately replicate the biological systems.

The brain learn by example and is using the memory to recover previous results and decide how to proceed in a similar situation. Similarly the ANN goes through a learning process for a specific application that is designed for. Analyses known data and stores the results in a file, thus replicating the memory. So to analyse a new set of data, recalls the old results to extract the new results. ANN are very good for specific applications such as pattern recognition, data discrimination and in general problems were adaptability is required.

There are many ANN algorithms, and all based on a theorem that states, “finite linear combinations of compositions of a fixed, univariate function and a set of affine functional can uniformly approximate any continuous function of n real variables with support in the unit hypercube” [51]. Although the mathematics involved with neural networking is not a trivial matter, a user can rather easily gain at least an operational understanding of their structure and function. The figure below (fig 4.4) shows the structure of a typical neural network.

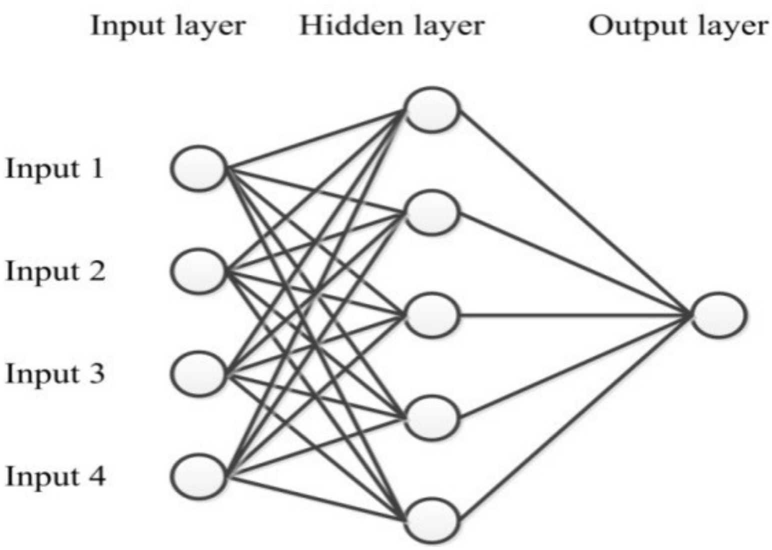

Figure 4.4: A visualisation of a Neural Network structure.

The structure of the neural network is consisted of three layers.

1. The first layer is the inputs variables of the system we study. For example, if we want to discriminate a particle like in this analysis we want to discriminate protons, we feed the neural network with the variables of the particle. Such variables could be for example the momentum of the particle, the mass, the reconstructed energy and variables that can help us identify the particle we are looking for. We take the values of those variables while we read all the events of our data set, and it is therefore an event by event analysis.

2. The second layer is hidden, and this the point where the system is doing the calculations. A simple way to describe the calculations at this stage would be, that the neural network is calculating the weight for every connection between the nodes of the different layers. So each synapses (link between two nodes) gets a value, positive or negative. We do not have access at this phase, though we define the structure of that layer.

   We choose for example the number of the neurons/nodes, and we can have multiple layers with each one having different number of nodes. So we could have two layers, the first with A nodes and the second with B, where A and B are natural numbers. There is no single perfect structure, therefore with trial and error, by changing the structure of the hidden layer (changing number of nodes and hidden layers), we need to calculate the efficiency of our network and thus decide the best configuration. It is very important to adjust the neural network to our analysis so to get sensible results. In general though we should try to keep the structure as simple as possible, in order to minimise the bias, and make the system faster. A complicated neural network will try to find connections between variables, even if those connections do not exist.

3. In the last layer we get the output, the result of the calculations. The algorithm is adding the weights to give a final value. Usually is a number between [0,1], but is not always the case as we can define the minimum and maximum value. What we should expect to see though, is the values for the data points of our signal to be around the maximum value and everything else (noise/background) to be around the minimum value (fig 4.2).

Once we set up the neural network, and we have decided the optimum configuration, we need to train it. For that we should use a sample, similar to the data we study so to make it as efficient as possible. During this phase, the system is "learning" by creating or deleting connections (synapses), and changing the weights. It stores the patterns that can identify for each event. Is it important not to over train it, as it won't be able to analyse events dissimilar to those of the sample. For that we have also a verification sample, and ideally both samples should be randomly chosen from the same sample (Usually with division relations, 70% training, 30% verification). At this stage we are ready to use our Neural Network .

4.3 Neural Network for Proton Discrimination Using the ECal

As we have discussed, there are many algorithms that qualify as neural networks. For this analysis the multilayer perceptron has been used. All ROOT versions, have it installed and available for use. Since the neural network can be useful to others in the T2K collaboration, we can make it easy to use, by using packages widely available.

Although there is no established definition of the perceptron, the term is mostly used to describe a "feed-forward network with short-cut connections”[52]. Feed-forward means that each neuron in one hidden layer has connections with direction to the next hidden layer only, and not the other way around. A multilayer perceptron, has multiple hidden layers and this is the most popular algorithm for the neural networks. The aim of this chapter is to give a brief explanation of the neural network.

In this analysis, the neural network was designed to select protons using the Electromagnetic Calorimeter (ECal). There are some for the ECal [8], which can distinguish between track-like, shower-like events, and can identify the MIP-like events. We decided to use the six most prominent variables that are included in Production 5. The reason for creating a neural network, was due to the inability to find independent optimum cuts for those variables. The main problem is that those variables are correlated (fig 4.12,4.13,4.14,4.15), therefore a cut on a variable, changes the distribution of the others, and the combinations of the cuts are infinite. We are dealing with six variables and it is a six dimensional system, with non obvious connections among the variables. The second problem is that the distributions of the particles for those variables look similar(fig 4.5,4.6,4.7,4.8,4.9,4.10,4.11), therefore it is an impossible task to calculate where to cut on a variable so that we collect only protons. In such situations the neural networks excel and many times is the only way to proceed. There is one more variable we are using and is coming from the TPC, which is the Energy/Momentum (E/p). This is widely used to discriminate particles so we decided to include it as well.

We are using the following ECal variables [8]:

1. ShowerAngle

   The angle is calculated from the Principal Components Analysis (PCA) in three dimensions, on the hits within a cluster. In principle, we expect small angles on the track-like particles, while Electro Magnetic (EM) showers, should give larger angles. The output of variable is given in rads, and the mathematical definition is given below (fig 4.8).

$$\theta = tan^{-1}(\frac{2nd\ principal\ component}{1st\ principal\ component})$$

2. ShowerWidth

   It is the variable describing the spread of the cluster. and is a dimensionless quantity (fig 4.9). Track-like particles give small width and EM showers, should give larger width. It is another variable to separate between MIP's and non MIP's

3. Circularity

   This variable is calculating the correlation between two axis. The variable takes values in the [0,1] interval, and is dimensionless. Linear correlation between two axis gives circularity 1, and if the axis are not correlated the circularity is 0. The events that give track-like clusters should give circularity close to one, and the shower-like clusters close to zero. The mathematical definition is the following (fig 4.5) :

$$Circularity = Circularity_x \times Circularity_y \text{ and,}$$
$$Circularity_i = (2 \times (2nd\ principal\ component)) - 1$$

4. TruncatedMaxRatio

   Is the ratio of charge in the highest charge layer to the lowest charge ratio, after removing the top 20% and the bottom 20% of the hits. In each layer of the

ECal we calculate the charge deposited, and we use those values to calculate the variable. It is optimised to discriminate between muons and electrons and is dimensionless(fig 4.10).

5. QRMS

   This is defined as the variance of the hit charge denominator, and it is dimensionless. Shower-like particles should give higher q_{RMS}, than non shower-like(fig 4.7).

$$q_{RMS} = \frac{1}{q}\sqrt{\sum_{i}^{N}\frac{(q_i-\bar{q})^2}{N}}$$

q_i is the number of hits,$\bar{q}$ is the mean hit charge, N is the number of hits within the cluster.

6. FrontBackRatio

   The length of the line connecting, the lowest and the highest hits, is divided in to four equal parts. In each part the total charge is calculated. The total charge of the back quarter, over the total charge in the front quarter, is the FrontBackRatio (fig 4.6). This variable can discriminate between MIP's and non MIP's.

7. E/p

   This is the only variable not from the ECal PID, though is using the ECal to calculate the total energy deposited by the particle. This variable can discriminate between MIP's and non MIP's. The variable assumes the event is an electromagnetic shower. The electrons give 1, while particles that dont create EM shower give values near zero(fig 4.11).

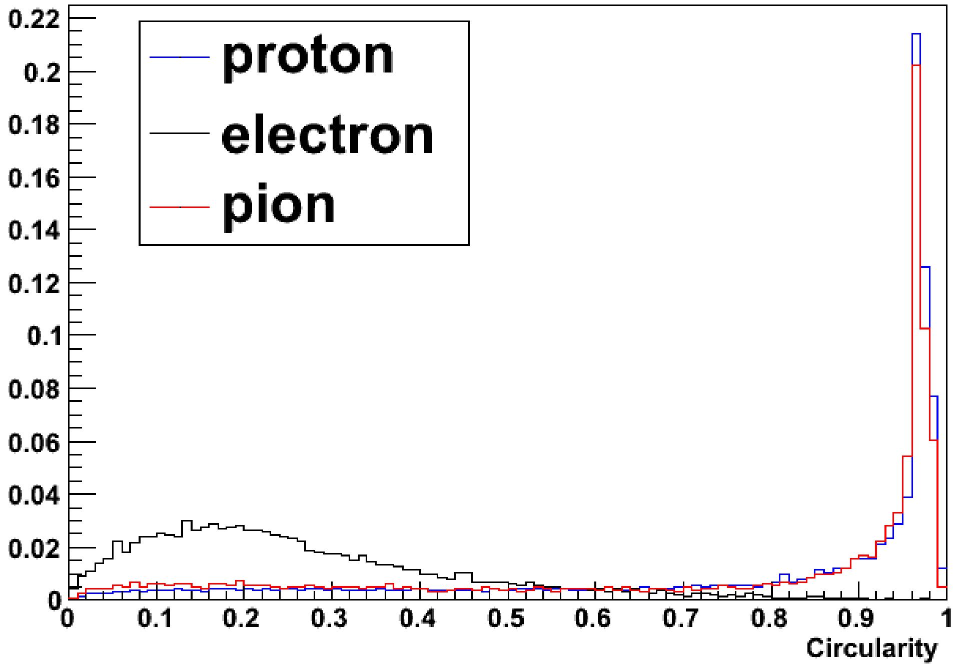

Figure 4.5: The Circularity, for proton, electron and pion.

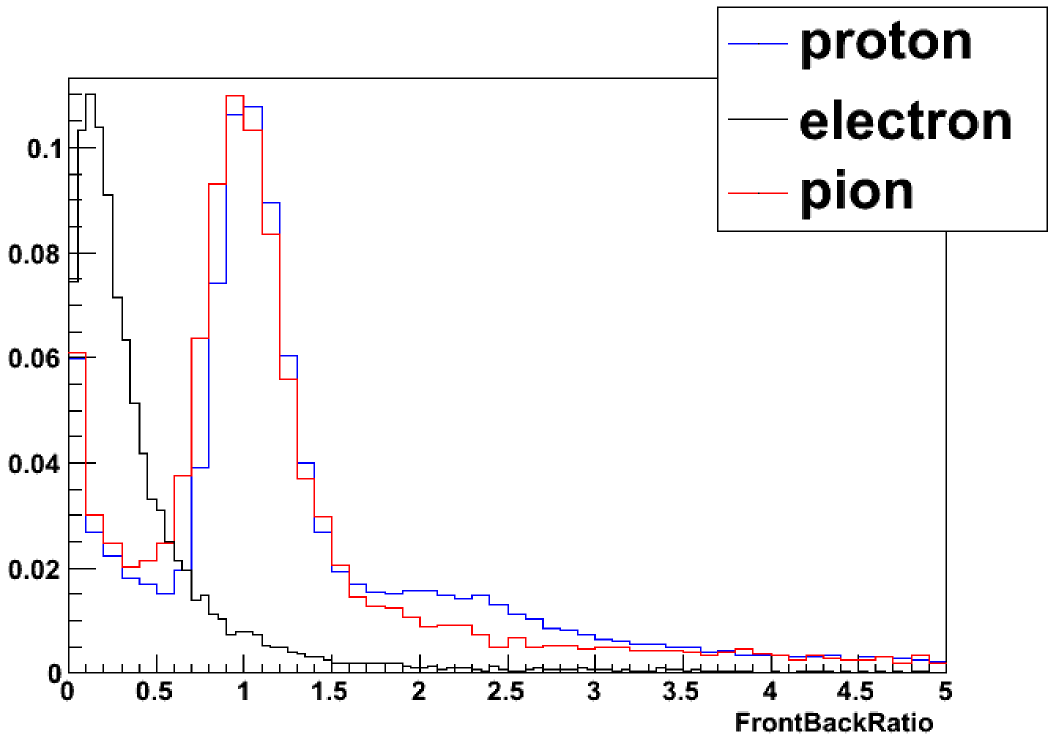

Figure 4.6: The FrontBackRatio, for proton, electron and pion.

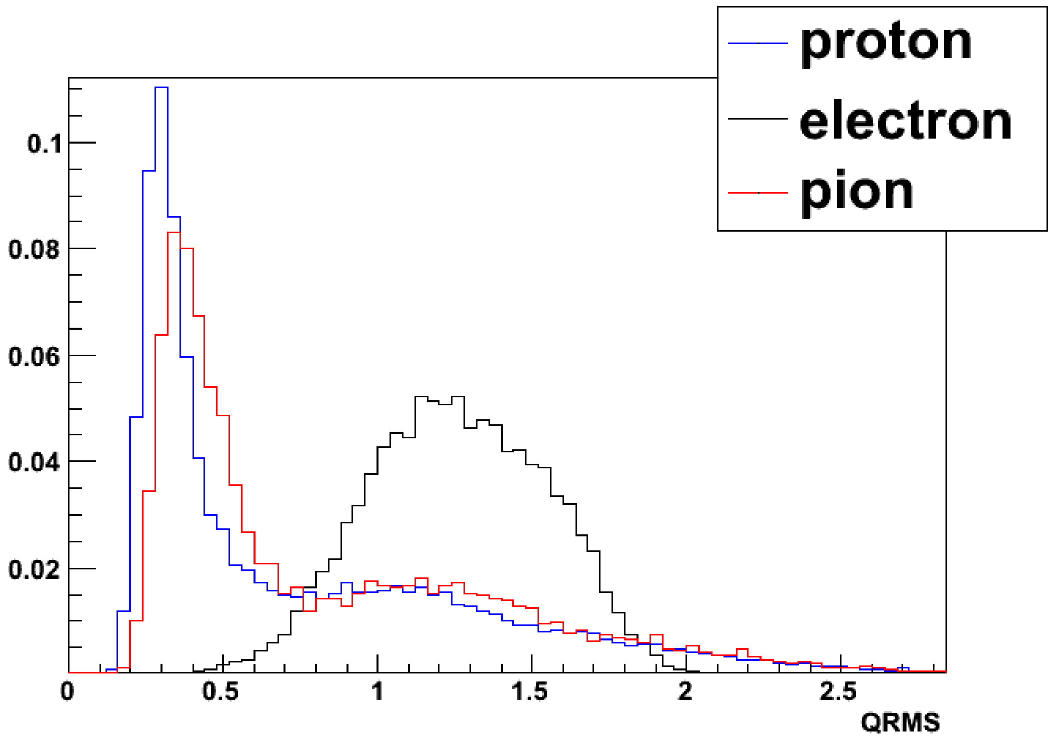

Figure 4.7: The QRMS, for proton, electron and pion.

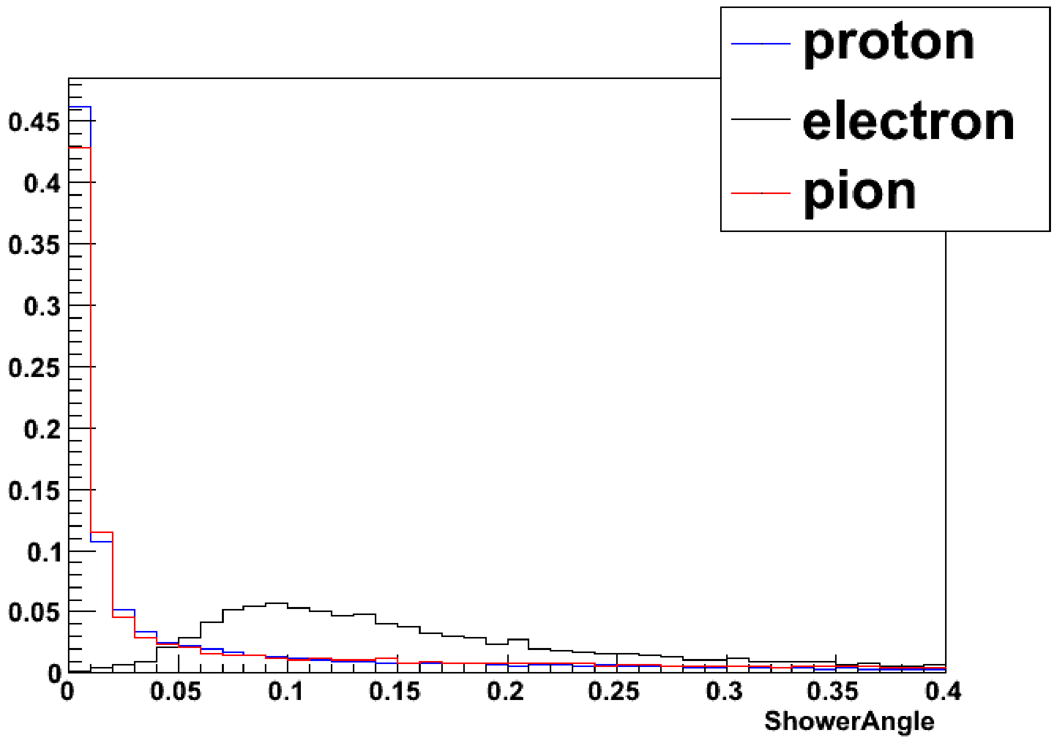

Figure 4.8: The ShowerAngle, for proton, electron and pion.

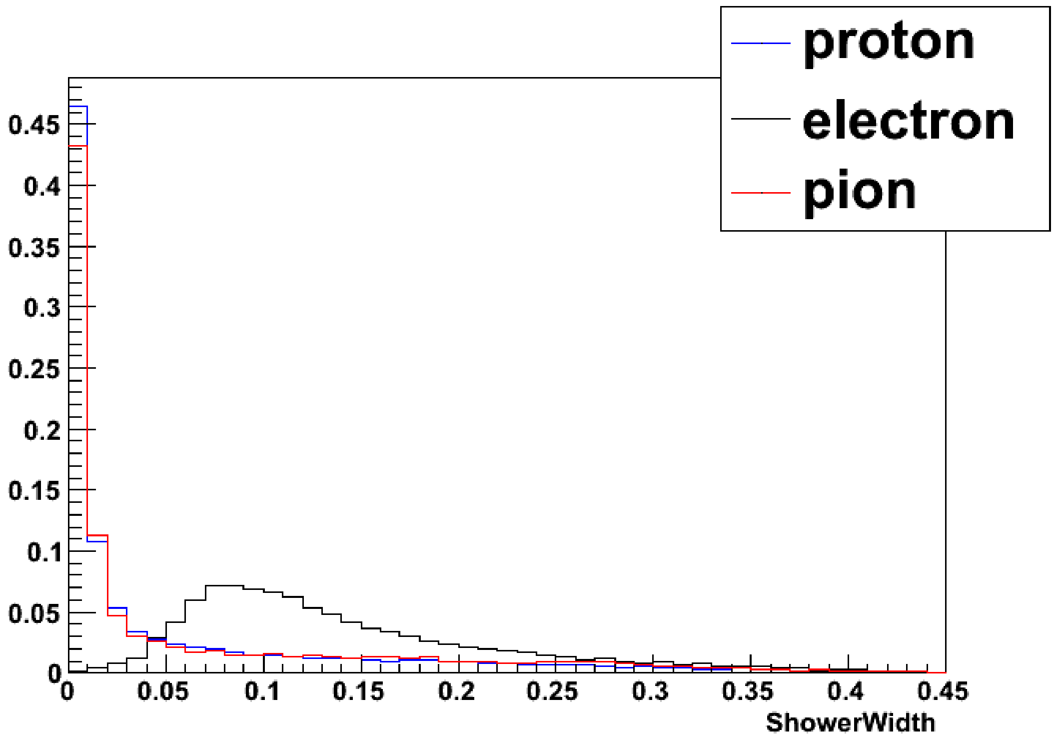

Figure 4.9: The ShowerWidth, for proton, electron and pion.

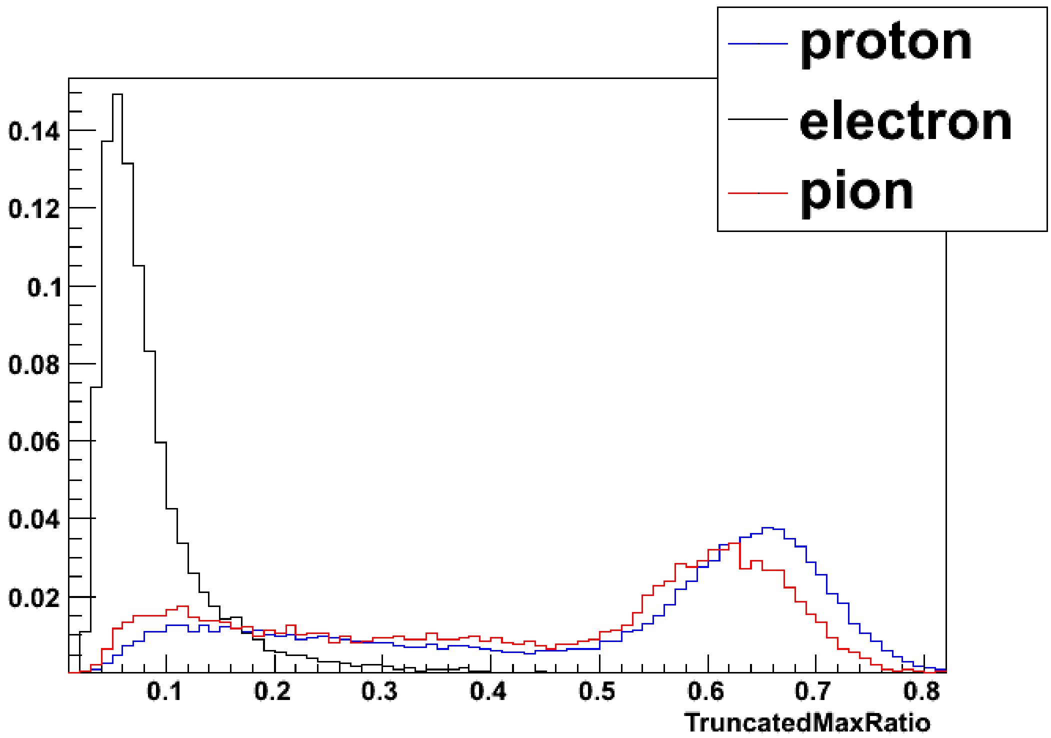

Figure 4.10: The TruncatedMaxRatio, for proton, electron and pion.

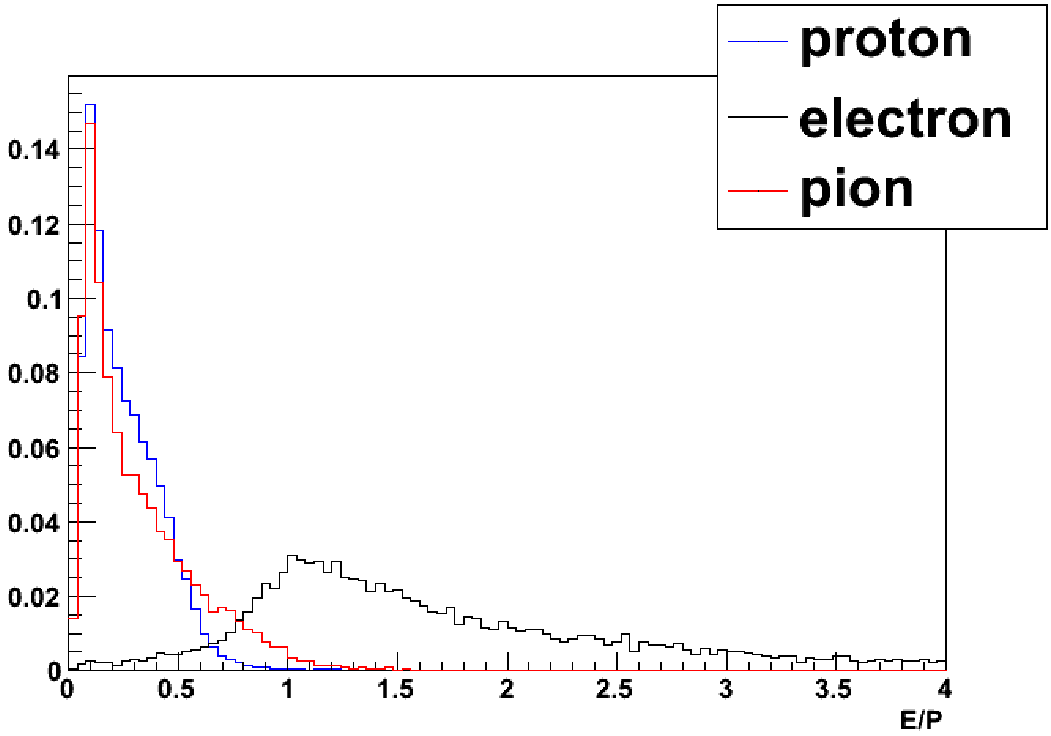

Figure 4.11: The E/p, for proton, electron and pion.

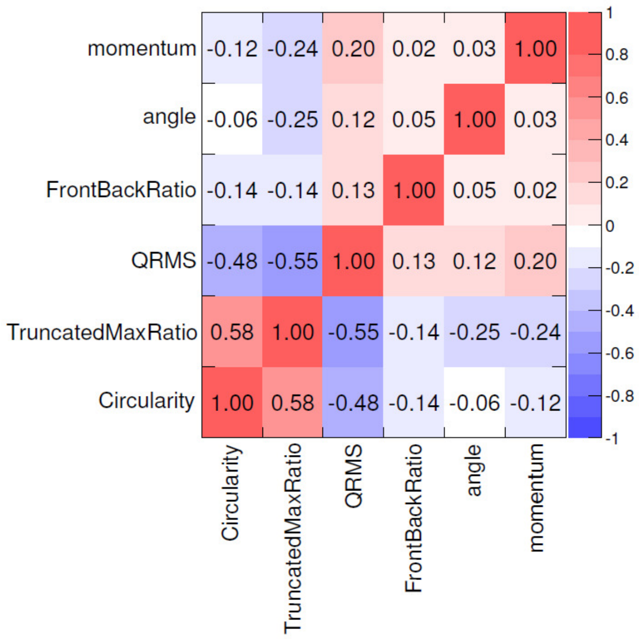

Figure 4.12: The Correlations of the production 5 PID variables calculated from DsE-Cal particle gun. Proton hypothesis, table taken from [8][9]

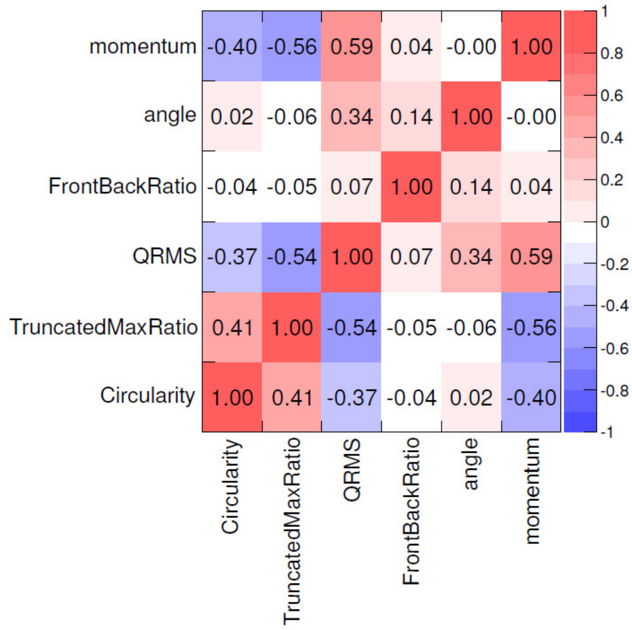

Figure 4.13: The Correlations of the production 5 PID variables calculated from DsECal particle gun.Electron hypothesis, table taken from [8][9]

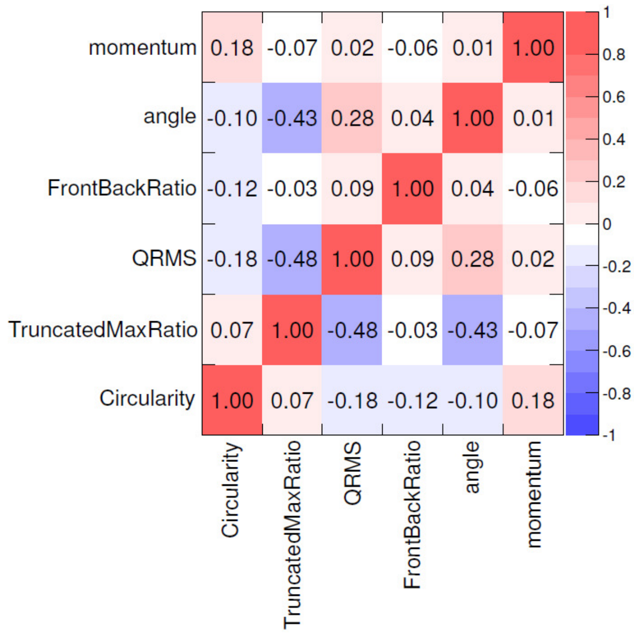

Figure 4.14: The Correlations of the production 5 PID variables calculated from DsECal particle gun. Muon hypothesis, table taken from [8][9]

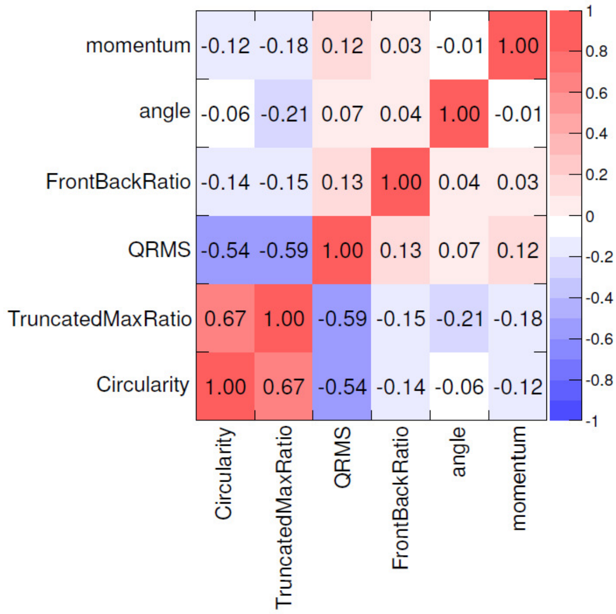

Figure 4.15: The Correlations of the production 5 PID variables calculated from DsECal particle gun. Pion hypothesis, table taken from [8][9]

4.4 Neural Network Optimisation

At this point, we are ready to set up and prepare the neural network for use. The first step is to create a training and a verification sample(fig 4.16). As we can discussed before, those two should come from the same sample, with 70% training and 30% verification. The MultiLayerPerceptron (MLP) algorithm can do that automatically once the training sample file is set. For the training/verification we generated a 1:1 signal to noise ratio, where the signal are the protons, and the background are the electrons,muons and pions. In the data, we expect most of the background (99%) to consist of those particles, so we generated a similar background. Also for momentum greater than $900 MeV/c$, the TPC can not distinguish between proton, muon and pion, and is difficult to reduce it without the neural network. The 1:1 ratio, is ideal for learning, since there is enough signal events for the neural network to learn to identify protons, and it is not required for the sample to mimic the Full Spill Monte Carlo.

The next step is to train the Neural Network (NNA) correctly, and to pre-

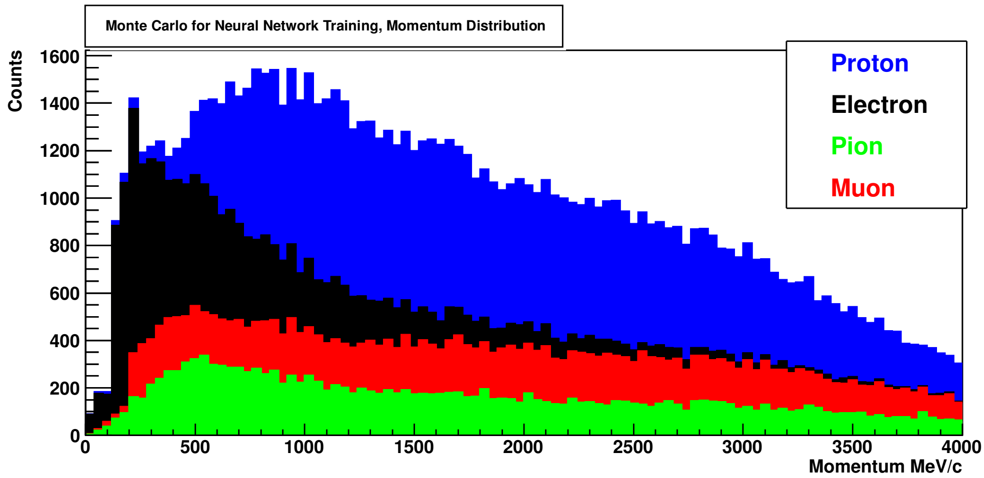

Figure 4.16: The Monte Carlo sample, momentum distribution, for Neural Network training.

vent overtraining. As we have seen, the MLP is learning in cycles (epochs), and each next cycle is improved with respect to the previous, by modifying the weights of the synapses. After each cycle the error is reduced, and a plot Error vs Epoch (fig 4.17) can help us decide when to stop our training. For this NNA, with the provided training MC sample, the optimum epoch is 150, since the curve reaches a plateau, and the error is not significantly reduced after that point. We know then that anything above 150 will overtrain our NNA, and will have a negative effect to the discriminating ability.

Until now, we didn't decide on the configuration of the NNA, thus we need to find the optimum number of hidden layers, and the number of nodes for each layer. Generally speaking, we should try to keep the system simple. Different configurations were compared, and concluded that the best set up is one hidden layer with eight nodes. For the comparison, we used the statistical test $Efficiency \times Purity$, and we found that a more complex configuration do not give better results, therefore we keep the most simple. Lastly, for better optimisation of the NNA, we created three momentum regions, and we study each one independently. The performance depends on the momentum, since the variables we use are momentum depended. Also we increase the overall performance, since the reduced performance in higher momenta (1GeV and above) do not affect the improved performance at lower momenta, for example when

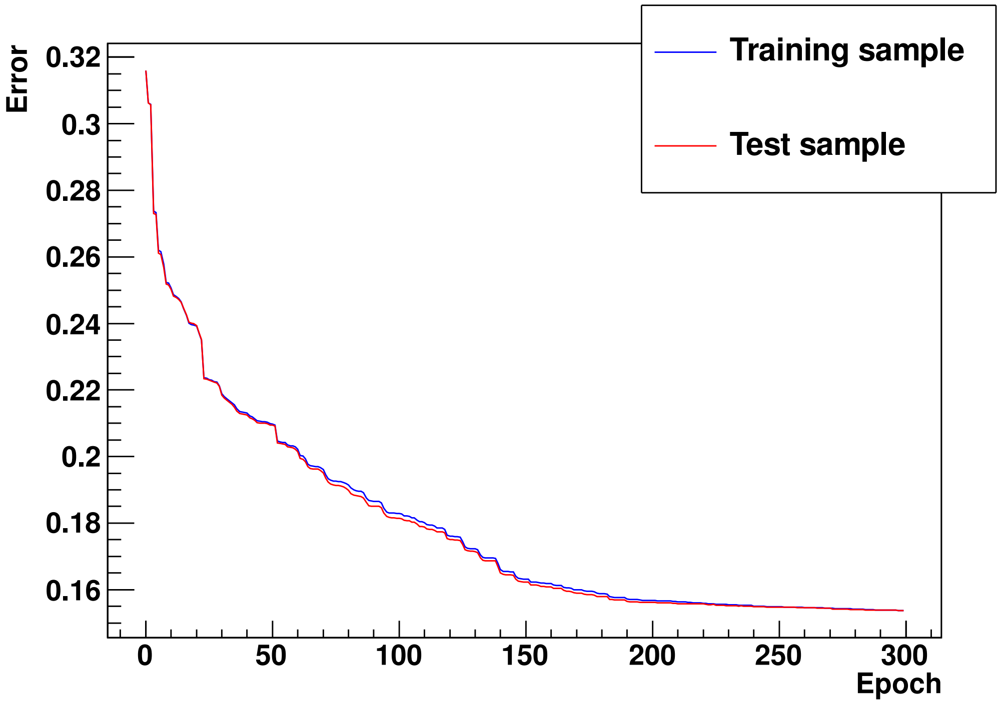

Figure 4.17: The Neural Network Epoch optimisation.

$p < 900 MeV/c$ it is easier to discriminate protons.

4.5 Validation and TestBeam results

After the set up and the training of the NNA (fig 4.18), before to use it on the selection, we had a validation test, to examine its performance and to verify that we get sensible results. An independent sample was generated, using MC ParticleGun, NEUT generator, keeping the same ratio we use for the training sample, and twice as many events. The validation was successful, and we can see (fig 4.19) there is a good discrimination between signal (blue) and background, even at higher momenta ($p > 800MeV/c$), which is the region where the NNA is needed most.

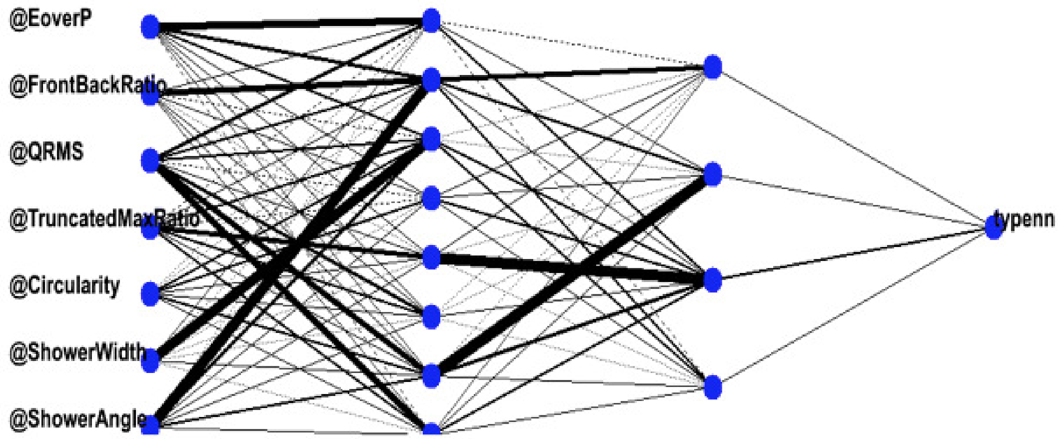

Figure 4.18: A visualisation of the Neural Network structure after training, thick line means more weight in the synapse.

For a second validation, we tested its performance on the TestBeam data which are independent of the MC sample we generated. The DsECal was taken to CERN in May and June 2009, to calibrate and test the detector. They used the facilities to fire protons, electrons, and pions upon the DsECal, at different angles (0, 15, 30, 60, and 75 degrees). Due to a mistake, the calorimeter was facing the opposite direction, so the particles were coming from back to front. At the testbeam the PID was performed using two Cerenkov detectors, and a counter to provide the Time of Flight (TOF). The two Cerenkovs give signal for electrons, and the TOF can discriminate between protons and electrons or pions. So by combining the two detectors, they could identify the particles, with high certainty. Though there was an unknown muon contamination

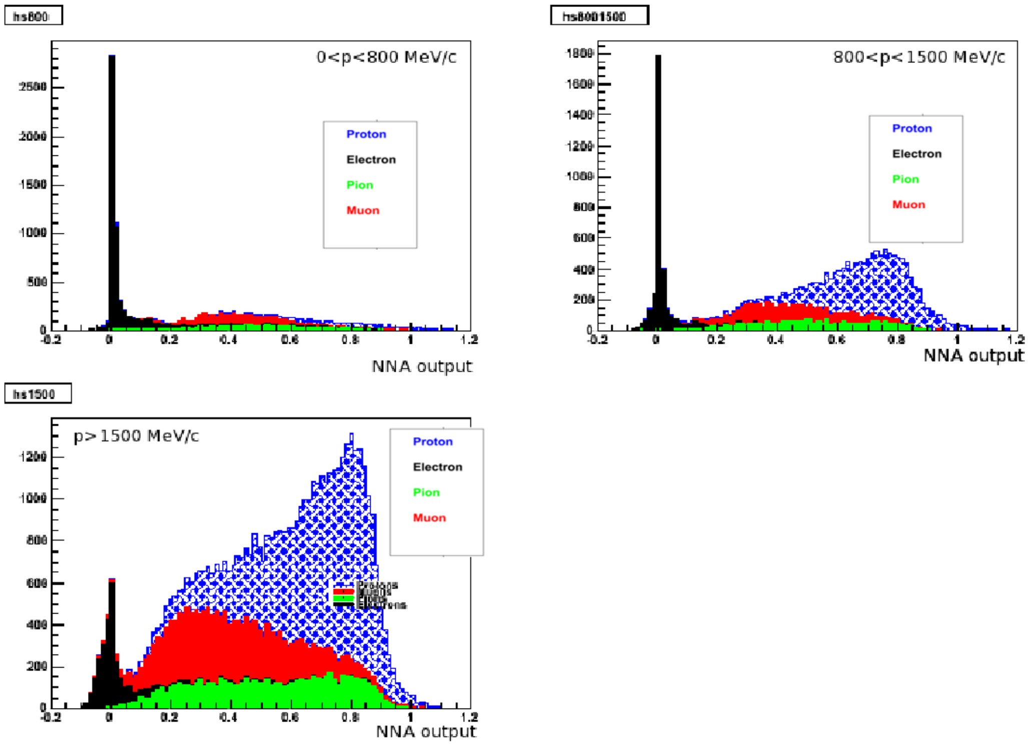

Figure 4.19: The output of MC PartiGun NNA, for the three momentum regions.

in the pion beam and this is an effect, impossible to simulate. The momentum was calculated, from the energy (provided by CERN) and the type of the particle. All this information is very important, as we produced a MC TestBeam, to compare the NNA output between MC and data.

One important difference between TestBeam and ND280 Data, is the momentum distribution. The TestBeam particles have momentum bunches, with particles having exactly the same momentum on each bunch (fig 4.20). On the other hand, the momentum for the ND280 is calculated with the TPC's, and is a reconstructed momentum. Therefore before to use the NNA on the TestBeam Data, we had to smear the momentum, to match the distribution we would get, as if we were using the TPC's (fig 4.21). The NNA was trained using reconstructed momentum, and we use it for the E/p variable. Without smearing the momentum, the NNA would have reduced discrimination, and increased error.

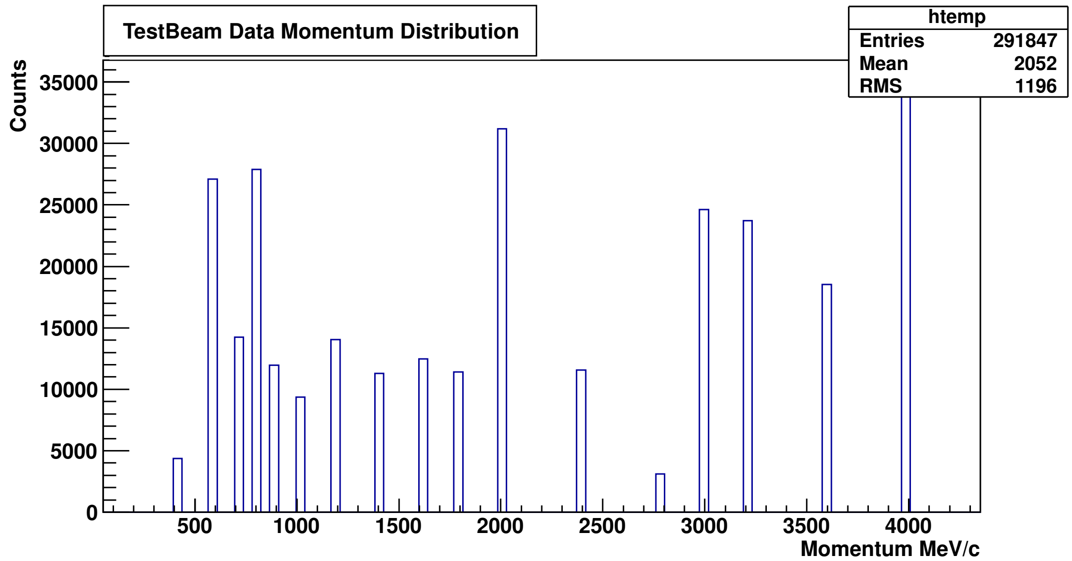

Figure 4.20: The TestBeam data domentum distribution.

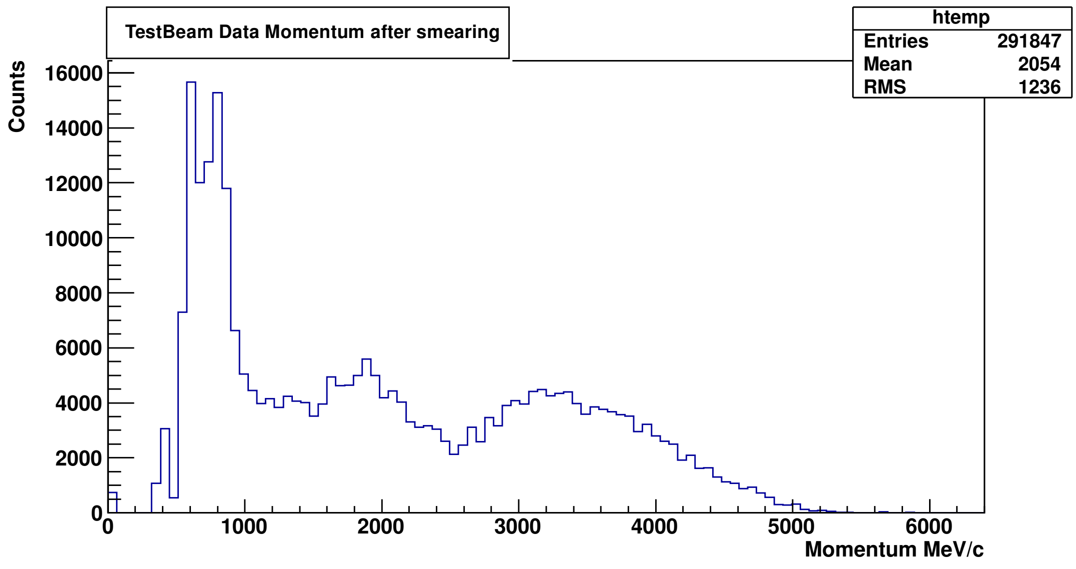

Figure 4.21: The TestBeam data with smeared momentum distribution.

A MC TestBeam Data sample was generated, to evaluate the NNA performance and is functioning as expected. For the MC we used the NEUT generator, at a 30 degree angle, keeping the same proportions for the particle mix, and momentum distribution as well. Since we don't know the muon contamination, we didn't include them, and we thus observe the differences between data and MC. We are mostly interested in the proton distribution which is our signal, and the output distributions of the NNA match. We expect to see differences, since the MC sample can not match the data perfectly (fig 4.22,4.23,4.24).

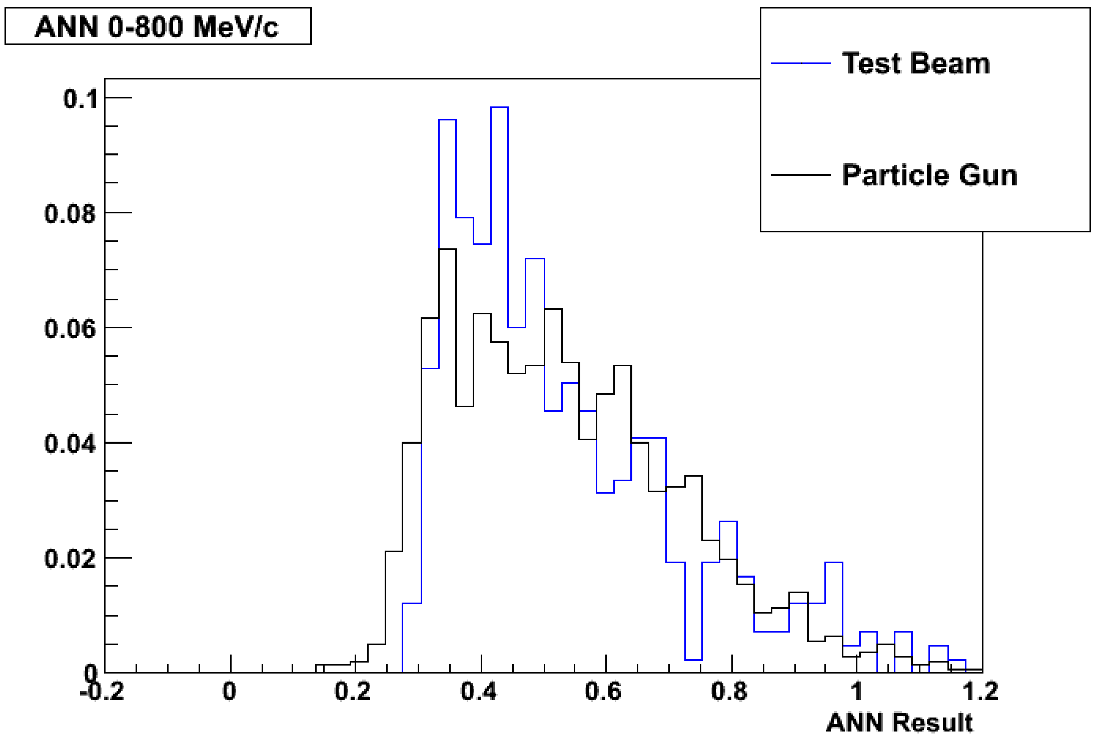

Figure 4.22: The NNA output TestBeam vs MC, momentum [0,800] MeV/c.

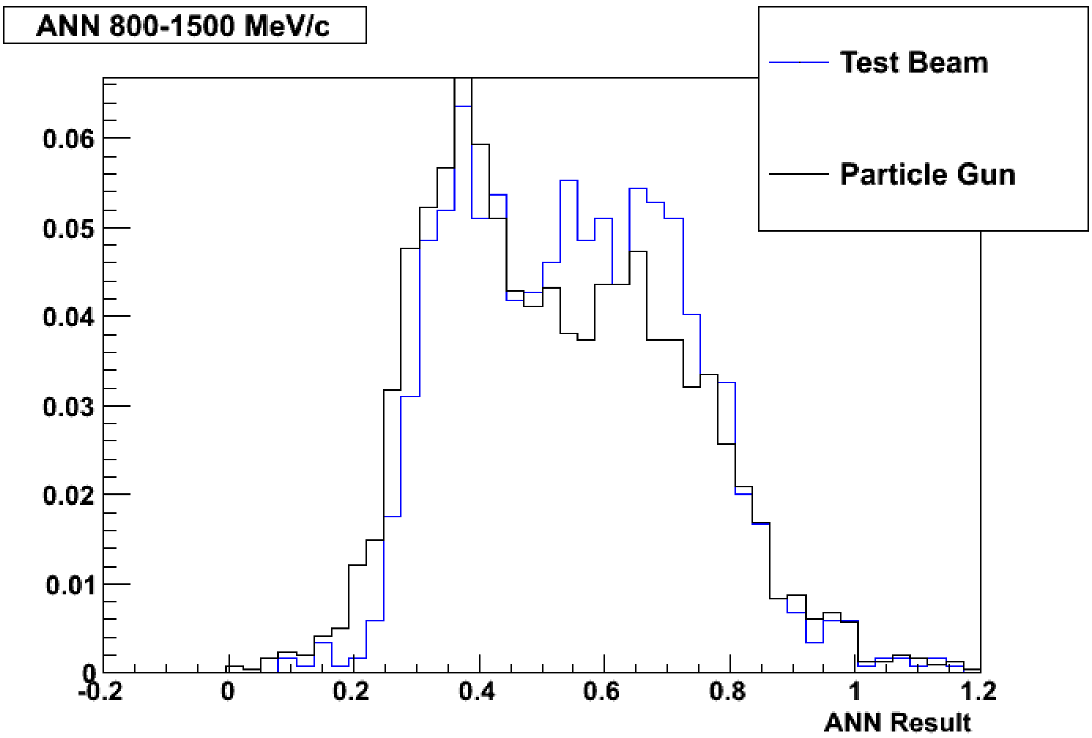

Figure 4.23: The NNA output TestBeam vs MC, momentum [800,1500] MeV/c.

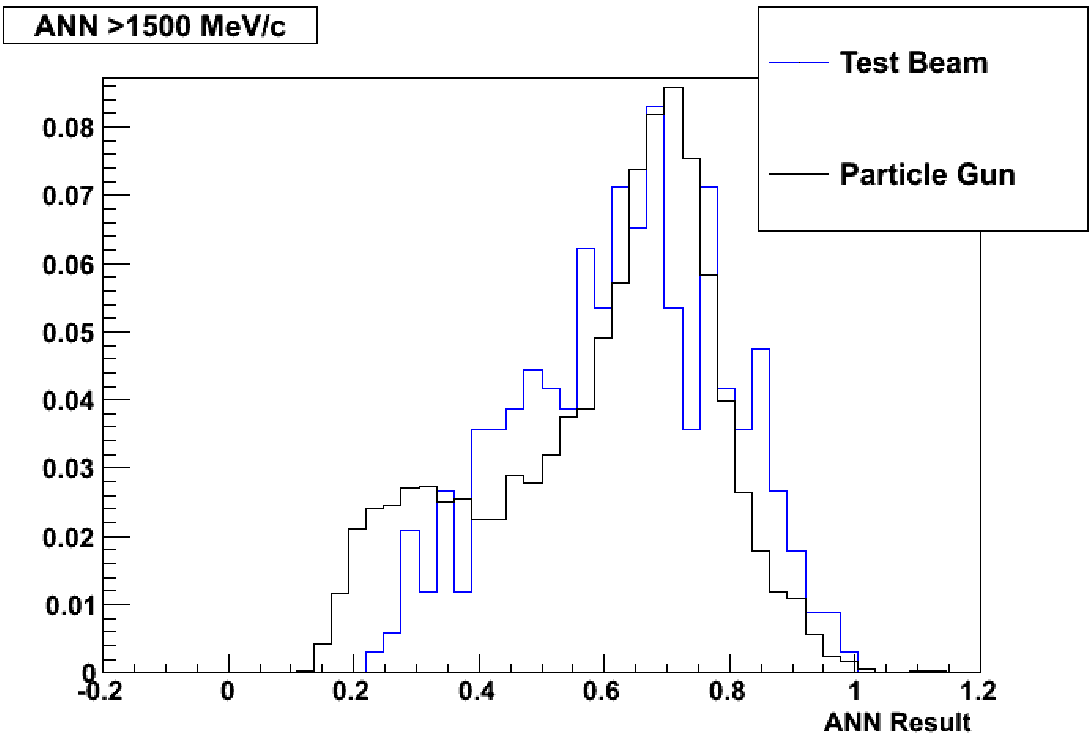

Figure 4.24: The NNA output TestBeam vs MC, momentum above 1500 MeV/c.

4.6 Results and Systematics

As we discussed, the NNA was developed to improve the proton purity, and include it in our PID. So far we have optimised the structure of the network, then we trained it, and tested it with MC and data. In the signal selection, we applied fiducial volume cuts and the vertex position is either in FGD1 or FGD2. Therefore, the neural network is analysing events, which start in the FGD's and enter the ECal. We have divided the selection in two parts, one for each FGD. The decision for that, is due to the different momentum distributions of the particles for the two FGD's. Events with vertex position inside the FGD1, which enter in the ECal, on average, have higher momentum with respect to events with vertex position in the FGD2. Also the background distribution is different, we see for example, the muon contamination is higher in the events starting in the first FGD. All the results we see come from the FUll Spill Monte Carlo with POT 2.4×10^{21} (fig 4.25).

We improve the overall efficiency, by using the NNA on the two selected samples independently. The main background are muons that passed the selection cuts. The TPC alone can not reject the muons, especially for momentum above 900 MeV/c, though the ECal PID variables have the potential to reject them. Based on the output of the NNA, we decide where to make a cut. For this analysis, we picked the output value with maximum $Efficiency \times Purity$, and we rejected all the events below that value. There are other statistical tests to quantify performance and help us choose the optimum value. They are all equivalent, so we are free to choose as long as we don't change in it the process. We have two FGD's and three momentum regions, therefore there are six individual cuts, one for each case. At the end we add the output files, after applying the cuts, to get the final purity. The NNA we created is doing all the calculations automatically and provides the final selection, without requiring any extra modification. The results presented show the work of the NNA done internally.

As we see (fig 4.26,4.27) at the NNA output for the selection, there are three momentum regions and two FGD's. For the first FGD, the optimum value to cut is 0.4

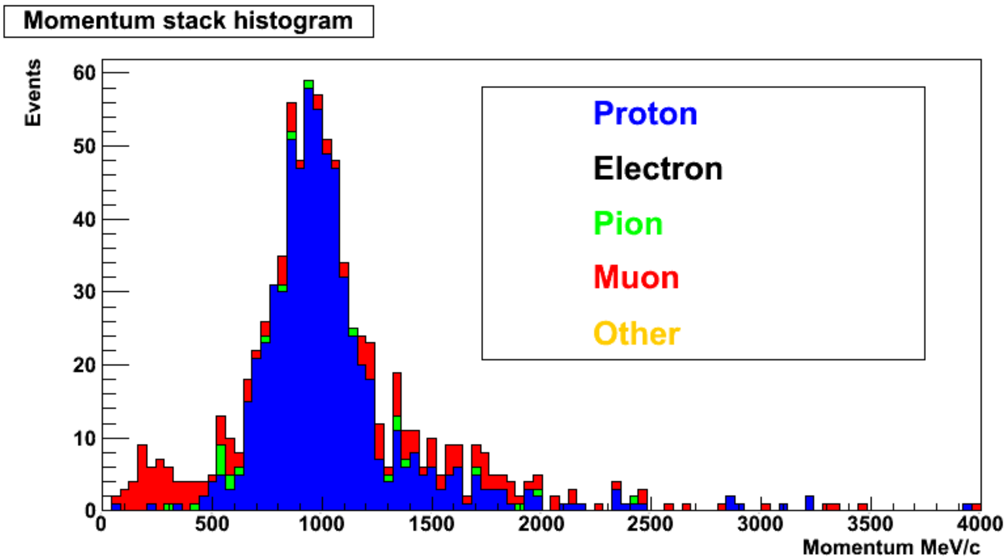

(a) FGD1

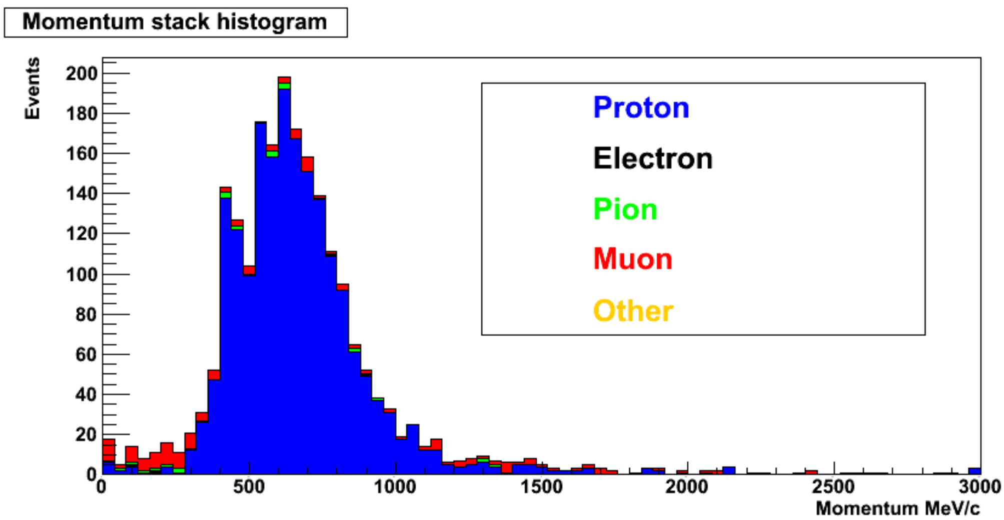

(b) FGD2

Figure 4.25: Momentum distribution for vertex position in the FGD1& 2.

for momentum $[0, 800]$ MeV/c, 0.4 for $[800, 1500]$ MeV/c and 0.5 for 1500 MeV/c and above. The values were calculated automatically, where the statistical test we use has it's maximum value. Similarly for the events with vertex in the FGD2 (fig 4.26,4.27), where it happens the values to be the same.

At this point we see the strength of the NNA, it is obvious that can clean the selection without losing much of our signal. For example in the FGD1, the muons were populating the low momentum region, and have been rejected. This is also true for the FGD2. This way we managed to reduce the background without momentum cut. By cutting on the momentum we could reduce the muons but we lose all the information from that momentum region. Kinematic cuts are our final option and only if every other method has failed. A kinematic cut is hard to justify and defend, since we can avoid it by using a neural network. Also the background at high momenta has also decreased, and those are good results, since at that momentum region, its virtually impossible to discriminate the proton if we only use the TPC. The energy loss curves converge and are useless for high energetic particles. The neural network was successful again, and is very efficient (fig 4.28).

As we discussed the NNA cleans the data, and gives one combined output, for both FGD's and for all momentum range. In the figure (fig 4.29) we see the momentum distribution for the proton, electron, muon and pion. We have achieved to improve the purity, in the whole momentum region, and this justifies the decision to use this method to improve the analysis. The rejection of background increased the purity up to 30% which is a remarkable performance, and we still have signal even where the background was dominating. We even see an improvement in the momentum region we already had high purity. This is also a verification that the NNA is working as expected, therefore we could trust the results we will get from the data. The neural network depends solely to the distributions of the input variables, since the MC match the Data closely, we should expect the NNA to have a similar performance on the data as well. Next, is to calculate the values of the errors.

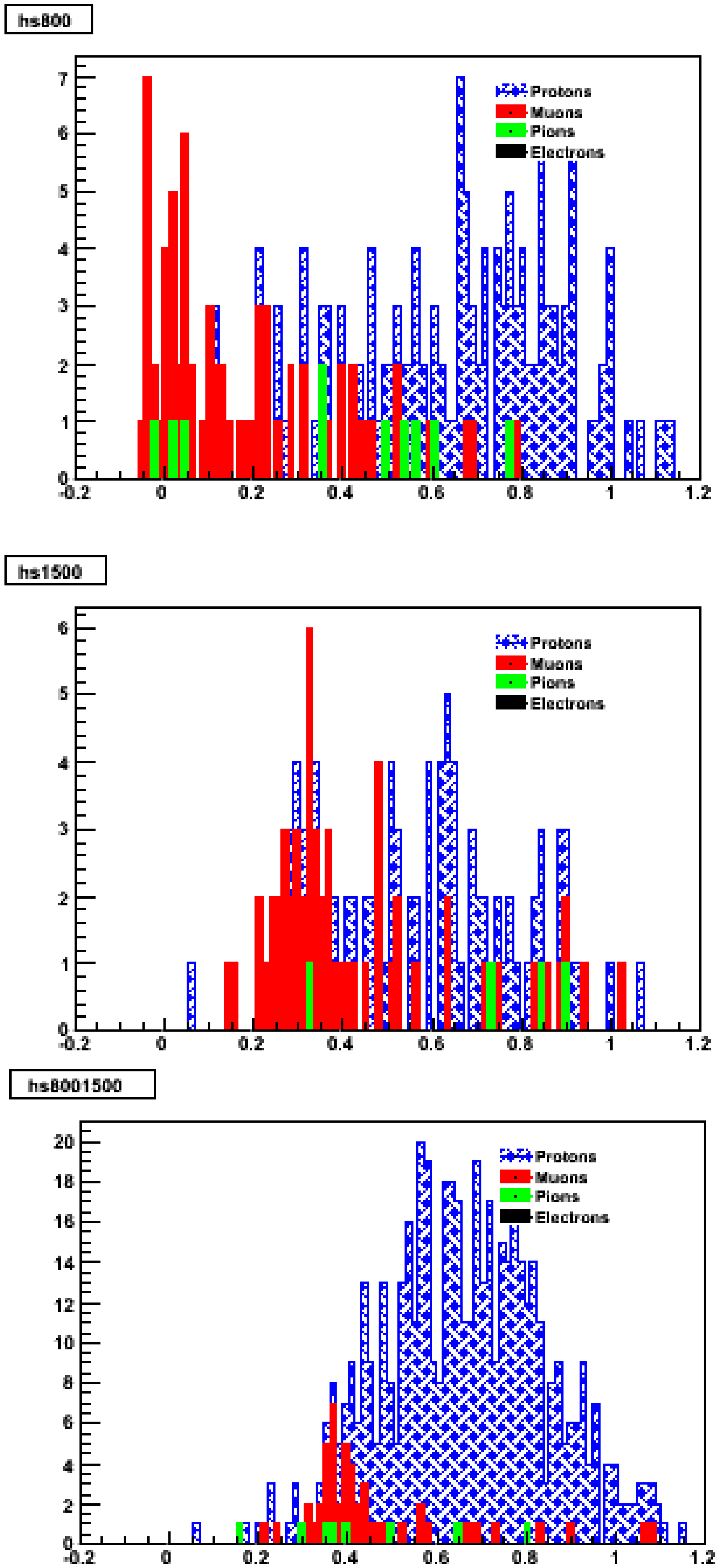

(a) FGD1

Figure 4.26: NNA output for vertex position in the FGD1. Blue is the signal.

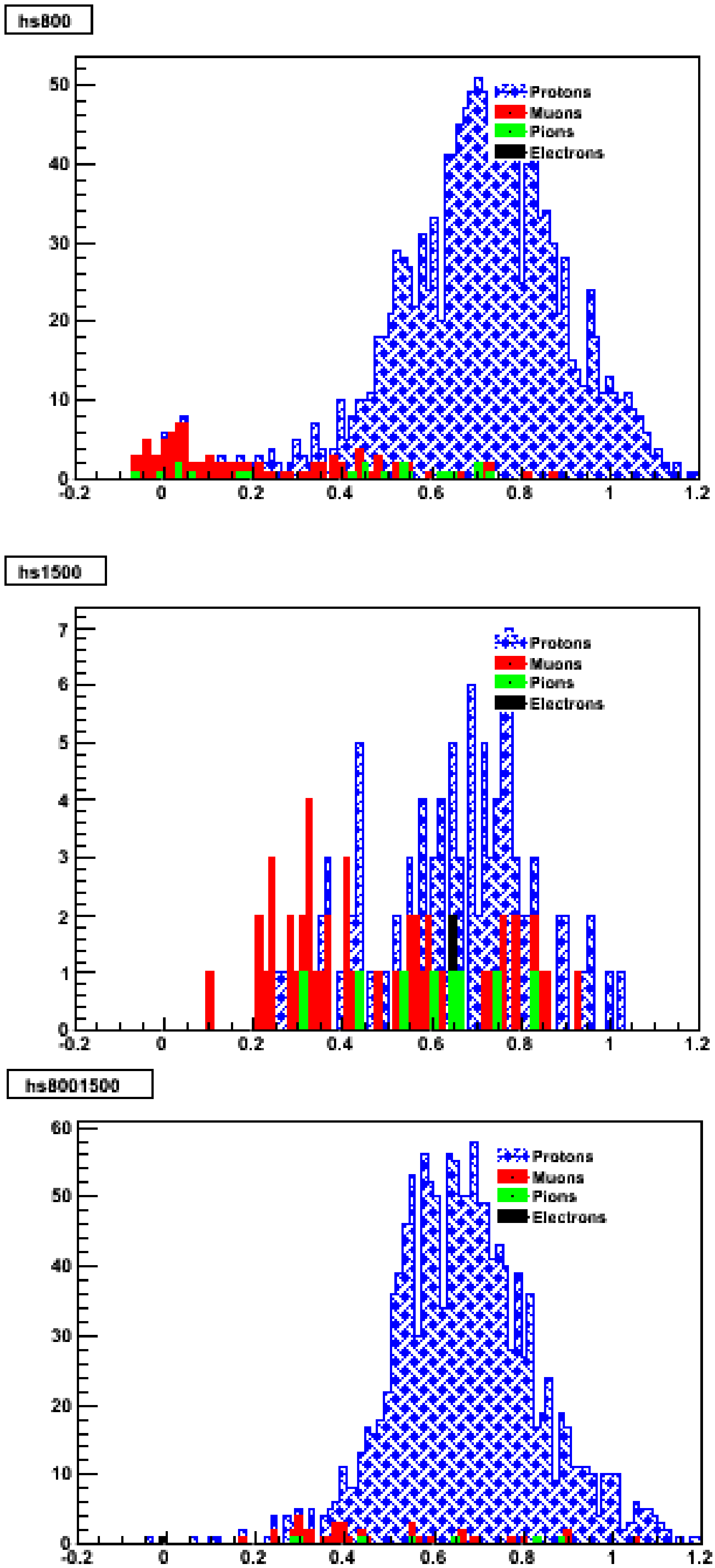

(a) FGD2

Figure 4.27: NNA output for vertex position in the FGD2. Blue is the signal.

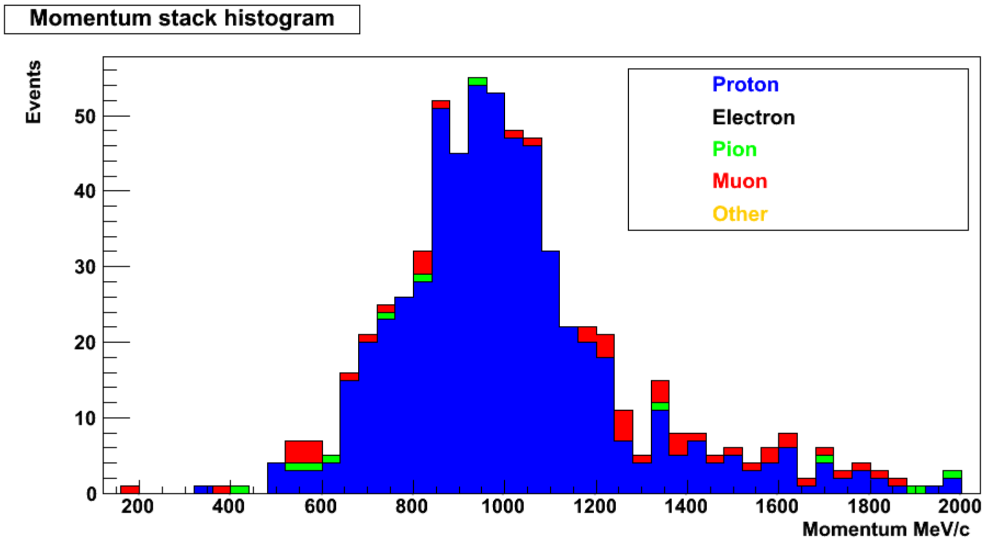

(a) FGD1

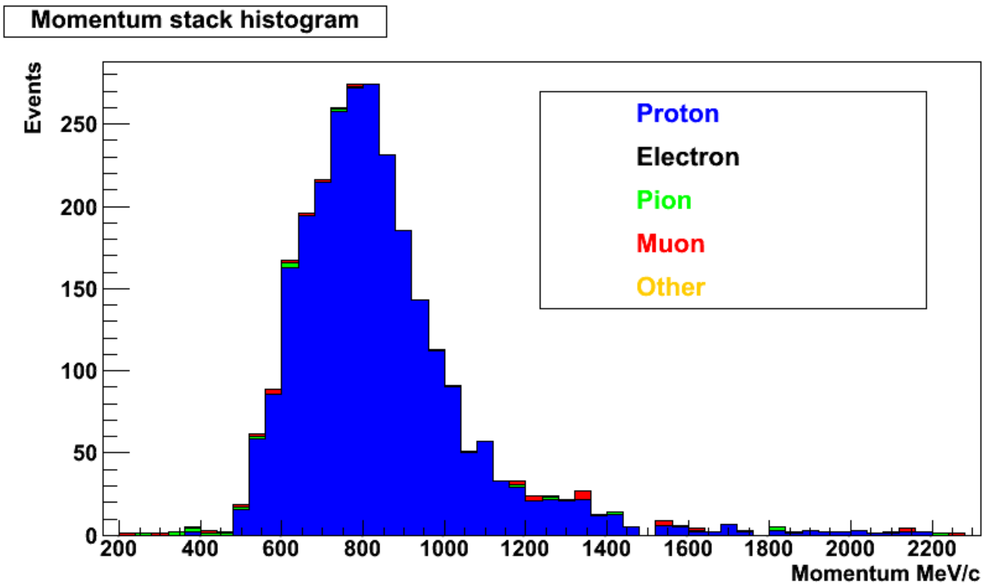

(b) FGD2

Figure 4.28: The Momentum distribution for vertex position in the FGD1 & 2 after NNA cut.

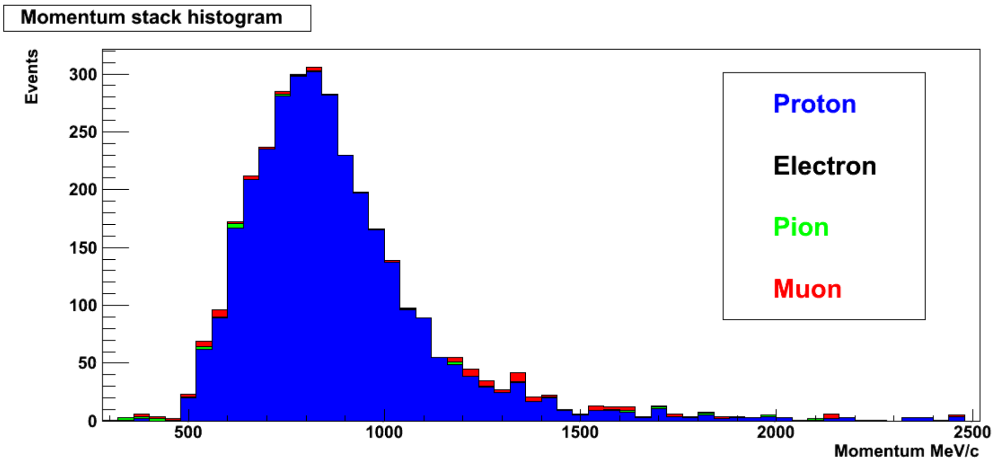

(a) Proton selection finalised, using the NNA and the TPC for all momentum regions.

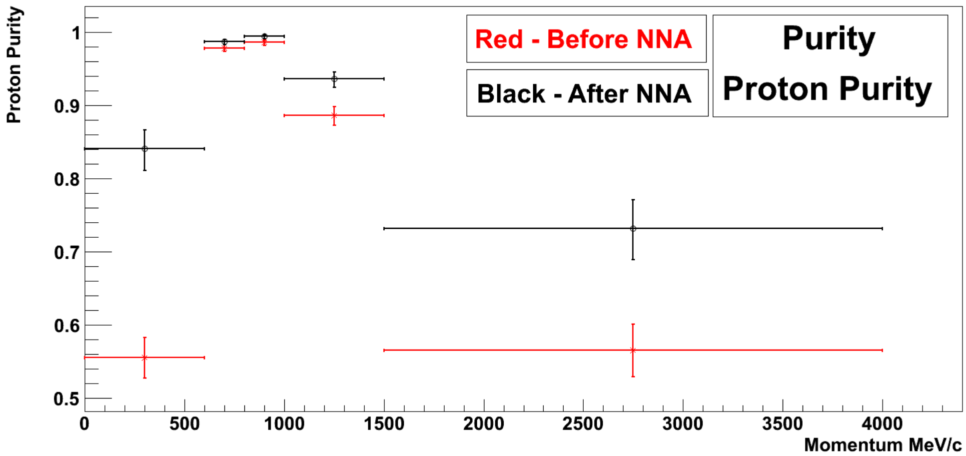

(b) Proton purity comparison, before and after the NNA.

Figure 4.29: The Momentum distribution and purity for vertex position in the FGD after NNA cut.

The last part of this section is the calculations of the systematic uncertainties. The Neural Network itself doesn't have any errors, so the systematics do not come from the network it self. As we discussed, the NNA makes decision based solely on the distributions of the variables. For example, two samples with differences in the ECal variables, will have different NNA output. This is true for the Data and MC, and we know there are differences due to a number of factors. The MC can never match perfectly the Data, so when we feed them in to the NNA, will get different efficiencies and purities. This difference in the efficiency should be added to the systematics of the analysis.

First we compare the input variables of the MC and Data, and then we modify the MC. We change each variable of the MC independently, so that it matches the Data. The variables Circularity, QRMS, FrontBackRatio, TruncatedMaxRatio and E/p follow a Gaussian distribution. Each MC variable had to change mean value, and spread (sigma σ). The mean value changed by shifting the distribution, and the sigma by smearing the events. The variables ShowerWidth and ShowerAngle are exponential distributions, and the MC was shifted and multiplied by a factor for each variable independently. All seven variables created a modified MC selection, identical to the original except the ECal variables match the Data (fig 4.30,4.31,4.32,4.33,4.34,4.35,4.36). We feed the new MC file in to the NNA, and we compared the efficiency difference of the output, for the same cuts, before and after the changes of the inputs. We calculated that there is a difference of about 3%, we lose about that amount of protons for exactly the same cuts. This number should be included to the final systematic of the measurement.

Here the NeuralNetwork is concluded, we have seen what is a NNA, and why is useful. Then we saw all the steps of the design and optimisation, then we did some validation studies, and at the end we run on MC and calculated the systematics. So we have a clear idea of the work that has been done and why all the steps were necessary to follow.

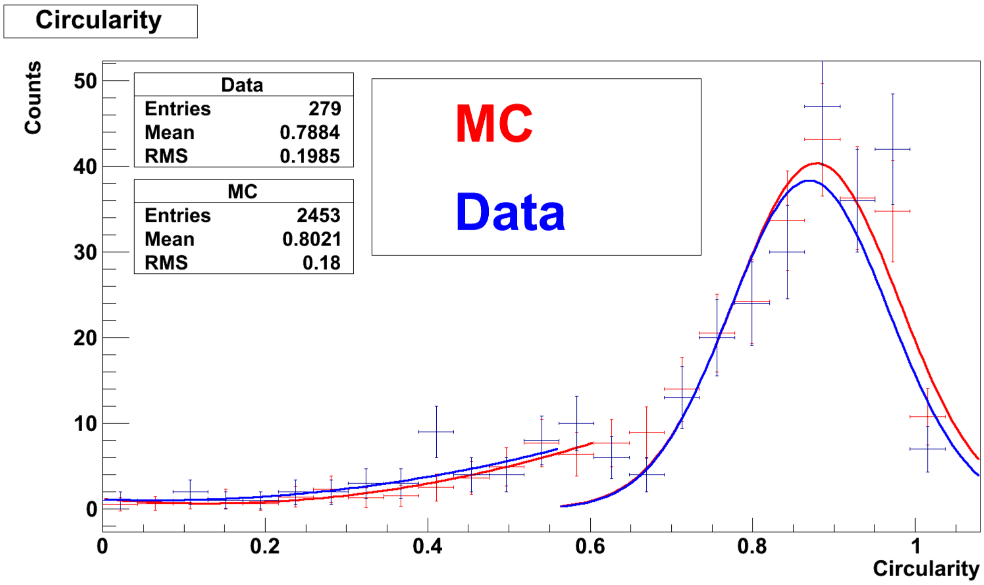

Figure 4.30: The plot of the modified MC variable Circularity to match the Data.

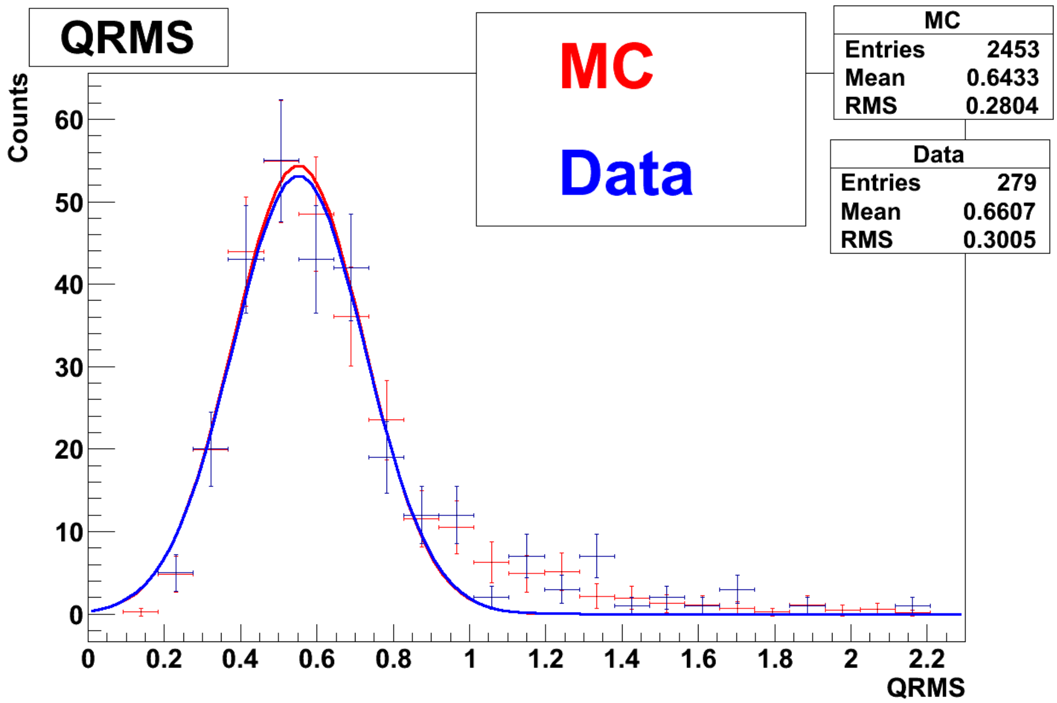

Figure 4.31: The plot of the modified MC variable QRMS to match the Data.

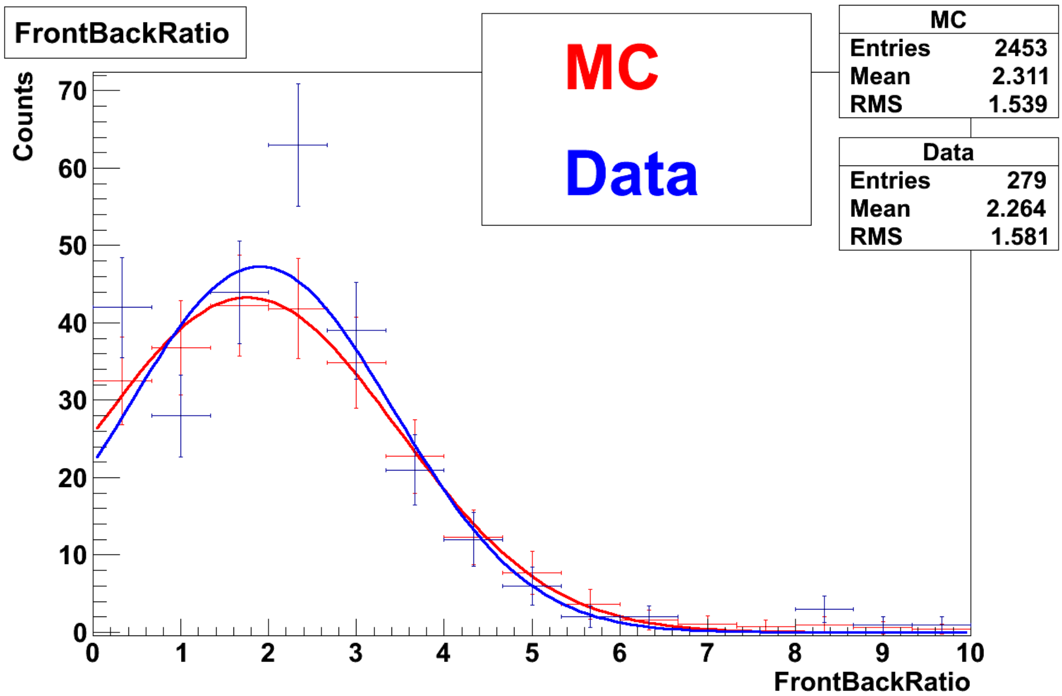

Figure 4.32: The plot of the modified MC variable FrontBackRatio to match the Data.

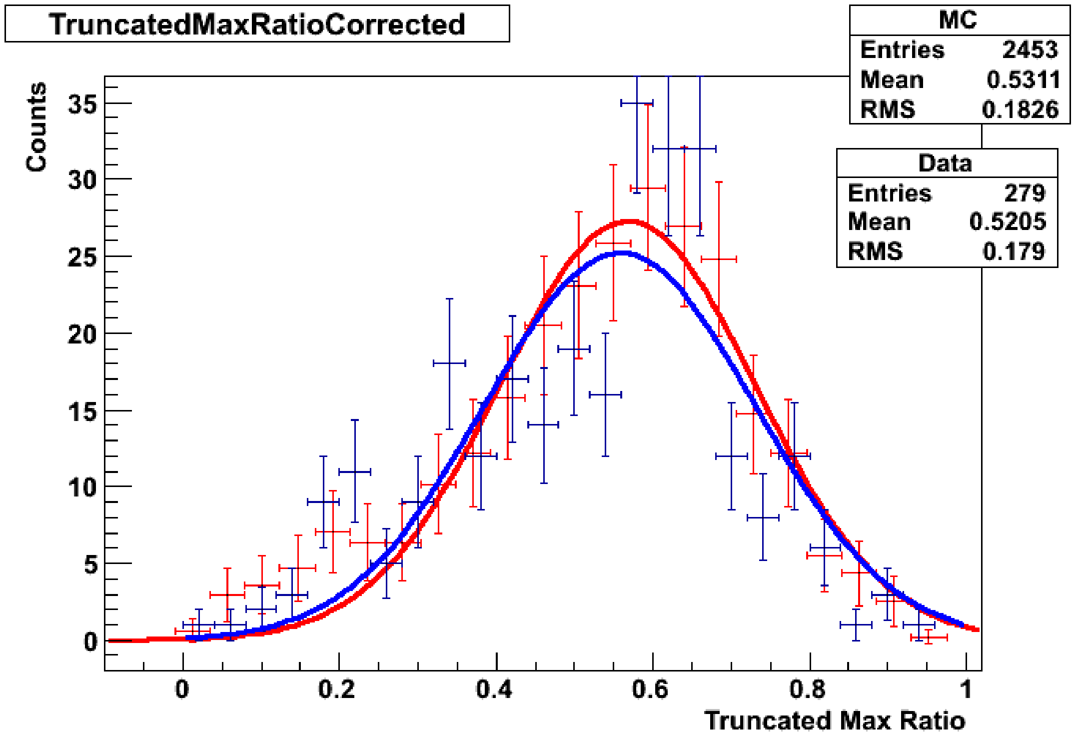

Figure 4.33: The plot of the modified MC variable TruncatedMaxRatio to match the Data.

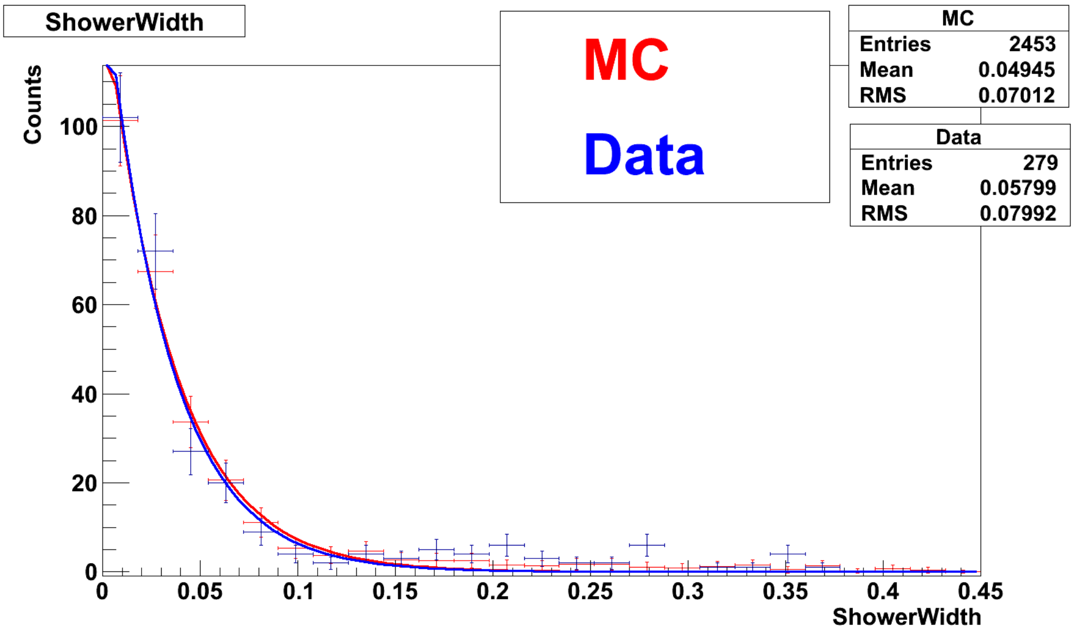

Figure 4.34: The plot of the modified MC variable ShowerWidth to match the Data.

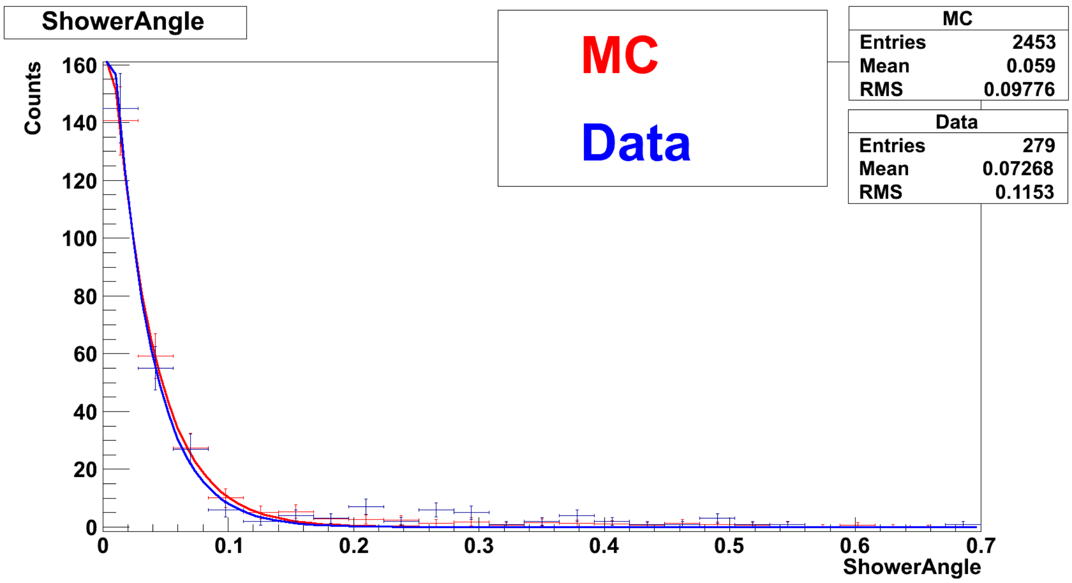

Figure 4.35: The plot of the modified MC variable ShowerAngle to match the Data.

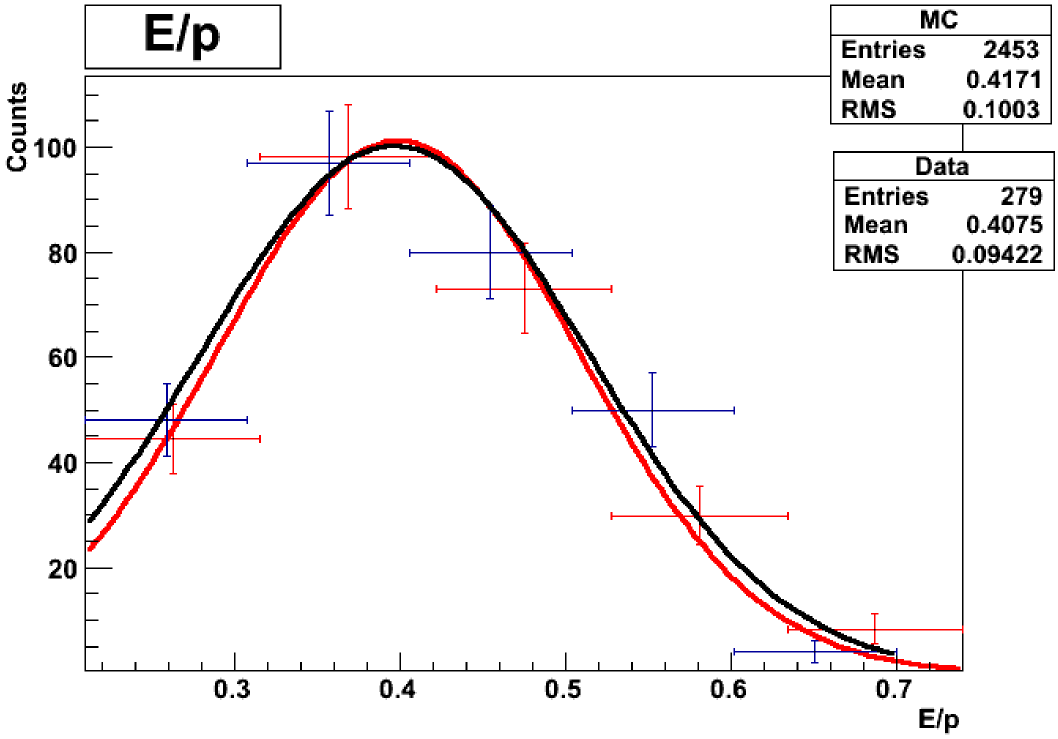

Figure 4.36: The plot of the modified MC variable E/p to match the Data.

Chapter 5

Systematic Uncertainties, and Measurement

The systematic uncertainties can be grouped in detector, beam flux and model uncertainties. The detector systematics is the largest systematics, since the flux and the model uncertainties cancel to a very good degree in the ratio. In particular the systematics of the detector are large, due to the secondary pion interactions and because of the mass systematics. The detector systematics are well understood, and calculated by the collaboration. The full ND280 MC software performs a complex and thorough simulation which includes the neutrino-nuclear interaction, the ND280 detector simulation and track propagation and the flux generation. A full re-simulation across the entire MC chain can remove any uncertainties but this is impractical due to CPU limits. The alternative is studying the effect of altering the input parameters and applying weights. Uncertainties could be propagated traditionally but an approach of throwing toys and calculating the resulting covariances is more durable given the often non-linear response functions. In general, the value of a systematic parameter is thrown according to its expected prior probability distribution, and the effect on the observables is propagated to the cross-section measurement to evaluate the systematic error [53].

5.1 Proton Control Sample

In order to calculate the systematic uncertainties of the Neural Network, and the proton pull in the TPC, a control sample of protons, independent of the proton selection, is required. The requirements are, the events in the control sample are not part of the proton selection, and to have very high proton purity (for the specific control sample, 93% of the particles are protons), with ECal activity. For the control sample, we picked charged current quasi elastic events with high momentum and kept only those (fig 5.1) with two tracks per vertex in the fiducial volume, with a proton and a muon in the final stage(fig 5.2). All the other events were rejected. This way the control sample is completely independent of my proton selection.

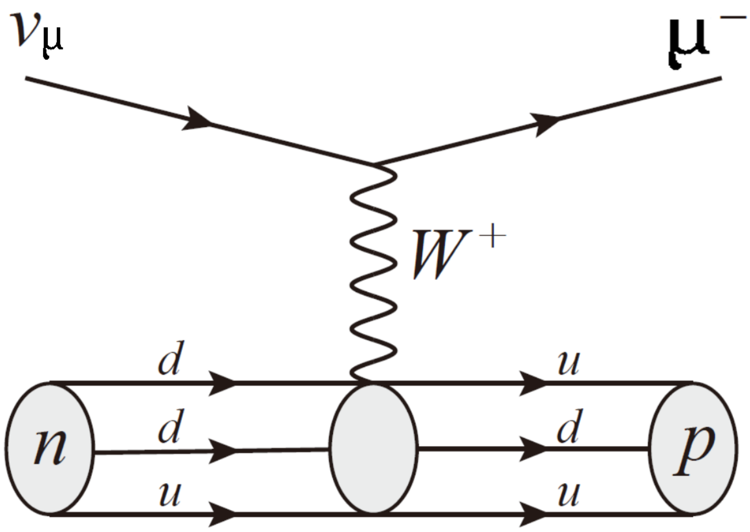

Figure 5.1: Feynman Diagram of Charged Current Quasi Elastic ν_μ interaction with nucleus.

We collected the protons, from the ν_μ charged current quasi elastic (CCQE) events with two tracks per vertex. In the ν_μ CCQE events, one track is negative (μ^-) and the other is positive (p^+), with activity in the ECal. The neutrino interacts with the nucleus and gives one muon and one proton at the final state. The negative track we reject, passes the TPC PID criteria for muons, while the positive track we collect is the proton. In order to increase the proton purity we implemented few extra cuts. First we collected events with momentum between 600-1400 MeV/c, so the TPC can

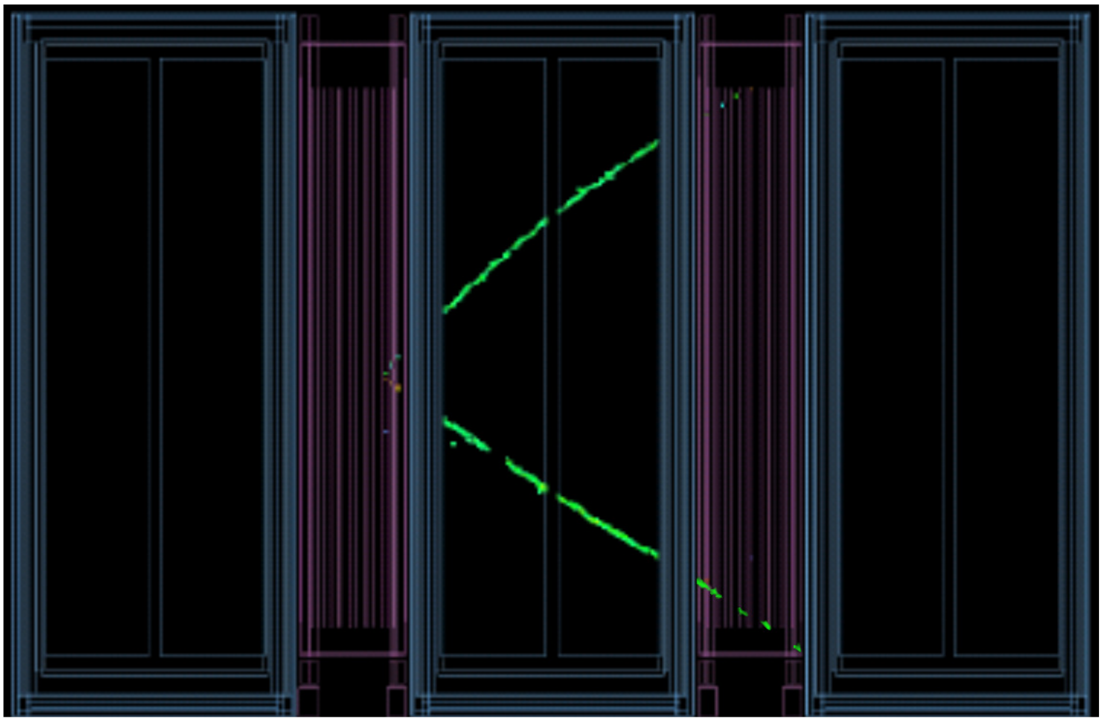

Figure 5.2: ND280 event display of Charged Current Quasi Elastic ν_{μ} with a proton and a muon at the final stage. Event number 50106.

discriminate the muons among other particles. Then we made cuts to the E/p and track length to reduce background. The protons do not travel far in the ECal, as they are heavier particles and interact easier than μ^+. So with the track length cut we remove most of the positive leptons. The E/p cut removes the positrons, since the protons do not produce an electromagnetic shower like the positrons. Thus the protons leave a clean trail while the positrons create an EM shower with spherical shape.

In the following figure (5.3) we see the energy loss with respect to the particle's momentum. The colours represent the density of the particles at each point. The shape of the distribution is expected as it follows the curve we get from the Bethe-Bloch formula for the protons. So it validates that the particles are protons and the TPC can identify them. At the bottom of the same figure (5.3), there is a distinct second distribution below the curve of the protons. Those events are probably the pions and the positive muons, as predicted from the Bethe-Bloch formula.

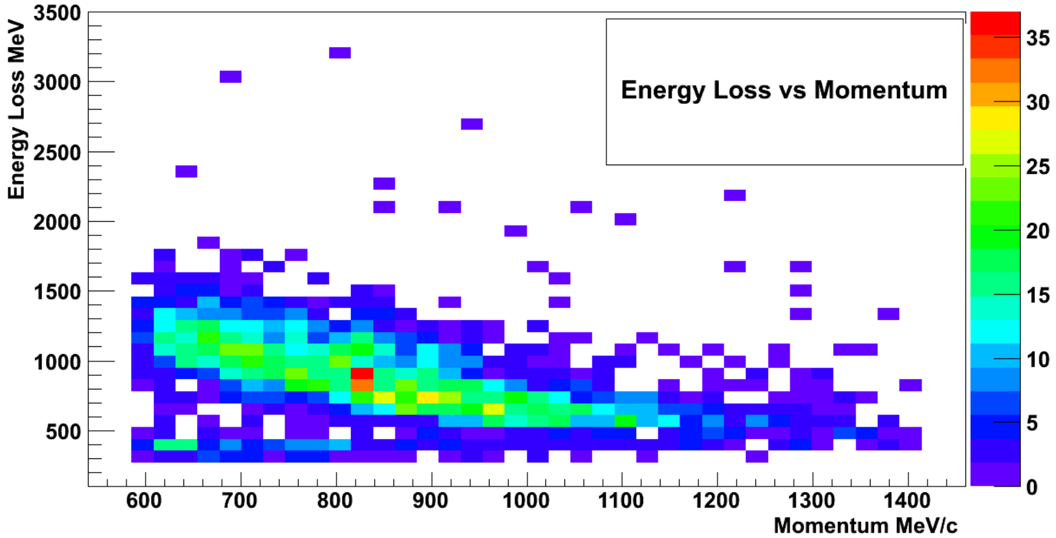

Figure 5.3: Total energy loss for a particle, traveling through the detector.

In the figure (5.4), we see the momentum distribution of the particles in the control sample. The high energy protons is our signal, and the background is consisted of pions, muons and electrons. In accordance to the theory we have mostly muons and pions in our background. The purity is increasing with the momentum as we have less background due to the kinematics of the interaction.

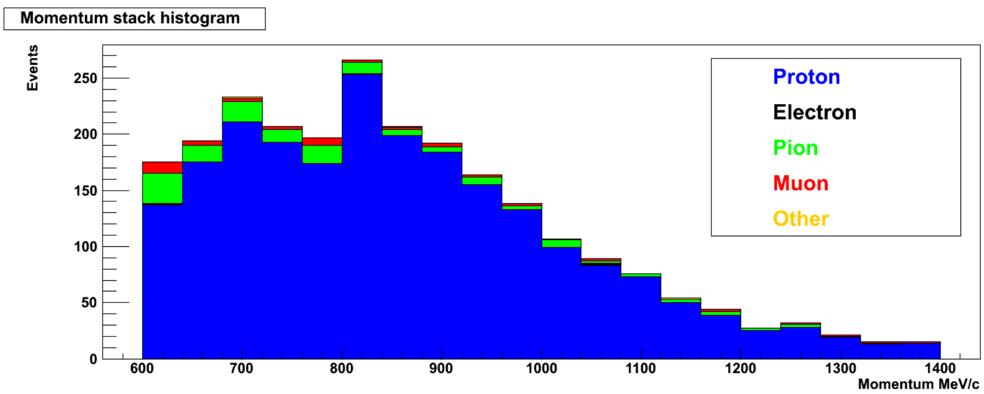

Figure 5.4: Particle type that pass the selection criteria, for the proton control sample.

Lastly we see the proton purity of our control sample in the figure (fig 5.5), for all our momentum range. While the total proton purity is approximately 93%, we see that for momentum between 800 – 1000MeV/c, the purity is almost 100% and this is the range where the TPC can perform best. The proton purity for low momentum is lower, as we do not have many low energy protons coming from CCQE interactions. Overall this selection is clear enough to calculate our systematics, and the contribution of the background is very small.

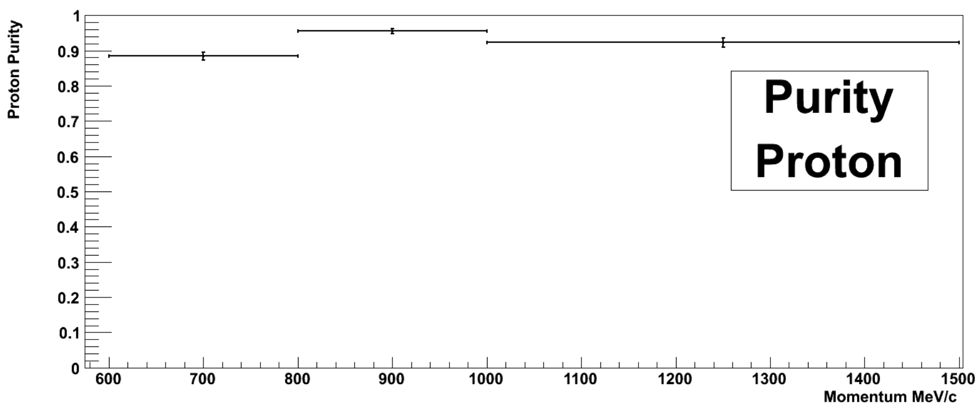

Figure 5.5: Proton purity of the control sample, with respect to the momentum.

5.2 Neural Net Systematics

To calculate the neural network systematics we had to produce an independent MC and Data sample. Then I compared the distribution of the Data versus the Monte Carlo, for each input variable. After that I created a large number of MC toys, and I let each variable to approximate the Data and for each toy I measured the purity of the sample and the efficiency of the Neural Net. The efficiency is defined as the number of protons that pass the criteria over the total number of protons in the sample. Each variable independently is changing the neural network efficiency when is changing value. I repeated the process 250 times for each variable, and I plotted the results to find the mean value and the error of the normal distribution. Finally I repeated the above process, while I let all the variables free to change value simultaneously, to see the change of the neural network efficiency so to calculate the overall systematics.

The table below summarise the standard error of the neural net efficiency for all the input variables.

NNA Variable	Fractional error σ%
E/p (fig 5.6)	8.32×10^{-2}%
QRMS (fig 5.9)	1.74×10^{-1}%
FrontBackRatio (fig 5.7)	4.22×10^{-1}%
Circularity (fig 5.8)	5.15×10^{-1}%
TruncatedMaxRatio (fig 5.10)	5.73×10^{-2}%
ShowerAngle (fig 5.11)	7.19×10^{-2}%
ShowerWidth (fig 5.12)	6.56×10^{-2}%
Overall error of the NNA (fig 5.13)	2.28%

The total standard error σ, of the mean value of the NNA efficiency is 2.28×10^{-2}. Calculated from all the input variables, for 250 toys.

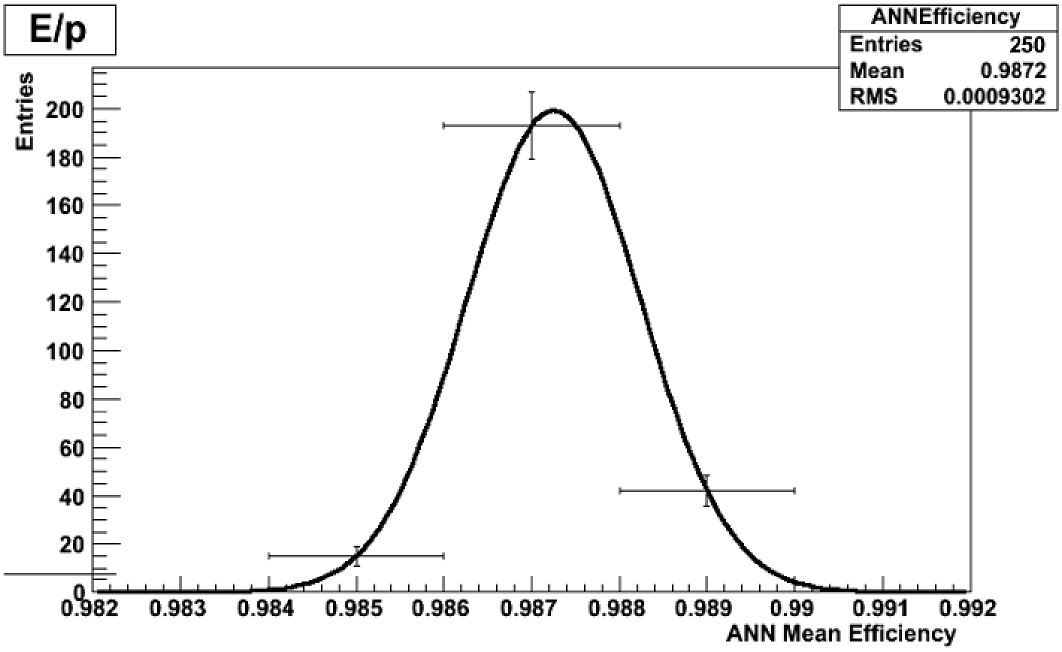

Figure 5.6: The neural net efficiency, for the input variable E/p, for 250 toys.

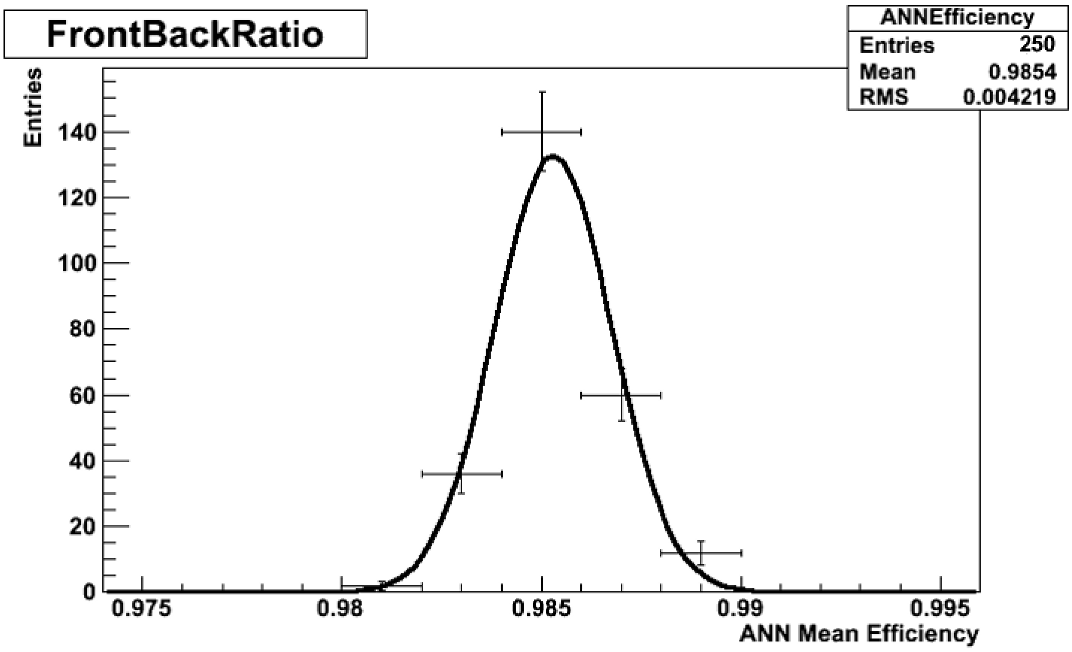

Figure 5.7: The neural net efficiency, for the input variable FrontBackRatio, for 250 toys.

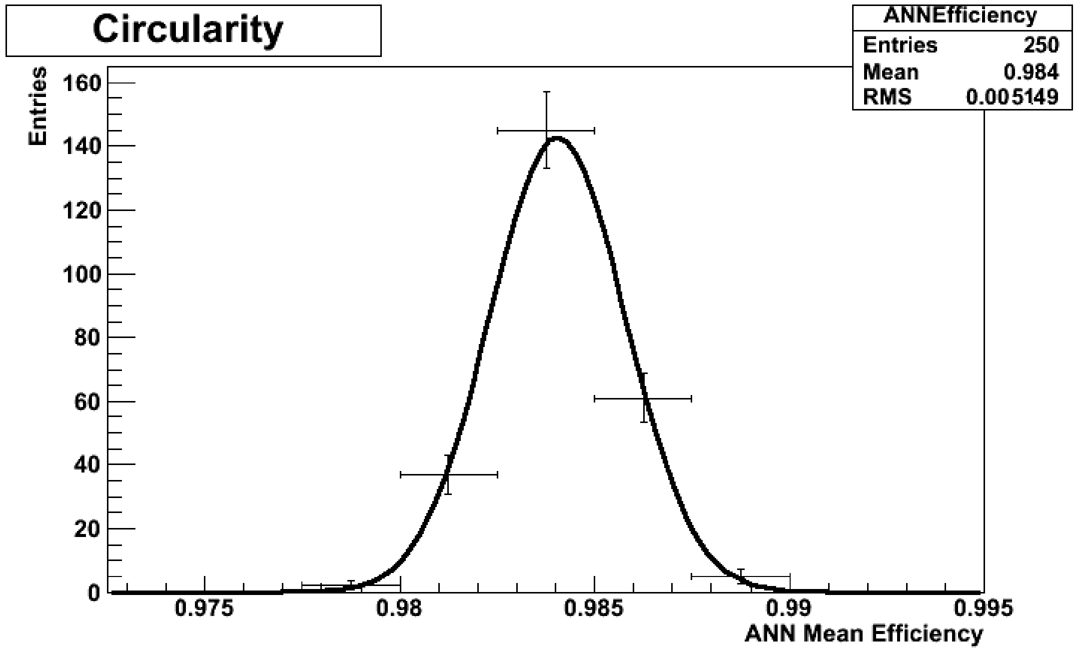

Figure 5.8: The mean value of the neural net efficiency, for the input variable Circularity, for 250 toys.

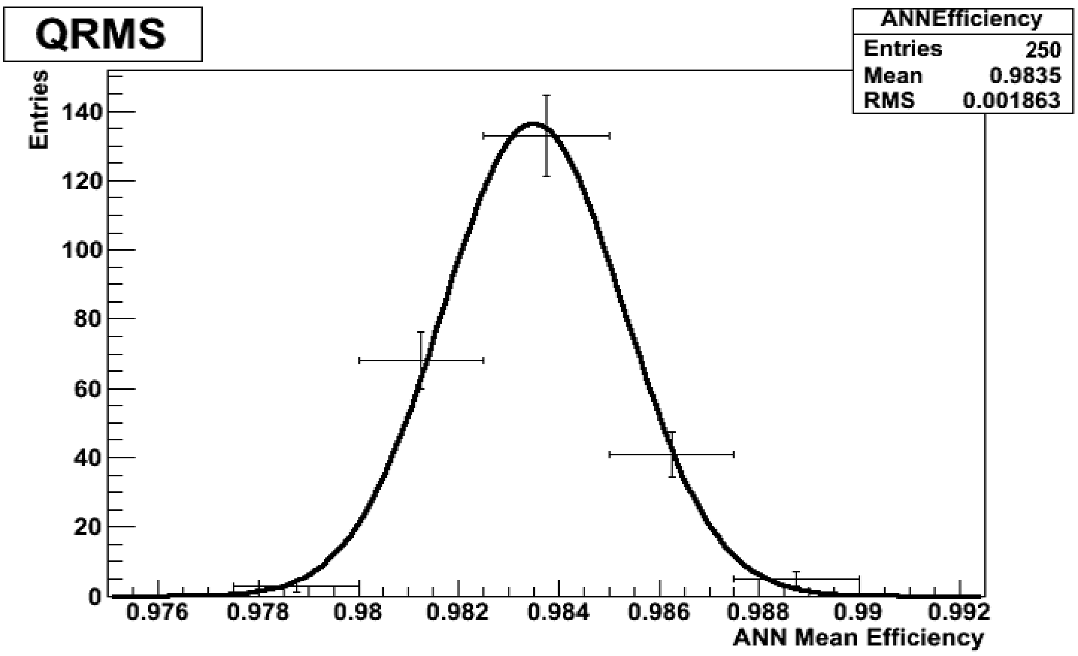

Figure 5.9: The neural net efficiency, for the input variable QRMS, for 250 toys.

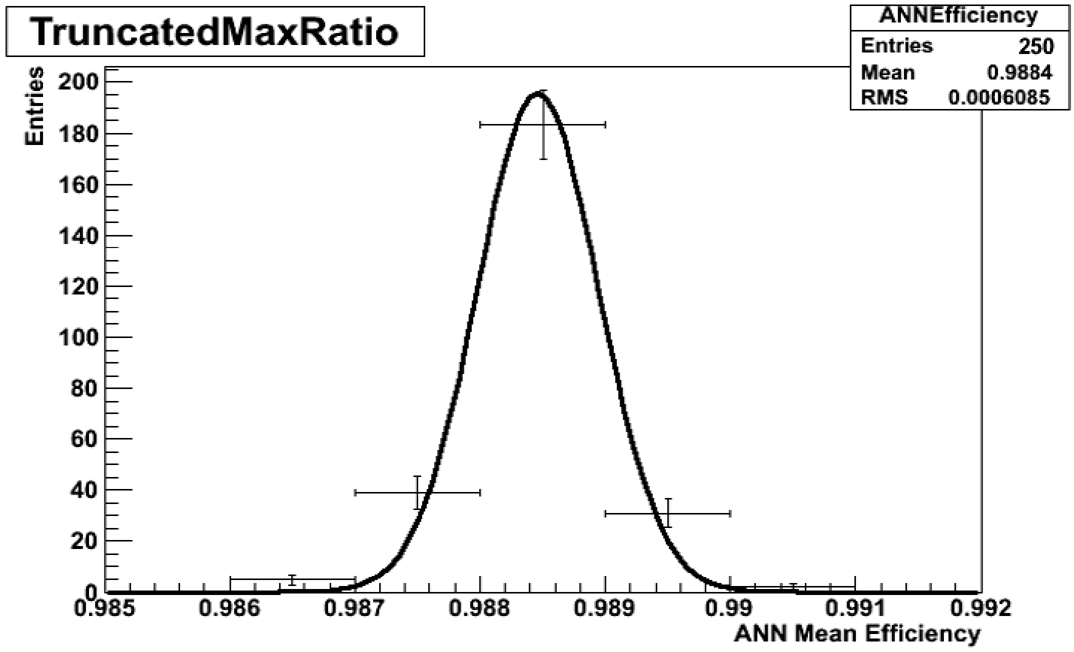

Figure 5.10: The neural net efficiency, for the input variable TruncatedMaxRatio, for 250 toys.

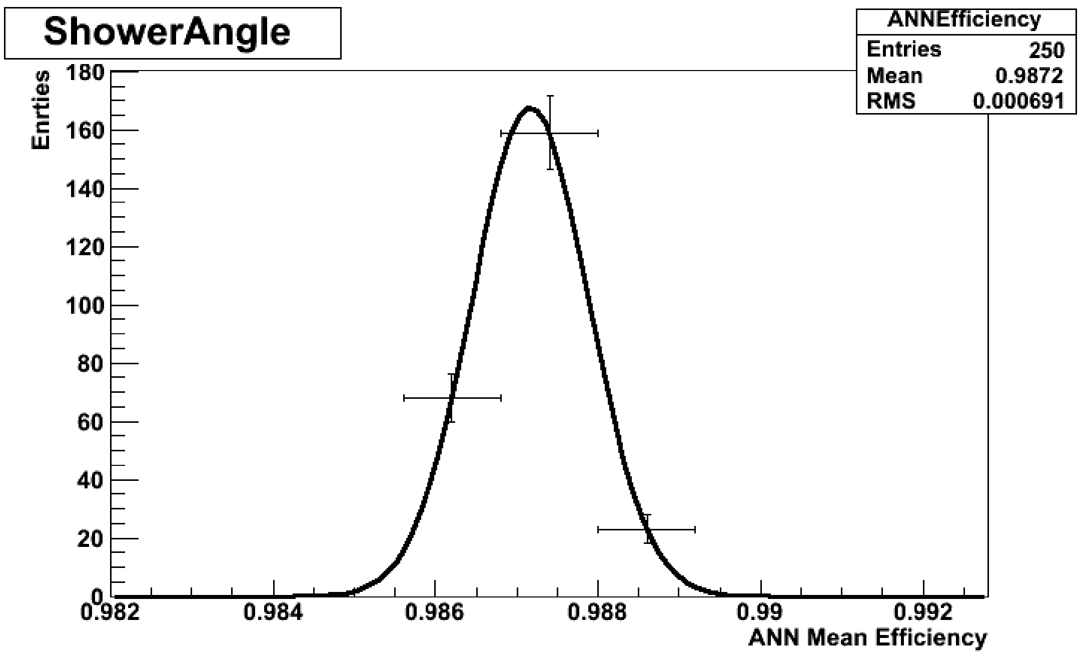

Figure 5.11: The neural net efficiency, for the input variable ShowerAngle, for 250 toys.

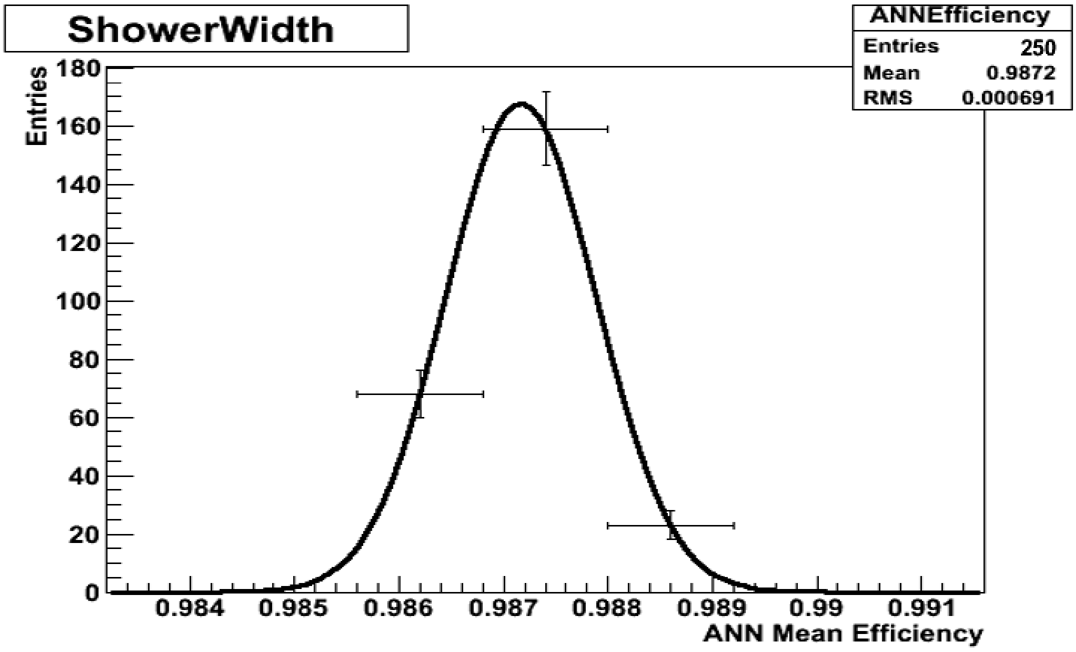

Figure 5.12: The neural net efficiency, for the input variable ShowerWidth, for 250 toys.

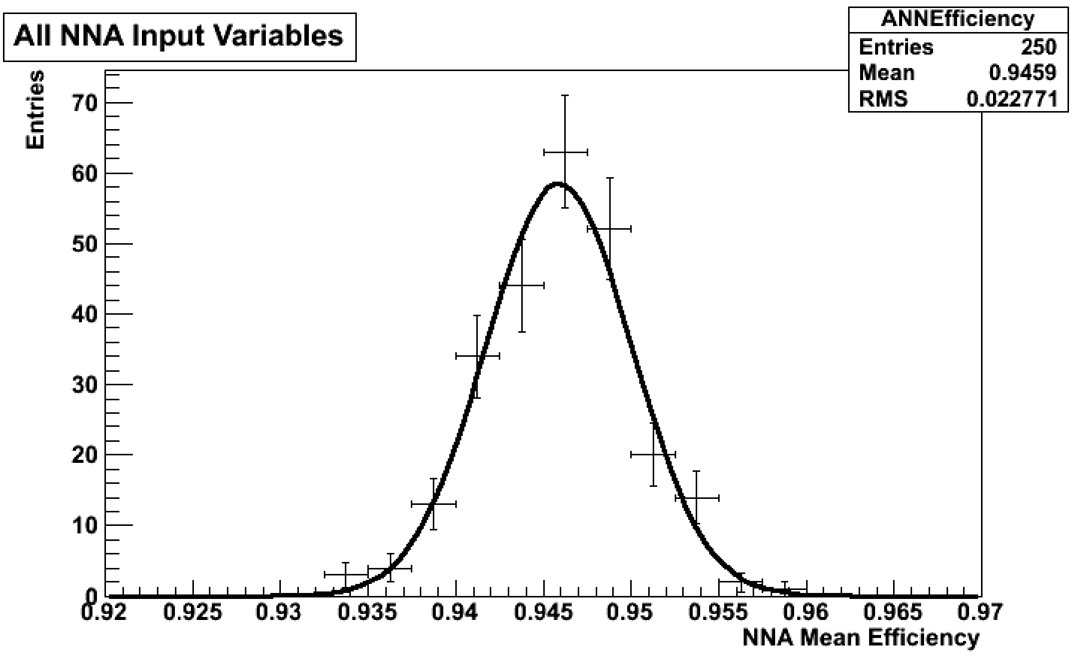

Figure 5.13: The neural net efficiency, for all the input variables, for 250 toys.

5.3 Michel Electrons Systematics

Muons decay in to an electron and 2 neutrinos. The electron produces an EM shower inside the detector and it is easy to identify. Thus if we backtrack the electron, we can identify the event that produced the electron and find muons that passed our selection criteria. It is one more method to improve the purity of our selection. This is called Michel Electron tagging and I include it in my analysis, as one more method to remove muons from the signal. In order though to include it in the analysis, I had to test the performance of the code and calculate the systematic errors. A high purity Monte Carlo, independent muon sample is created (fig 5.14) to test the efficiency of the Michel electron tagging. Then, using the same criteria with the MC, I created an independent muon sample from my data. The difference of the efficiencies between MC and data, will give an estimate of how many muons we don't identify in our data. For the MC the efficiency is 63%, while for the data is 62%, that means in our final selection, we expect more muons in our data, than in our MC. When I apply this error to my MC proton selection I get 1% fractional error. This number will be added to the overall error. We generated the muon sample using the following cuts,

- $\mu\ Pull| <= 2$
- $|p\ Pull| > 2$
- $|\pi\ Pull| > 2$
- $|e\ Pull| > 2$
- $charge\ q = -1$

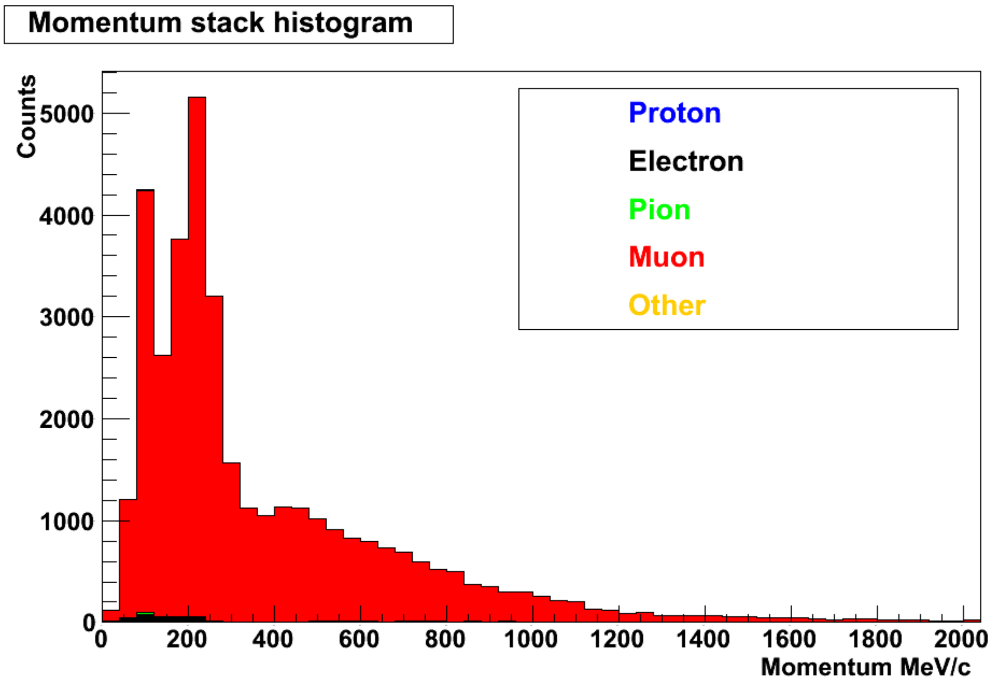

Figure 5.14: Muon sample used to calculate Michel Electron Systematics.

5.4 Proton Pull Systematics

Next I had to calculate the error systematics of the proton pull. I used the proton control sample, I created for the other systematics, as it is independent of the proton pull, and it has high proton purity. Then I compared the proton pull of my data and the MC. The two distributions had different mean values and standard error. In order to see the effect of the different proton pull distribution to my analysis I changed my MC proton pull so to match the data (fig 5.15) and I used the new distribution for my signal selection. The new modified proton pull distribution had a 2.5% loss of protons. This is an error can not be corrected, and is included in my total systematics.

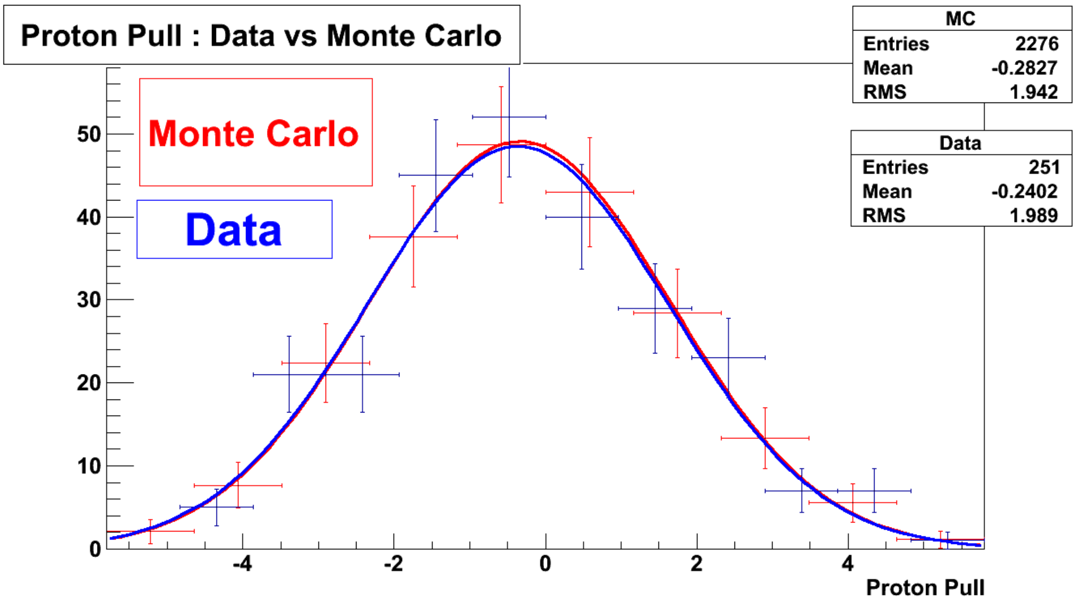

Figure 5.15: Proton pull corrected MC vs Data normalised with fits.

5.5 Flux and Detector Systematics

Flux Systematics : Flux model errors are all handled by altering a set of parameters (or dials), and using the covariance matrix provided by the T2K's NIWG group [54], the correlations between parameters are taken into account. Gaussian throws are performed using this covariance matrix across the three groups, flux, and the neutrino interaction model via the Cholesky decomposition method: for each group, the parameters within that group are simultaneously varied while the other parameters do not change value. To generate event-by-event weights for each value of each altered parameter, a reweighting procedure is then run across all the events. In the collaboration the ND280 Beam Group calculates the flux uncertainties, then creates the covariance matrix to compute the systematic errors and provides the flux corrections. The ND280 Beam Group evaluates the flux uncertainties and provides the flux corrections, and the covariance matrix to propagate the uncertainties. The flux systematics is separated in bins of true neutrino energy for the three neutrino flavours. Uncertainties on different parts of the ND280 MC simulation affects the flux prediction. The fig (5.16) shows the ND280 flux uncertainty as a function of the neutrino energy, at low energies, the hadron production uncertainties dominate [55].

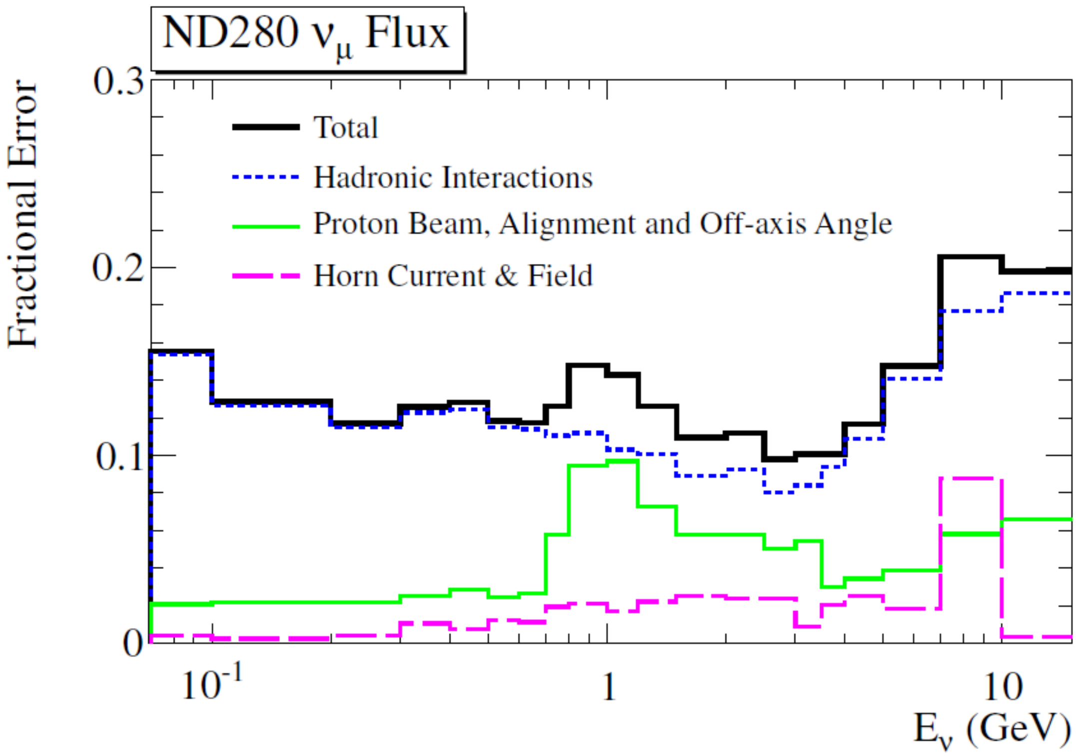

Figure 5.16: Fractional flux uncertainty on the ND280 [56].

Detector Systematics : There are a large number of sources of systematic uncertainties, due to the modular design of the ND280 detector. The design allows the systematics to be calculated in the same way for both FGD1 and FGD2 selections. The uncertainty on a given observable is quantified by evaluating the data to MC differences in an independent control sample. Some parameters affect directly the event selection and they make the MC uncertainties. the number of events passing the selection cuts, have the systematic uncertainties. The variation systematics concerns all the reconstructed quantities with uncertainties. To compute these systematics, we change values of a parameter each time and we rerun the selection. For the weight systematics we reweight the events, so we measure the contribution of each event to the selection. Follows, brief descriptions of the most important detector systematics for this analysis.

- Magnetic field distortions : The particles crossing the detector are affected by the unavoidable anomalous curvatures, near the edges, of the magnetic field lines. The distortions were measured with a Hall probe before the installation and the reconstruction accounts for these measured deviations from the ideal field. By turning on and off the magnetic field, we can evaluate the systematic uncertainty by comparing the reconstructed momentum [53].

- TPC momentum resolution : For events which cross muplitple TPCs, If we compare the reconstructed momentum in each TPC, and after correcting for the energy loss in the FGDs, their difference should follow a normal distribution with center around 0. The standard deviation of the distribution is the momentum resolution [53].

- TPC momentum scale : It depends on the overall magnetic field strength, as there is a calibration mapping between the momentum and the curvature of the tracks. Uncertainties in the magnetic field strength is confirmed using a control sample of cosmic muons passing through both FGDs, which lead to an uncertainty on the momentum scale of 0.6% [53].

- TPC PID : The uncertainties mainly come from the difficulty of particle separation. Is measuring the dE/dx, which depends on a particle hypothesis. Muons can be misidentified which changes the signal and the background. With high purity control samples of electrons, muons, and protons we can compare the energy deposit difference between MC and data and evaluate the systematics. Pull distributions are calculated for both data and MC and the differences are taken to correct the MC. For each particle type and TPC, the uncertainty is measured as a function of momentum, pull's mean and pull's sigma [53].

- TPC cluster efficiency : describes the efficiency of reconstructing a cluster, and it is found to be better than 99%. It is calculated as a function of the vertical clustering and the horizontal, and we assume to be correlated, as they have the same underlying uncertainty (hit efficiency) [53].

- TPC tracking efficiency : A control sample of muons, is used to measure the difference between data and MC and estimate the tracking efficiency. In all three TPCS, the efficiency is found to be better than 99% for both data and MC. The inefficiency due to the overlap from a second nearly collinear track was calculated and is negligible [53].

- TPC charge ID efficiency : From the curvature of a track in a magnetic field, the charge is determined, so we can calculate how often the assigned charge is wrong by the TPC. For momenta less than 5GeV, uncertainty is less than $< 1\%$. For higher momentum the tracks become more straight, as they follow the arc of a bigger circle, so the efficiency decreases as the uncertainty increases. For low momentum, we have less statistics as fewer particles cross all the TPCs and a mismatch is more likely to happen [53].

- TPC-FGD matching efficiency : Using a control sample of comsic or sand muons, which cross at least a TPC and a FGD, we calculate the systematics. The matching efficiency is almost 100%, as the difference between MC and data is almost zero. In case of an event near the edge of the FGD, the efficiency drops, and there is a systematic error [53].

- Pion secondary interaction : A pion leaving the nucleus can undergo secondary interactions, either with absorption, charge exchange, or quasi elastic scattering. The predictions have been found to be significantly different from the available external data, even though these interactions are modeled in MC [53][57].

- FGD Mass : The systematics is evaluated from the uncertainty on the density of the scintillator and water modules [58]. The FGD1 consists overall of 15 scintillator modules, while the FGD2 is overall composed of 7 scintillator modules interleaved with 6 water modules. During the assembly of the detector, each component has been carefully measured, and calculated the uncertainties. The density of a scintillator module has 0.6% uncertainty, while the water modules have 0.55% [53].

- Fiducial volume systematics Simulates an interaction outside the fiducial volume, and inside the ND280 detector [59].

- P0D Systematic : The P0D is designed for π^0 reconstruction while the Tracker is intended to analyse charged-particle final states. When combine the electromagnetic calorimeter and the charged particle tracking system, we can cross check the results of the P0D and calcuate the systematic errors [60].

- Sand Muons : Simulates an interaction outside the fiducial volume which enters in to the detector [59].

- Pile-Up : Due to a possible pile-up which prevents, a true ν_μ Charged Current event, from being collected [59].

As discussed, the detector uncertainties are the largest one, they have been calculated by the ND280 collaboration. The detector systematics have various scources and are correlated among each others. Nevertheless they can be studied separately, propagating them to the final result as if they were independent sources. We have the following fractional errors:

Detector systematics	Fractional error
Pion secondary interaction	1.47%
FDG mass	0.95%
Momentum resolution	0.52%
TPC track efficiency	0.45%
Magnetic field distortion	0.43%
Out of fiducial volume	0.42%
TPC-FGD matching	0.15%
TPC PID	0.13%
Charge mis-identification	0.07%
Pile-up	0.07%
Momentum scale	0.07%
TPC cluster efficiency	$< 0.001\%$
P0D VETO	0.12%
Sand muons	$< 0.001\%$

5.6 Protons to Neutrons Ratio

With all the errors calculated I had to validate my results. First I scaled the MC using the protons on target (POT) number to see how it compares with the data. For this analysis I use the MC production 1 to 3 with total POT 2.438×10^{20}. Then I applied all the error corrections not coming from the detector and are effecting my selection like the Michel electron tagging, and the proton pull which create a discrepancy between data and MC. Last step was to plot the MC and the data together, to see how well the MC match the Data. A good match gives us confidence to trust the MC results, and make safe predictions about our data. The figure 5.17 shows the MC versus the Data per particle type, and the figure 5.18 shows the interaction type. The MC match the data well enough to allow predictions for the data using solely information of the MC. The MC includes all the selection and the NNA cuts, for both FGDs and for the events with ECAL activity. The MC proton purity is 93% and we can assume safely that the same applies to the data as well.

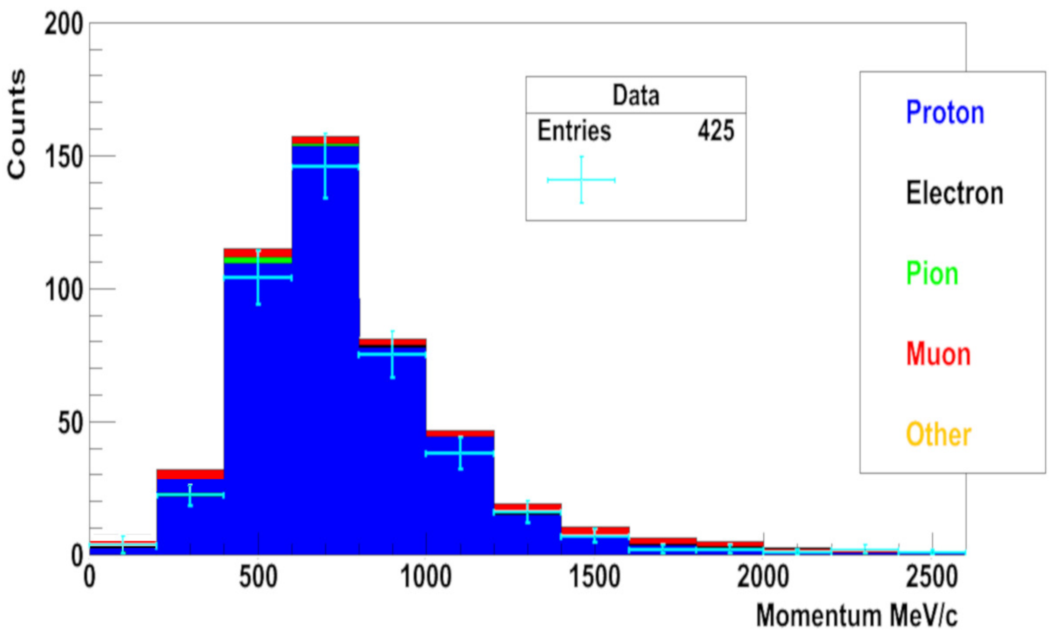

Figure 5.17: MC distribution per particle type (after applying all corrections and scaling to data), vs Data.

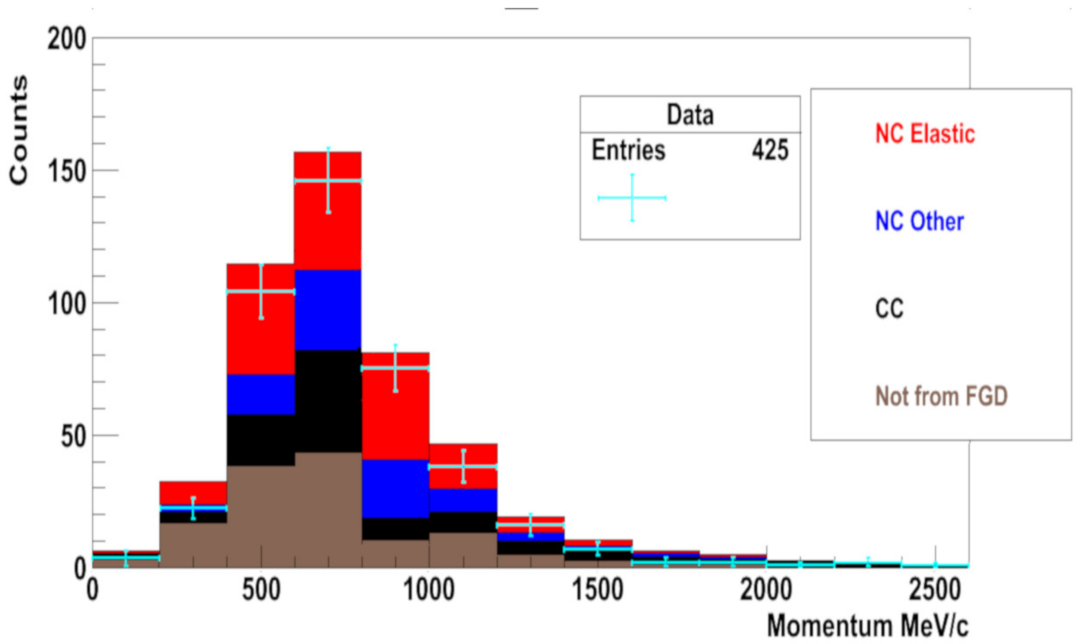

Figure 5.18: MC distribution per interaction type (after applying all corrections and scaling to data), vs Data.

My measurement is the proton to neutron ratio in the MC selection. This measurement is very interesting as it will allow to compare the results of the T2K with other experiments who have measured this ratio. Also it is another useful result to understand better the MC interactions, and also will help for any future cross section measurements for the protons and neutrons. Also we can probe the nucleus and test the interaction models we use for the MC, and remove simplifying assumptions we make. It is an original measurement in the ND280 collaboration. Lastly this measurement can allow us compare the ratio between the Super-K and the ND280 and search for discrepancies.

When a neutrino interacts with a nucleus it can release a proton (NCQES event), a neutron or other particles. If a neutron is released, will not appear in the detector, though due to the big mass will interact inside the detector and will have a secondary interaction. A percentage of the protons in my signal come from this kind of interactions, especially for events outside the FGD. In reality the detector can not tell if a proton was released by a neutrino or a neutron as both of them are invisible to the detector. The MC simulates those events using the predictions of the standard model, and real data whenever are available. The protons of the NCQES come solely from neutrino interaction with the nucleus, while the other NC events, about 35% of them, a neutron interaction with the nucleus and release a proton. The protons of the CC events, only 2%, come from neutrons, and for events that started outside the FGD, about 92% of the protons come from neutrons. Therefore we expect the total

Table 5.1: Interaction type of selected protons, and percentage of the protons coming from secondary neutron interaction with a nucleus.

Interaction type	%	Events coming from neutrons %
NCQES	38.9	-
NC Other	15.5%	35%
CC	13.6%	2%
Not from the FGD	32%	92%

number of protons coming from neutrons to be about 143 or 34%. The total error of our measurement is the square root of the sum of the errors squared. The detector systematic is the total of the table 5.5. The neutrino Flux error for this analysis is 0.43%, and the NNA is the neural network error. The FSI is the final state interactions and is a correction for the nuclear effects. Therefore the final number is 143 ± 4.29 or $34\% \pm 3.01\%$.

Table 5.2: Summary of all systematic errors for this selection.

Systematics	Fractional Error %
Detector total	1.99%
Neutrino flux	0.43%
FSI	0.21%
NNA	2.3%
Total	3.01%

Chapter 6

Liquid Argon Detector Technology and Future Neutrino Detector Designs

6.1 Why Liquid Argon

The future of the next generation neutrino experiments, is heading towards colossal water based detectors with hyper K [61] in Japan, and with liquid Argon detectors based in US around the DUNE experiment [62]. Figure 6.1 shows the DUNE project. A neutrino beam will be generated at Fermilab and 800 miles aways giant liquid detectors will be placed underground at the Sanford Underground Research facility.

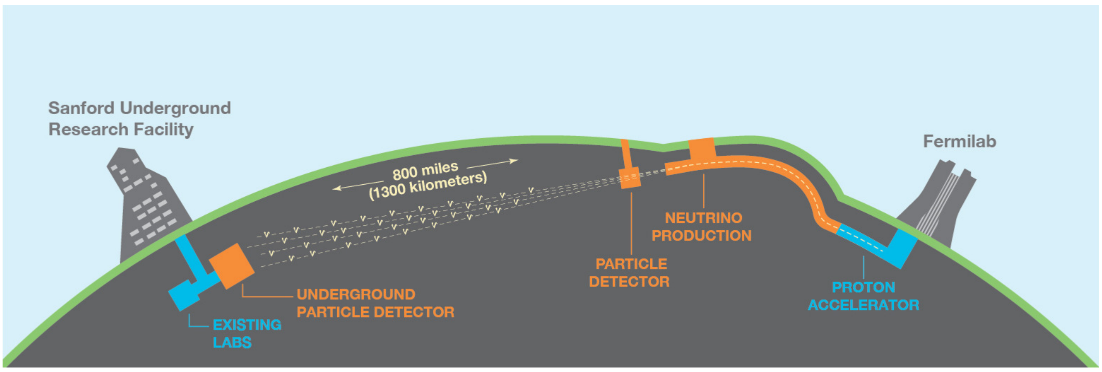

Figure 6.1: The DUNE experiment.

To study neutrino interactions, we need massive underground detectors, that present a large target for neutrinos. The neutrino interactions are very rare due to the nature of the neutrinos, therefore the probability to have an interaction within the detector increases with the size and the mass of the detector. The detectors for neutrinos should be placed underground, to minimise background noise, as the matter around the detector presents a natural shield and can minimise cosmic radiation [63]. A future experiment will need multiple detectors, and an accelerator which will produce neutrinos. The distance between the target and the detectors should be such that maximises the sensitivity to neutrino oscillations [62].

The DUNE collaboration proposes an ambitious program, and is planning to build the biggest underground liquid Argon detector for neutrino physics in an underground mind in South Dakota [62]. The DUNE project will have a near and a far detector. The near detector will be at FermiLab and at the time of this writing the design of the detector has not been decided. The far detector will be 4 modules with 10 kt each. The current plan is the first two cryostats to be instrumental with single phase TPCs and the other two with a two phase type TPCs (subject to successful scale ability using the design at CERN). The beam will come from the FermiLab accelerator, where neutrinos will be generated. Such detectors will allow precise measurements for CP violation in the lepton sector, and to answer the neutrino mass hierarchy problem. The proposed detectors will also be used to study other rare interactions like the nucleon beta decay, and neutrinos from supernovae [64].

Among many materials and elements, we could use in such a detector, the Argon is the best candidate for many reasons. This is due to its intrinsic properties as well as the low cost enabling us to build a detector with magnitude of many kilo tons. The liquid Argon TPC technology provides supreme capabilities for energy resolution, and is an ideal calorimeter. In addition the fine granulation will allow position resolution and reconstruction, even for complex interaction topologies, without limiting our energy range. The DUNE experiment will have interactions with energies above $1 GeV$ and all the interactions will have complex topologies, and the current water Cherenkov detectors are not precise enough to make such measurements. Compared to other designs, the liquid Argon provides a relatively compact solution, which can be scaled up without having impossible problems to solve. Also, Argon is a lot cheaper compared to other noble elements with similar characteristics [65].

There are two proposed designs, the single phase and the double phase detector. In the single phase, all the detector is filled with liquid Argon, while in the double phase, a part of the detector will contain Argon gas, while the rest will have liquid Argon [62]. The detection principle for both design is similar. A particle entering the detector fiducial volume, interacts with the liquid Argon atoms along its path and electrons are released due to excitation of the atoms. The electrons then are drifted, by creating a homogeneous electric field in the detector, towards the readout. Also from the atom excitation, photons are released and we see them as scintillation light, using typical photomultiplier tubes. This light is used to time the event, since the delay is approximately zero due to the light speed being very high in relation to the size of the detector. The event starts the moment we see the scintillation light, and then we can track the event [66]. The latest published results provide the method for a charge read out, using TPCs in a double phase detector[67]. There is a potential to include optical read out, using high resolution cameras that can perform in cryogenic environment, for position and momentum high resolution reconstruction [68]. This is one of the main focus that will be discussed in this chapter.

The single phase design detector will be modular, consisting of “blocks” filled with liquid Argon. All the electronics will be in merged in the liquid Argon and thus we get a very good signal to noise ratio, since the low temperature will minimise the noise. In this design multiple layers of sense wires will be used, on the anode, for event reconstruction and then the signal will be amplified [63]. An electric field cage drifts the electrons released, when the particle enters the detector and excites the Argon atoms on its path, to the anode where is the readout. A photo multiplier tube (PMT) will see the event from the scintillation light, so we can time the event. Then, the slow ionisation drift velocity allows to accurately reconstruct the event in three dimensions. This single phase detector design is scalable and has been proven to work up to 600 tons with the ICARUS program [69].

The double phase design will be one large electron drift volume, where a part of the detector and all the electronics will be in Argon gas. This will make one big TPC, and the design will possibly use THick Gas Electron Multiplier (THGEM, [70]). When the particle enters in the detector fiducial volume, ionises the Argon atoms and electrons are released. A field cage will drift the released electrons to the anode, where a THGEM will multiply them using electrical potential difference, and will create an avalance of electrons to the readout. So this way the signal is amplified. Thus with the THGEM charge readout segmented in to strips, and the scintillation light, using a PMT, the event can be reconstructed in three dimensions. This design is also scalable however up to today on 1 ton detector has been operated. When using a double phase detector we can track events with high energy (1GeV), as well as, with very low energy, about 100keV [63]. In addition to electron multiplication in the THGEM holes, secondary, scintillation light is produced, and this light can be captured by a sensitive optical device. This is highly explored in the Liverpool liquid Argon facility which is dedicated to addressing challenges towards colossal liquid Argon detectors.

Specifically the lab focuses on purification, and recirculation studies. In addition, focuses on the optimisation of light collection, by using wavelength shifting reflectors, and on testing and optimising the charge and optical readout methods. The Liverpool lab is developing a novel detection method using high resolution CCD cameras for the track reconstruction with high precision due to its intrinsic properties of Argon. In the next chapter I will describe extensively the LAr detector in Liverpool and I will talk about my contribution.

6.2 The Liquid Argon Detector in Liverpool

In the Liverpool University liquid Argon lab , there is a 40-litre liquid Argon (LAr) vessel which has a flexible design to allow to perform characterisation studies of new readout devices (fig 6.2). Previous published results were on purification studies [66], and argon pulse shape discrimination studies between nuclear and gamma recoils, by inserting radio active sources inside the vessel. Current efforts are focusing on the construction of a bigger detector and track reconstruction algorithms for events recorded with cameras. This is the Ariadne project [71]. The author worked at the early stages of the detector when the camera readout concept was first being established.

The Liverpool University liquid Argon detector setup, consists of a stainless steel target vessel, a recirculation system to increase purity, two THGEMs manufactured by CERN with optical transparency 35%,a field cage to drift electrons, a high voltage feedthrough which creates the electric potential difference in the field cage, a PMT at the bottom to see light from the interactions, wavelength shifting reflector sheets to amplify the light for the PMT, and lastly but most important innovation high end camera. The detector also had LEDs and cryogenic webcams for internal detector monitoring.

6.2.1 The Target Vessel

The Target Vessel is a 40 litres cylinder made of stainless steel (fig 6.3), with a DN1375 CF, VUV flange at the top from which the detector internal components are suspended. This is custom built, in the workshop of Liverpool University for the LAr lab. When the flange is sealed we use an scroll pump for a day to create vacuum $10^{-7} atm$ and then we shift to the molecular pump which is fixed on the top of the vessel. This way we can create the initial conditions for a high purity liquid Argon inside the detector. On the top of the vessel are attached also various instruments for monitoring and recording. There is a safety pressure seal, which breaks if high pressure is built inside the detector, to avoid overpressure.

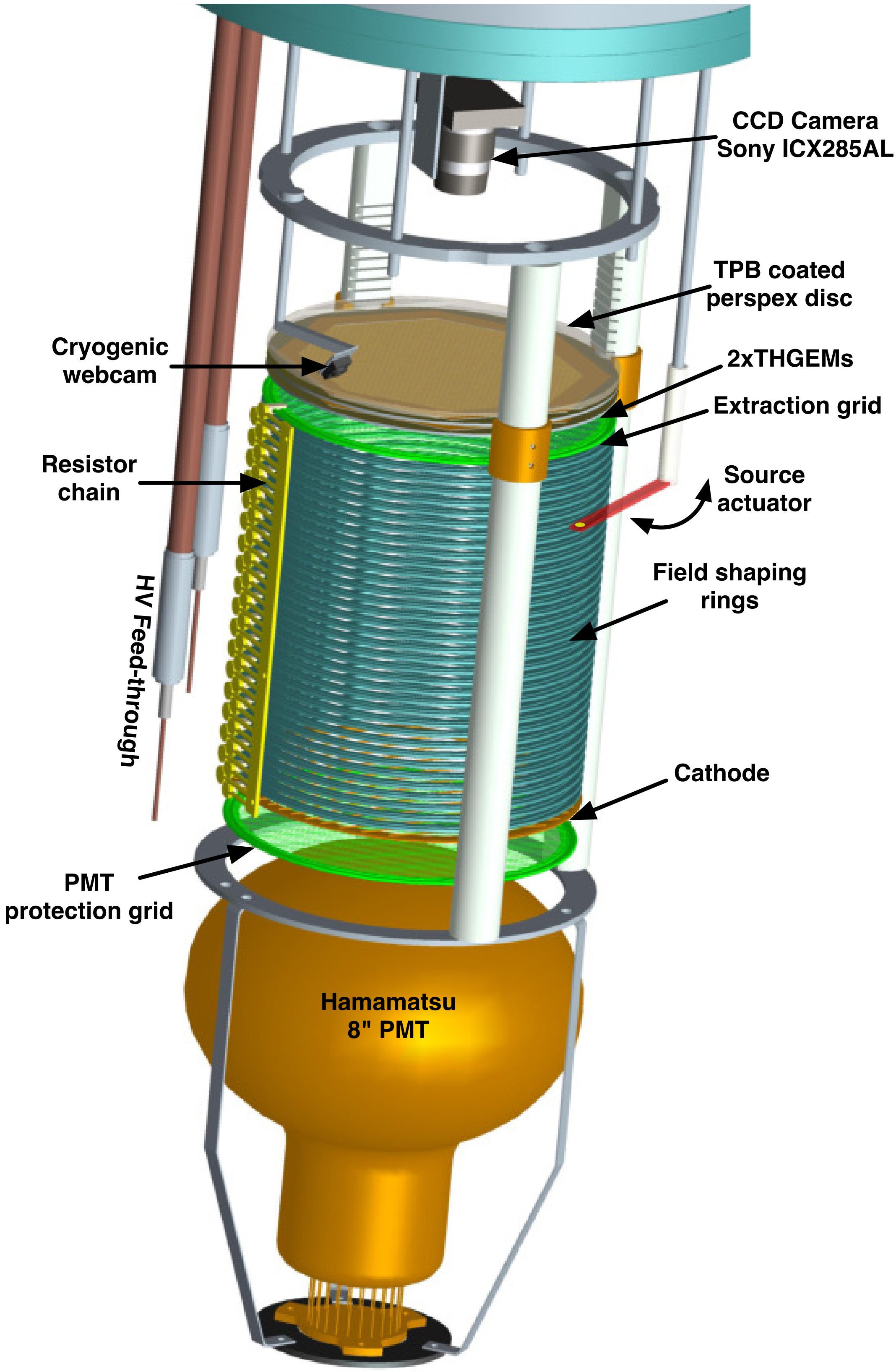

Figure 6.2: The Liverpool Liquid Argon detector, getting ready to go inside the stainless steal cylinder.

The vessel sits inside a 250 l stainless steel open bath to maintain the cryogenic $-185°C$ LAr temperature. Also there is a pressure gauge to monitor the process while we create vacuum, and when we create liquid Argon inside the detector. All the instruments we use are inserted through DN vacuum fittings to provide positive or negative pressure seal.

While building vacuum inside the vessel, we monitor the pressure for leaks and if there is one, all bolts are checked and start the process again. In high vacuum and with all the components install, we fill the bath, with liquid Argon, after we have cooled it down originally using liquid Nitrogen, which is a lot cheaper and more accessible than liquid Argon. Once the bath is full, we insert gas argon, slowly, in the inner detector, and through condensation, the gas converts in to liquid. This way we minimise the stress we put on the instruments, as sudden temperature change can damage them beyond repair. While the detector is operational, we always monitor the liquid Argon level in the bath, so it does not drop, and thus prevents to build pressure inside the detector through conversion from liquid to gas Argon.

To monitor the detector at any time, we are using live cameras connected to the internet with username and password, accessible from any computer and with an alert to notify us of any problems. When the detector is operational there is always someone inside the lab 24 hours ready to intervene in case of a problem or emergency.

6.2.2 The Recirculation and Purification System

The recirculation and purification unit [66] is custom built and designed specifically for the LAr detector. Positioned on the side of the target vessel, and consists of a bellows pump and a purification cartridge. The pump creates a one way recirculation system and the liquid Argon passes through the purification cartridge. Inside the cartridge there is highly fined Copper powder to capture Oxygen atoms, and molecular seaves to adsorb water. The results are published and the recirculation unit can re-circulate 27lt/hour. It was designed and constructed in 2010 and was used also for Argon pu-

Figure 6.3: The target vessel.

rification studies, and the effects of impurities in our detector [66]. After each time we operate the detector, we regenerate the purification cartridge in a vacuum at 600K for about 4 hours. So we make sure any molecules trapped inside are released and the cartridge is ready for use again. The purification system is a vital component of the detector in order to remove electronegative impurities such as oxygen. These impurities will capture the ionised electrons, thus, not allow them to reach the surface of the detector.

6.2.3 The Field Cage

The field cage, is a set of custom made field shaping rings (fig 6.4), placed vertically one on top of the other with 4mm separation between two rings, and they are supported by 3 non conducting custom rods made out of Macor. Macor is a ceramic type material with very low out-gassing properties. The rings are electrically connected with custom made potential dividers (resistor chain), specifically designed to divide the voltage equally among the rings, in order to create a homogeneous electric field, with the electric potential to increase with each ring. The rings have 178mm diameter and they are 38 in total, creating a 20cm drift field. By applying 30kV between the anode and the cathode (the top and bottom grid), the rings with the resistor chain, create a uniform electric field of 1kV/cm is created.

The field cage defines the fiducial volume of the detector. When an incoming particle interacts with the argon atom, ionization and scintillation result. The primary scintillation light (S1) will be detected immediately by the PMT. The free ionized electrons released inside the detector will be drifted to the surface of the liquid (i.e. the top grid). Once the electrons are at the surface of the liquid, they will be extracted to the gas phase via the application of a higher electric field of about 4 kV/cm, thus creating secondary electro luminescence light (S2). The time difference between S1 and S2 will provide the electron drift time. A charge amplification/readout device such as a THGEM is positioned in the gas phase of the detector.

Figure 6.4: The field cage of the detector is consisted of rings which create a homogeneous drift electric field in the volume inside the rings.

6.2.4 The LAr Insulated High Voltage Feedthrough

Originally two custom made ceramic Si (silicon) Oil filled feedthroughs for high voltage cables were tested and installed in the detector. The two cables were connected to the rings in order to create a potential difference, and a uniform electric field in the fiducial volume of the detector. One feedthrough was connected to a 10kVolts power supply and the other to a 30kVolts. The rod is made of steel and inside runs the high voltage cable, with ceramic ending for good insulation. In addition, inside the feedthrough, we pumped out the air and we filled it with silicone oil. This feedthrough design has worked in room temperature however in cryogenic Si freezes and discharges (fig 6.5).

A new novel design of high voltage feedthrough was made instead, using liquid Argon as an insulator. The feedthrough consists of a stainless steel tube, a ceramic vacuum feedthrough and a PTFE sleeve. At the end of the tube the ceramic feedthrough is welded and inside the tube a high voltage cable is soldered to the copper pin of the ceramic feedthrough. Around the soldier connection the PTFE sleeve is inserted to provide extra insulation. This pipe/feedthrough assembly is immersed in liquid Argon and as such if you insert gas Argon in the tube it will condense in to liquid therefore will provide an excellent insulation. A photograph of the feedthrough can be seen at the figure (reference). This new design was successfully tested up to 30kV.

6.2.5 The THGEMs

Two THGEMs [72] (fig 6.6) manufactured by the CERN TS/DEM workshop were used [72]. The amplification region of the THGEMs has an octagonal shape with a 150 cm^2 surface area. Within this region there are approximately 23000 holes that have been mechanically drilled with standard PCB techniques in a copper cladded glass epoxy plate. The copper extends 1 cm from the perimeter of the amplification region for optimal shaping of the electric field at the edges of the active volume. Each

Figure 6.5: A close up picture of the feedthroughs.

THGEM is 1 mm thick and and each hole has a diameter and pitch of 500 μm and 800 μm respectively. A 50 μm dielectric rim is also etched around each hole to extend the break- down voltage of the THGEM. A photograph of the THGEM is shown in Figure 6.6 . The optical transparency of the THGEM is 35%. When mounted in the detector the space between the two THGEMs is 4 mm and care was taken to align the holes of the top and bottom THGEM.

A 30 kBq Am-241 alpha source was used to calibrate the detector in gas and liquid operation. Alpha tracks deposit all their electrons within 4 cm in pure argon gas and therefore Am-241 is an ideal source for gas measurements and optical imaging with the CCD camera. Additionally, the energy deposition of alphas in gas compares to a muon deposition energy in LAr which is $\approx$2.3 MeV/cm [72]. The source was mounted facing upwards 3 cm below the extraction grid using a rotation motion feedthrough that allows the source to enter and exit the field cage through the gap between two FSRs (Field Shaping Ring). As alphas do not penetrate the field cage from outside, we can effectively switch on and off the source ionisation signal. For the two phase run an external Cs-137 high rate gamma source was also used.

The gain of the THGEMs is defined as the ratio of the charge produced after amplification over the initial charge produced before amplification. No corrections are incorporated for electron losses due to grid transparency and electron recombination. In LAr the 5.4 MeV alphas are expected to produce on average 228800 primary electron pairs whereas in GAr 204500 electron pairs will be produced assuming a W-value of 23.6 eV and 26.4 eV respectively [72]. The Am-241 source also produces gammas which are predominantly at 59.5 keV and these are expected to give rise to approximately 2500 electron pairs in LAr. The gain of the THGEMs was measured using an ORTEC 142IH preamplifier connected to the top THGEM electrode. This preamplifier is calibrated by the manufacturer to produce 0.05 μV per electron pair. For each pre amplifier amplitude measurement the average of 1000 pulses was calculated using the mathematical function on a Lecroy 9374TM oscilloscope.

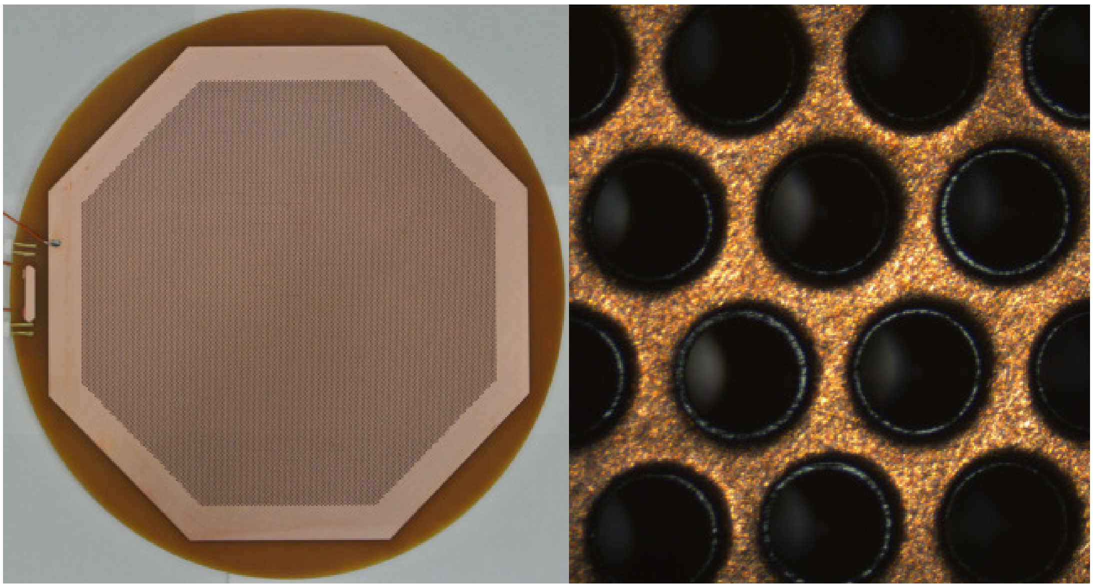

Figure 6.6: The THGEM.

6.2.6 The Monitoring Cryogenic web-camera

Cryogenic environment can seize the operations of electronics. Certified Commercial cameras that can work in cryogenics are very hard to be found. However, silicon detectors commonly are cool down to low temperature in order to reduce the noise. We were the first lab to conceptualize, to investigate and use webcams in liquid argon. To this end a variety of webcams were purchased and cool downed with liquid nitrogen in order to identify the ones that will continue functioning in this environment. We were the first lab that could see inside a liquid Argon detector [72]. The main problem was to identify a camera that works inside liquid Argon, to this end we have tested 15 cameras by submerging them inside liquid Nitrogen. We used liquid Nitrogen because it is very cheap and only 10 degrees Celsius below liquid Argon. The Microsoft HD 3000 has shown an excellent performance in cryogenic environment. Details of the tests that were performed to identify these cameras are described in section 6.3.

6.2.7 Scientific CCD Camera

The CCD was an Artemis FS14 using a Sony cheap ICX285AL [72]. The chip is very popular among astronomers and its relative low cost along with high sensitivity made it the best choice. Additionally, the camera as a whole system (including the digitiser card) will not operate at such low temperatures without the development of cold electronics. We circumvent this issue by mounting the majority of the electronics (i.e. the digitiser) externally, connected to the CCD sensor via a custom made Kapton cable and feedthrough.

The chip's response to low temperature was tested before assembly in the detector using a separate apparatus. A thermocouple was attached to the back of the chip which was then was cooled down at a rate of about 3 C/min. The chip thermal noise reduced significantly during the cool-down, however, the chip stopped functioning below $-120\ ^oC$. The CCD gain and the Read Out Noise (RON) for 28 ^oC and $-100\ ^oC$ were measured and are shown in Table [72]. To allow chip operation in a colder environment a resistor type heater was made and placed on the back of the chip. This allowed very nice heat exchange control of the chip which, as a result, operated down to $-190\ ^oC$. In two-phase operation the chip was typically kept at $-60\ ^oC$.

As the secondary scintillation light produced in the THGEM holes is mainly in the VUV region, special care has to be taken with the optics used. VUV grade lenses are very expensive and additionally VUV is out of the spectrum range of the CCD. An obvious way around this issue is to coat a normal camera lens with wavelength shifter (WLS), however, this was inadequate for this setup. As an alternative we coated a transparent disk with WLS and placed this directly above the THGEM, thus VUV light is converted to visible before it reaches the camera lens. Specifically, a 178 mm diameter perspex disk coated with 0.05 mg/cm^2 TPB was positioned 4 mm above the top THGEM. As VUV light doesn't penetrate perspex, the coated side of the disk was placed facing downwards. The lens used in the setup is a Fujinon DF6HA-1B which has a small focal ratio of f/1.2 allowing more light to reach the chip. In order to mount this lens onto the chip, a CCD chip holder with a C-mount thread was manufactured.

Just below the camera, and above the extraction ring we installed 8 LEDs, four white and four red. In the detector there are four metal supporting rods in a cross, and we installed on each rod one white and one red LED. I tested many types of LEDs in liquid Nitrogen, and I excluded the LEDs that didn't emit sufficient light or failed. I tested the LEDs starting at room temperature, to $-190\ ^{\circ}\mathrm{C}$ and I tried different voltage and current to find their limit. We decided to install two sets of four, connected in parallel, each set is different type and colour, in case one fails we will have less chances the second to fail too. The white LEDs needs more voltage than red for the same luminosity, though on the other hand white is what our eye can see best and therefore the web cameras. When the PMT is off, the LEDs can be on, so we can see inside our detector with the web cameras. This is a great help when we want to see the level of the liquid Argon, or in case something goes wrong inside the detector, we might have the chance to pinpoint the problem.

6.2.8 PMT (Photo Multiplier Tube)

The photomultiplier tube (fig 6.7) in our detector is recording the Argon scintillation light We use an 8-inch Hamamatsu R5912-O2MOD PMT [66] optimised to work in cryogenic environment. The PMT is placed at the bottom of the detector, right after the last ring of field cage positioned watching upwards towards the field cage (fig 6.4). Those PMTs are commonly used for neutrino physics applications and are used in various experiments. The PMT multiplies the incident photon using a 14 stage dynode stack and has a high gain design. This PMT requires 900V, potential difference between the anode and the cathode, to operate. According to the manufacturer the rated gain is 10^6, though at very low temperatures the gain drops. Compared to other PMTs, the Hamamatsu, has better detection efficiency in a cryogenic environment, eventhough it's gain drops.

If a minimum ionisation particle (MIP) enters the detector, interacts with the Argon atoms and excites those along it's path. From the de-excitation, photos are released, and approximately 30% of the photons appear as prompt light (fast component), which is the scintillation light the PMT detects. The rest of the photos create a slower component signal in the PMT. The fast component is of the order of nano seconds, while the slow component is of the order of micro seconds The fast component of the PMT signal is used as an event trigger, as it arrives almost instantly the moment of the interaction. The main drawback of this PMT is that it's maximum efficiency is at 420nm while the scintillation light in Argon is 128nm. In order to increase the efficiency of the PMT, we shift the wavelength of the photons, we enclose the field cage with non conducting 3M reflector foils, coated with Tetra phenyl Butadiene (TPB). The TPB has the property to shift the light wavelength from 128 to 420nm. The 3M reflector foil was selected because in non conductive and doesn't release molecules inside the detector, thus doesn't effect the LAr purity. The TPB was coated on the reflector using the vacuum evaporation method as it is better applied than the simple spray method.

Figure 6.7: The PMT design, and sits at the bottom of the detector looking upwards.

6.3 Identifying Cryogenic Web Cams and Installation in the Detector

Cryogenic environment can destroy electronics and requires specialised equipments, cameras that have certificate to operate in very low temperatures are very expensive and for that our work can be revolutionary. We are probably the first lab that can see inside a liquid Argon detector, with a low budget commercial web camera. Nothing similar has been published before, and the camera has many advantages. The main problem was to find a camera that can work inside liquid Argon, we tested many cameras (about 15) by submerging them inside liquid Nitrogen. We used liquid Nitrogen because it is very cheap and only 10 degrees Celsius below liquid Argon (fig 6.8).

In our apparatus we used 3 fibre optics (fig 6.9) and we enclosed the camera in a dark environment. Then we took images in fits extension and we could see the light intensity in every pixel. This way we can make plots of the light intensity as a function of temperature. Also using the PMT and a single fibre optic we calculated the number of photos per second emitted, and then we calculated the sensitivity of the camera. The minimum number of photons per pixel in the web camera is about $10,000$ photons which is the maximum intensity the PMT can read.

We tried web cameras from many companies, and different models from each company. Only one model passed all the tests, the Microsoft HD3000, 2010, with almost no noise. Most of the other cameras had stopped working below -100 °C, and only three models didn't fail. The other two models had many artefacts and noise due to the low temperature and the temperature change of the electronics (table 6.1).

After we chose the model we had to open the web camera, remove the casing and modify the USB cable to fit in the detector. Part of the cable was replaced to keep vacuum and we had to make sure there were no leaks. Then the cameras were mounted on a ring above the grid, and one camera was looking straight to the PMT (fig 6.11),

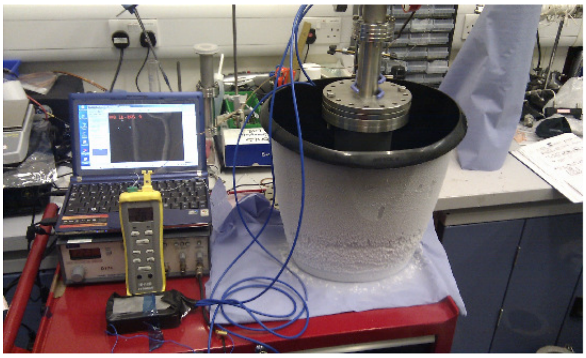

Figure 6.8: Web camera test

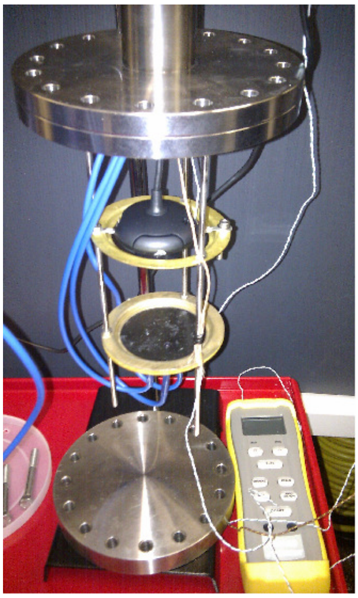

Figure 6.9: Apparatus to test the web cameras light sensitivity at cryogenic temperatures.

Table 6.1: Characteristics of the successful cryogenic web cameras.

Webcam Name	Model Number	Sensor Type	Focus	Comments
Microsoft VX-1000	1080	CMOS	Manual	-
Microsoft VX-3000	1076	CMOS	Manual	-
Microsoft HD-3000	1456	CMOS	Auto	Model no:1492 doesn’t work in cryogenics

while the other at the side of the detector(6.12). We used the second camera to monitor the level of the liquid Argon, and we managed to get it between the grid and the last ring of the cage field (fig 6.10).

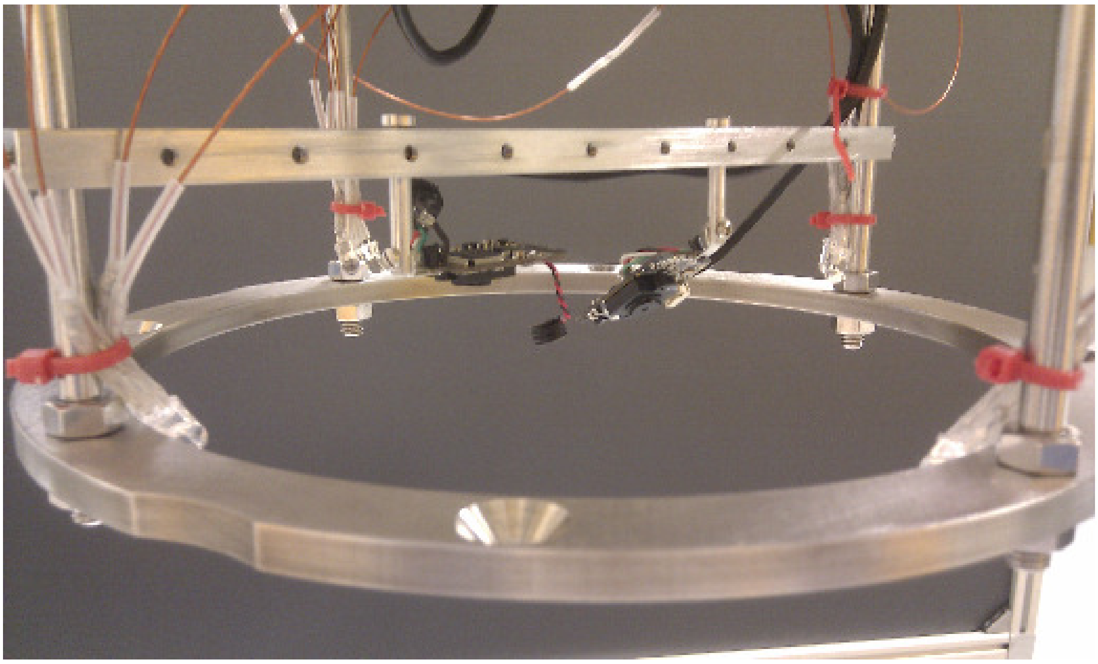

Figure 6.10: Web cameras test setup.

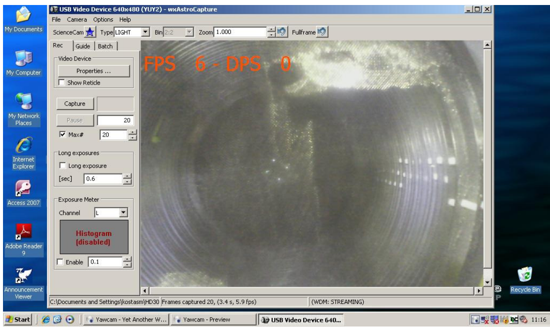

Figure 6.11: WebCam1

Downwards view, of the detector

Figure 6.12: WebCam2

Monitoring the LAr level.

Just below the camera, and above the extraction ring we installed 8 LEDs (fig 6.13), four white and four red. In the detector there are four metal supporting rods in a cross, and we installed on each rod one white and one red LED (fig 6.14). After testing many types of LEDs in liquid Nitrogen, and we excluded the LEDs that didn't emit sufficient light or failed. The LEDs test started at room temperature, to -190 °C and then we tried different voltage and current to find their limit. We decided to install two sets of four, connected in parallel, each set is different type and colour, in case one fails we will have less chances the second to fail too. The white LEDs needs more voltage than red for the same luminosity, though on the other hand white is what our eye can see best and therefore the web cameras. When the PMT is off, the LEDs can be on, so we can see inside our detector with the web cameras. This is a great help when we want to see the level of the liquid Argon, or in case something goes wrong inside the detector, we might have the chance to pinpoint the problem.

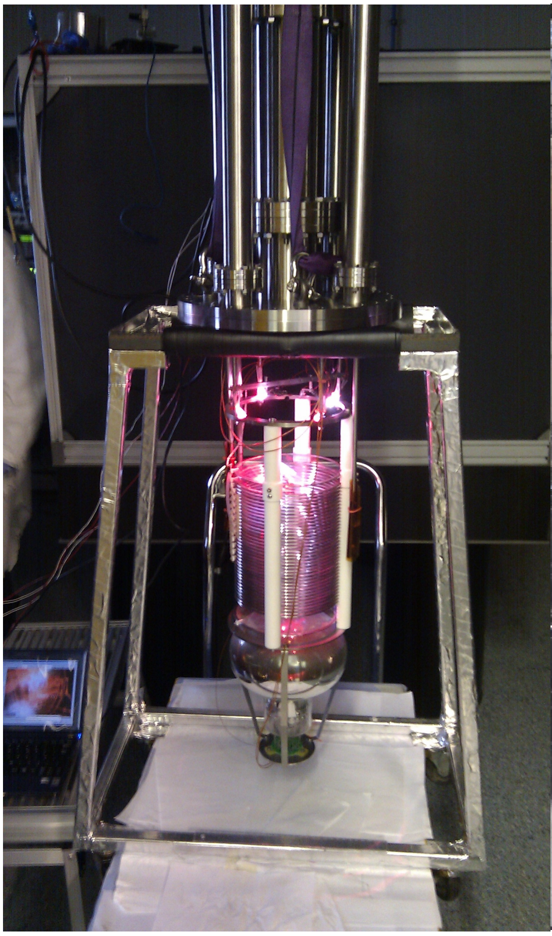

Figure 6.13: LEDs on

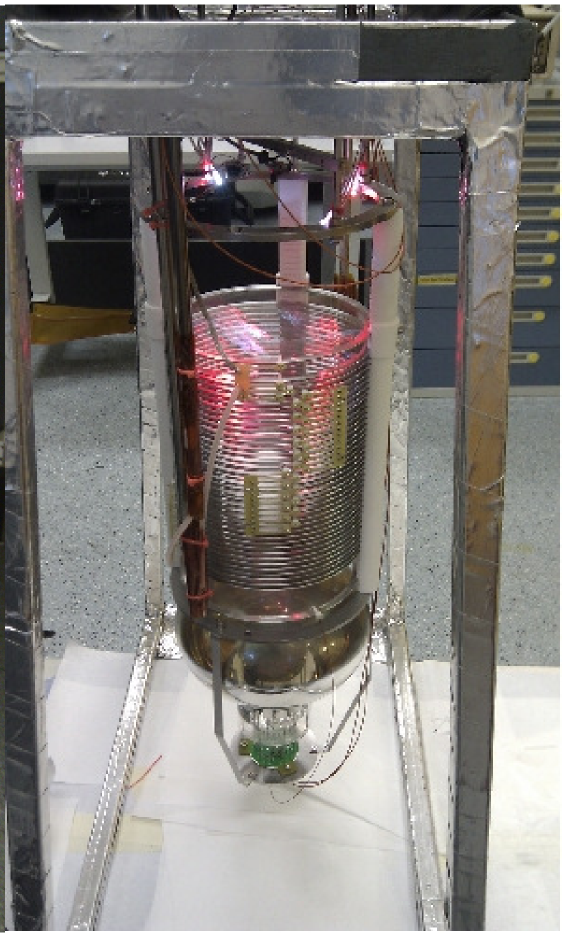

Figure 6.14: LEDs installed

6.4 Gas Argon Operation

Initially and before to run the detector in a liquid Argon environment, it was tested in gas Argon. Calibration runs were done during that phase, which helped to understand the THGEM (fig 6.15) behaviour with respect to different voltages and calculate the THGEM gain (fig 6.16) [72]. Also the PMT and the CCD were monitored and their performances were recorded and analysed. To prepare the detector for the test runs, it was evacuated at 6×10^{-7} millibars and after it was filled with gas Argon, the tests lasted about 3 hours maximum to minimise purity differences due to outgassing of the components purity instabilities.

Initial studies on a pure gas Argon environment, were run to test the electric field inside the detector, and the THGEM [72]. A radioactive alpha source was inserted in to the detector and produced primary and secondary scintillation light (fig 6.17). The electrons created due to the alpha source (fig 6.22) were guided to the THGEM, following the electric field. The THGEM gain was calculated and the break down voltage was determined.

In addition the relation between the PMT light collection (fig 6.18) and the THGEM light was found to be linear. For very high gains of the THGEM (above 25) [72] the PMT was saturated due to the high light production (fig 6.19). For the electric field of the THGEM and the light collected by the PMT, the relationship is exponential. In a 10 second exposure, with binning 8×8 the CCD lowest limit (fig 6.20) for light detection is when the THGEM gain is 1, and for gain above 53 the CCD is saturated (fig 6.21). At this stage after the detector performance was characterised in room temp (fig 6.23) gas cryogenic two phase operation took place.

It is also worth mentioning that it was found that small impurities in GAr, even on the 40 ppm level (based on argon scintillation slow component decay time measurements [66]), coming from detector component outgassing is enough to produce visible light within the spectrum range of the CCD thus wavelength shifter is redundant in this case. However, for higher purity levels the signal is visible only with the use of

WLS.

Table 6.2: Configuration of the electric fields applied in room temperature gas operation.

	Distance to the stage above (cm)	Potential (kV)	Field to the stage above (kV/cm)
$THGEM_2$ (top electrode)	-	+1.50 to +1.85	-
$THGEM_2$ (bottom electrode)	0	0	15.0 to 18.5
$THGEM_1$ (top electrode)	0.4	0	0
$THGEM_1$ (bottom electrode)	0.1	-1.50 to -1.85	15.0 to 18.5
Extraction grid	1.0	-2.0	0.15 to 0.5
Cathode	20	-4.0	0.1

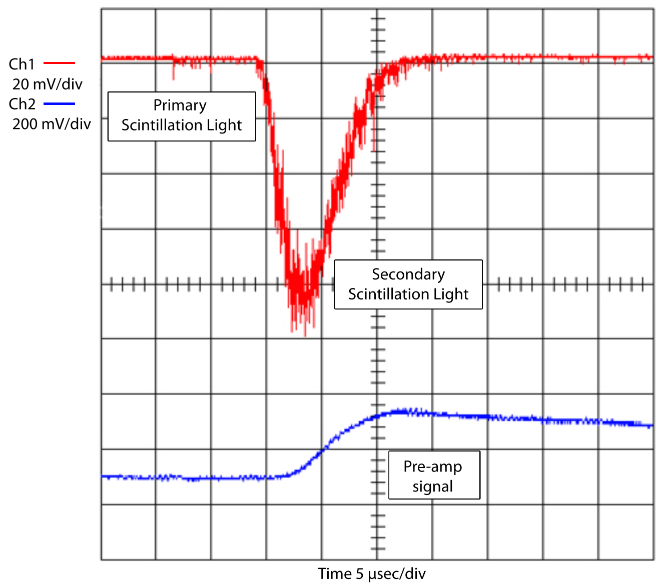

Figure 6.15: A sample event of primary and secondary scintillation light with the corresponding charge signal from the preamplifier in pure 1 ppm argon gas. The THGEM gain was ∼20.

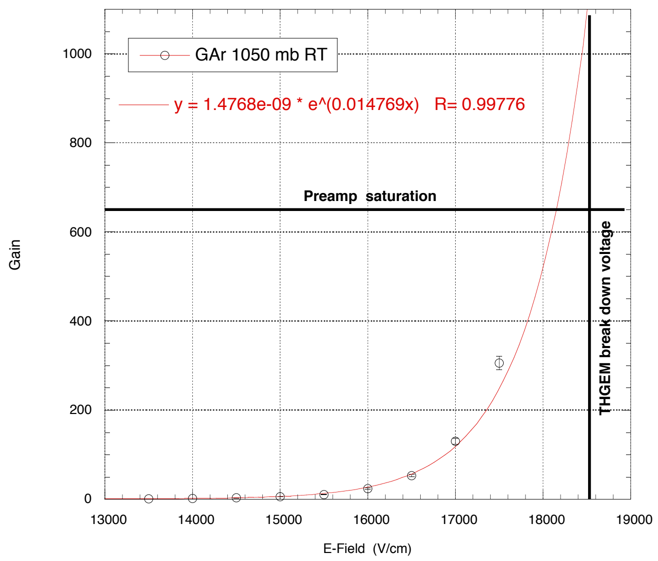

Figure 6.16: Gain variation with THGEMs field. Gain measurements above 18 kV/cm were not possible as the pre-amp signal was saturated. The break down voltage of the THGEMs was approximately 1850 V.

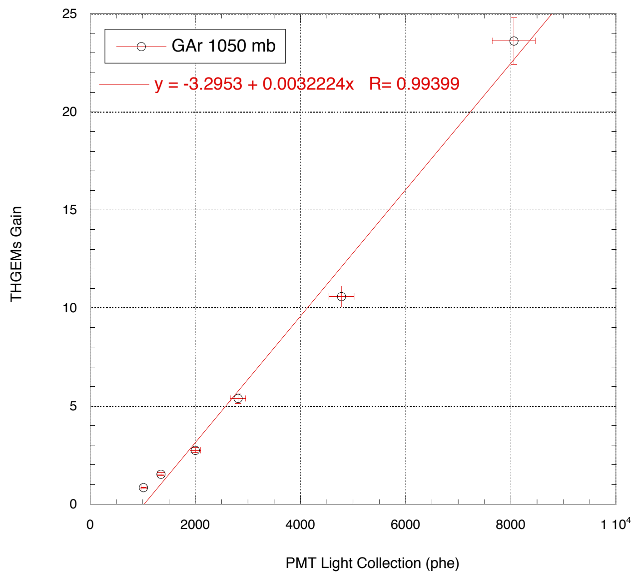

Figure 6.17: Correlation between THGEMs gain and PMT light collection. For THGEMs gain values higher than 25 the PMT was saturated and therefore no data are shown, although the highest gain in gaseous argon at ambient temperature was approximately 1000.

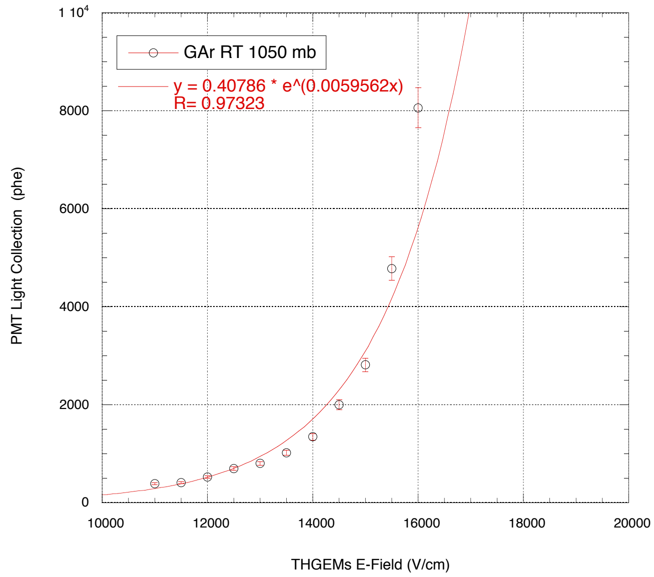

Figure 6.18: Variation of PMT light collection with THGEMs field. The PMT was saturated for fields higher than 16 kV/cm.

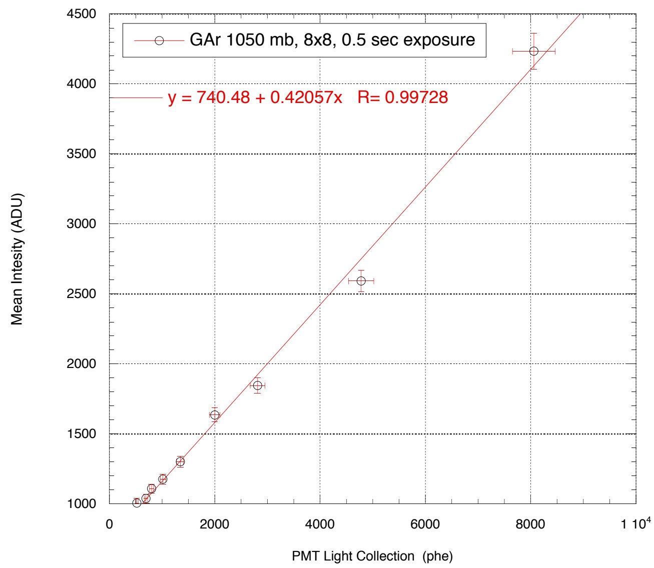

Figure 6.19: Correlation between PMT and CCD light collection. The mean intensity of the CCD refers to the Gaussian mean value from the image region that contains the alpha source.

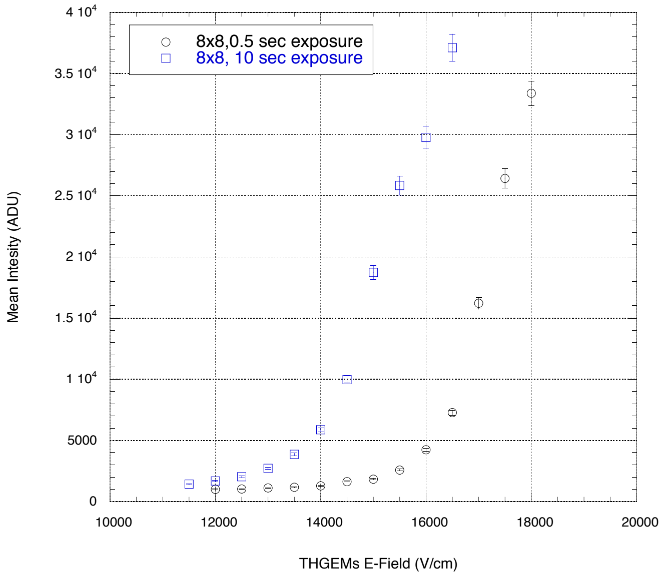

Figure 6.20: CCD mean intensity variation with THGEMs field for 0.5 and 10 sec exposure.

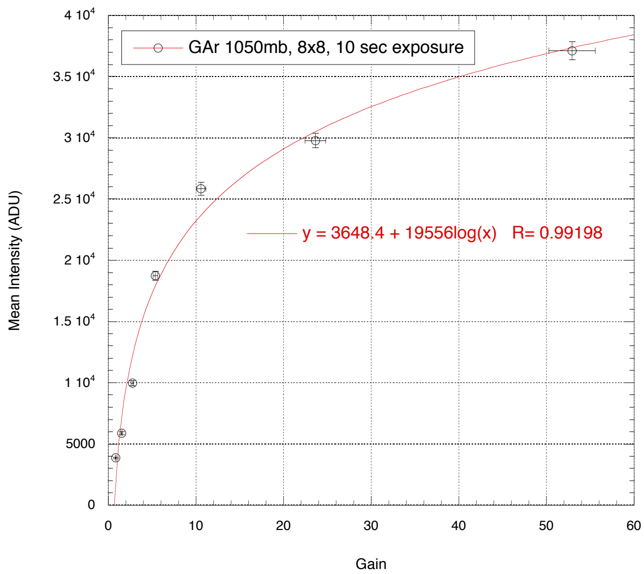

Figure 6.21: Correlation between CCD intensity and THGEMs gain. A gain of 1 corresponds to approximately 4000 ADU for a 10 sec exposure.

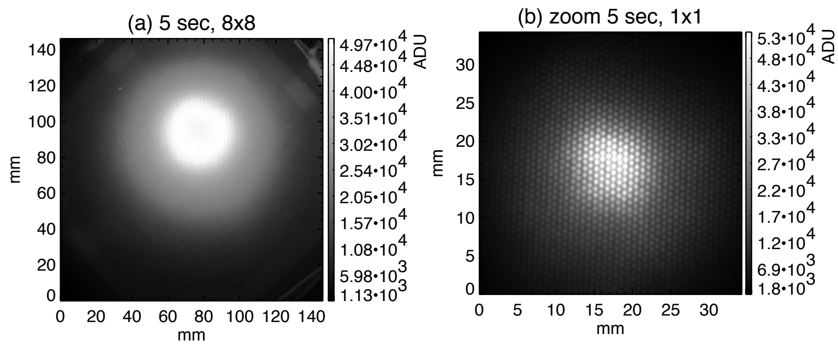

Figure 6.22: Images of the secondary scintillation light in ambient temperature and pure argon gas induced by Am-241 for a THGEM gain of 600. a) 8×8 binning and 5 sec exposure, illumination of the whole THGEM plane. b) A zoom of the alpha source region at a high 1×1 binning resolution and 5 sec exposure, the individual THGEM holes are clearly visible.

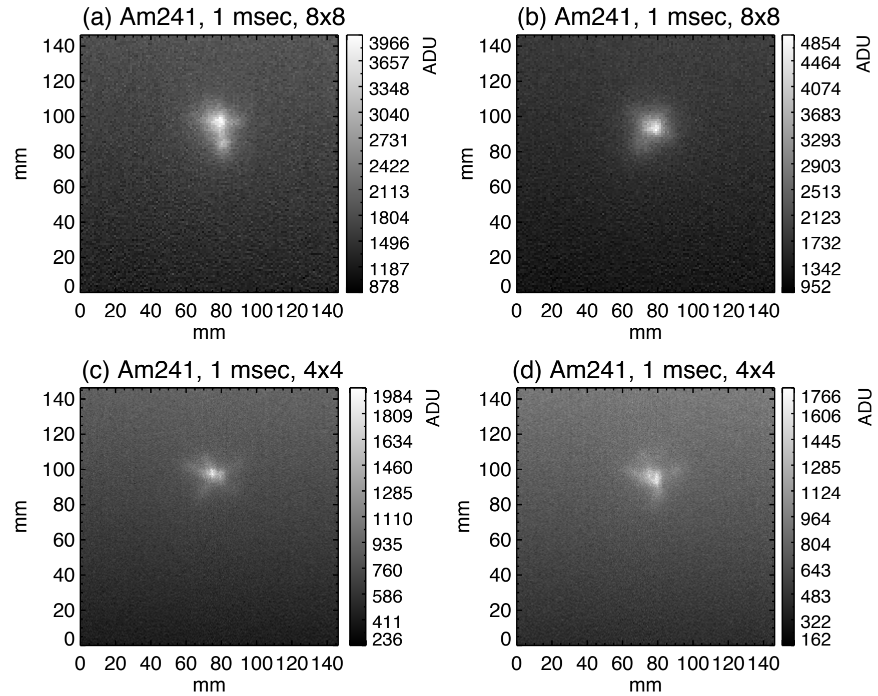

Figure 6.23: A gallery of alpha tracks in pure argon gas and ambient temperature. The electric field for both THGEMs was set to 18.5 kV/cm and the gain was approximately 1000. The top images were captured with 8×8 binning whereas the bottom ones with 4×4 binning.

6.5 Two Phase Operation

Following the successful operation in pure gas Argon at room temperature, and the characterisation of the CCD and the THGEM, we started the tests in cryogenic conditions. During the two phase operation the detector was submerged in liquid Argon and only the CCD cameras and the THGEM were operating in gas Argon environment, few degrees more than the rest of the detector.

Inside the electric field cage, the potential was constant at $0.5kV/cm$, and the speed of the electrons due to the electric field is $1.6mm/\mu s$ [73] [74], therefore the electrons take $125\mu s$ to cover the total distance from the electric field to the extraction grid. While for electrons generated $3cm$ below the extraction grid the time of travel is approximately $18.75\mu s$. The lifetime (τ), of the drifting electrons is highly dependant on LAr purity and can be approximated as a function of O_2 equivalent impurity concentration (ρ) [74] [75], as $\tau\ [\mu s] \approx 300/\rho[ppb]$. Therefore, a LAr purity level better than 2 ppb and 15 ppb is required for the drifting electrons to transit 20 cm and 3 cm respectively[72].

A purification system, through recirculation, was designed by the LAr lab and constructed in the workshop [66]. This component recirculated the liquid Argon and pass it through special designed copper filters to remove impurities. To achieve high purity first its important to minimise the outgassing of the components inside the vessel. For that the detector was left for a week with internal pressure $6\times10^{-7}mb$ using a vacuum pump at room temperature. Then the temperature was lowered at $-5°C$ with the same internal pressure and the vacuum pump still in operation, therefore any water molecules that remained froze inside the vessel.

The filling of the detector with liquid Argon lasted about 12 hours and through condensation, the gas Argon turned in to liquid. The detector sits inside a bath tank that we fill slowly with liquid Argon, thus the temperature of the detector drops gradually, until the surface of the liquid Argon inside the detector is about half way between the extraction grid and the other end of the THGEM. During the two phase operation the pressure is always monitored along with the temperature, using a thermocouple located behind the CCD camera. Also the performance of the THGEM is constantly evaluated in low temperatures using an Am-241 source, located in the middle of the field cage through the whole process.

It is important to mention that before applying high voltage to the drift cage with the custom made feedthroughs, inside the pipes where the wires are travelling through, liquid Argon was formed through condensation, and it functioned as an insulator, in order to prevent the wires from tripping with the metal pipe, since the air, is not an insulator for electric fields $3kV/cm$ and above.

6.6 Summary

Extraction of electrons produced by the Am-241 source was verified by observing the secondary electroluminescence light produced in the extraction region with the PMT. Further light production in the THGEM holes was achieved by increasing the electric field in the THGEMs. The maximum electric fields in the bottom and top THGEMs before discharges occurred were 41500 volts/cm and 22000 volts/cm respectively. With such electric fields we have captured the first images of an Am-241 source submerged in LAr using a CCD camera and 10 to 15 sec exposures as shown in Figure 6.24. Furthermore, a 15 sec exposure photograph of high rate gamma events produced by an external Cs-137 source illuminating the whole THGEM plane is shown in Figure 6.24. Figure 6.25 shows the light collection increase with bottom THGEM electric field variation recorded with the CCD camera using 8×8 binning and a 10 sec exposure. The CCD Gaussian mean intensity values reported here are solely for the pixels that contain the alpha source.

The secondary scintillation light is produced by the passage of electrons through noble gas within a linear electric field and as such is expected to increase linearly with the increase in the field up to a point. When a threshold in the electric field is passed the drifting electrons gain enough kinetic energy to ionise the atoms of the medium and subsequently initiate further multiplication known as avalanche, therefore there is an exponential relationship between charge multiplication (and so light) and electric field. As shown in Figure 6.25 the light increases exponentially with electric field indicating that we are within the avalanche region however, the gain based on the source could not be deter- mined due to the preamplifier noise.

The Microsoft HD-3000 webcam (model no:1456) was found to be the superior option of all the webcams tested in LAr and provided a very useful internal detector monitoring tool, allowing close observation of the LAr level during filling. Furthermore, the insight into the internal workings of the detector revealed that the LAr level remains constant and steady during recirculation allowing data collection whilst the pump was on.

Characterisation of the Sony ICX285AL CCD (table 6.3,6.4) chip in a cryogenic environment revealed a lowest operating temperature of -120 °C. To overcome this problem a heater was mounted on the back of the chip. There are however, more expensive alternative light sensitive chips that are guaranteed to operate to -200 °C such as those manufactured by e2v. In this setup the majority of the electronics such as the digitiser were mounted outside of the detector connected via a custom made Kapton cable thus limiting the components required to function in cryogenics to the chip. The VUV secondary scintillation light produced in the THGEM holes was converted to visible with a TPB coated perspex disk placed above the THGEMs allowing the use of economical conventional lenses.

The THGEMs and CCD camera performance was evaluated in argon gas ambient temperature. The highest THGEM gain reached was approximately 1000 and for such high gain individual alpha tracks were identifiable with a 1 msec exposure. When 5 sec exposures were taken the overall light was enough to light up the individual 500 μm THGEM holes. In two phase conditions accurate determination of the THGEM gain was not possible as the charge signal could not be separated from the preamplifier noise. However, for 10 sec exposures photographs of the secondary scintillation light produced by the Am-241 source in LAr were successfully captured. The light detected by the CCD was found to have an exponential increase with the THGEM electric field.

Now that we have demonstrated proof of concept, the next stage will be to investigate the capabilities of more light sensitive and ultra fast camera systems that would ultimately allow the time resolution of tracks. CCD chips are limited by a readout time of a few msecs however, some state of the art CMOS chip based cameras can record 10 μs exposures with 2 μs dead time between frames. It is likely that a custom system would need to be developed that allows for the electronics to be separated from the chip whilst still maintaining the high readout rate. As of June 2018 at the Liverpool Liquid argon lab a new 1 ton system is being built that will utilise 4 EMCCD cameras. The detector will be fully characterise at charged beam at CERN and will

Table 6.3: Artemis FS14 CCD PCB assembly characteristics.

CCD camera Artemis FS14	
CCD sensor type:	Sony ICX285AL
CCD sensor design:	Monochrom, Progressive scan, Interline transfer
Sensor dimensions:	8.98 mm$\times$ 6.71 mm, Diagonal 11.21 mm, 4:3, Type 2/3"
Pixel resolution (H$\times$V):	1391$\times$1039, 1.45 Megapixels
Pixel size:	6.45 μm $\times$ 6.45 μm
Full well capacity:	17.500 e^-
Typical Gain (temp dependant):	0.267 e^-/ADU
Read out noise (temp dependant):	3.7 e^-
Spectrum range:	300 nm - 1050 nm
Quantum efficiency at 430 nm:	50 %
Min exposure time:	1 msec
Dynamic range:	1:4730
ADC and data format:	16 bit, RAW Fits
Binning:	1$\times$1, 2$\times$2, 3$\times$3, 4$\times$4, 5$\times$5, 6$\times$6, 7$\times$7, 8$\times$8 via software
Data interface:	USB 2.0

validate further the optical readout technology.

Table 6.4: Sony ICX285AL CCD chip gain and Read Out Noise (RON) measurements.

CCD Gain at 28 °C (e^-/ADU)	CCD Gain at -100 °C (e^-/ADU)	CCD RON at 28 °C (ADU)	CCD RON at -100 °C (ADU)
0.32	0.27	28.30	16.50

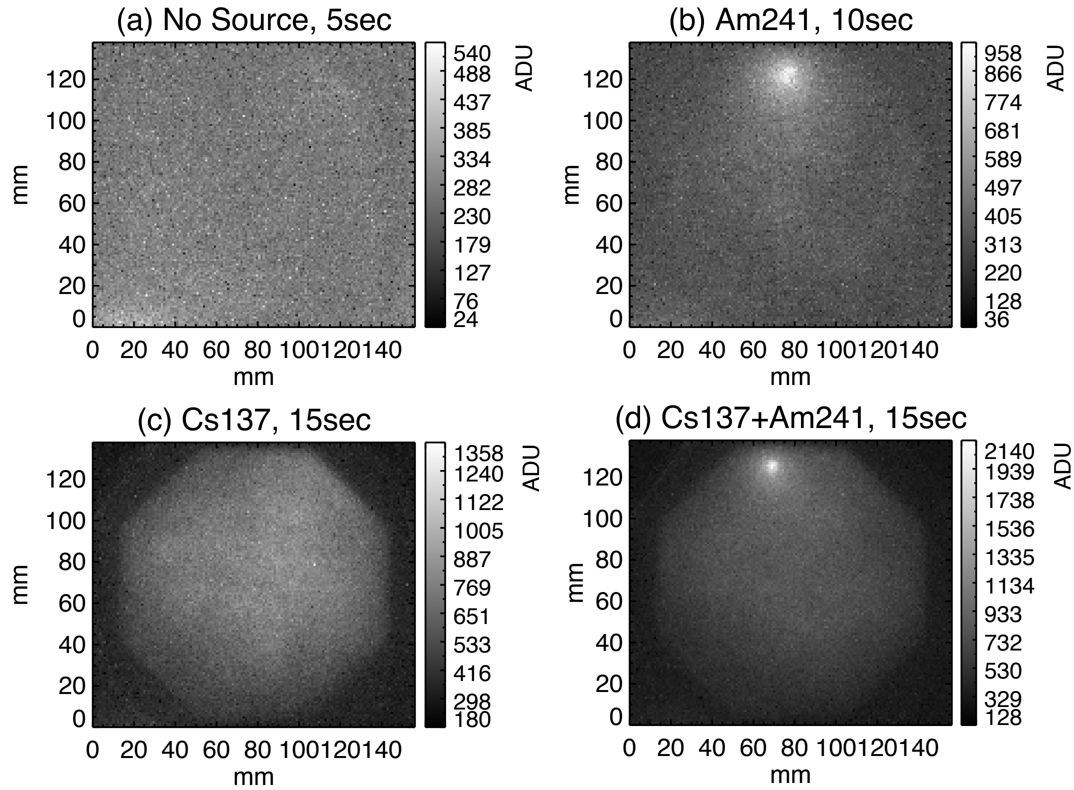

Figure 6.24: Images of the top THGEM in cryogenic two phase operation a) with no source, b) with the Am-241 source placed within the active region, c) with only the external Cs-137 source, d) with both the Am-241 source within the active region and the external Cs-137 source. For all four images the bottom THGEM field was set to 40 kV/cm while the top was set to 20 kV/cm. The gain of the THGEMs was estimated to be $\lesssim 45$ and the binning for all images was 8×8..

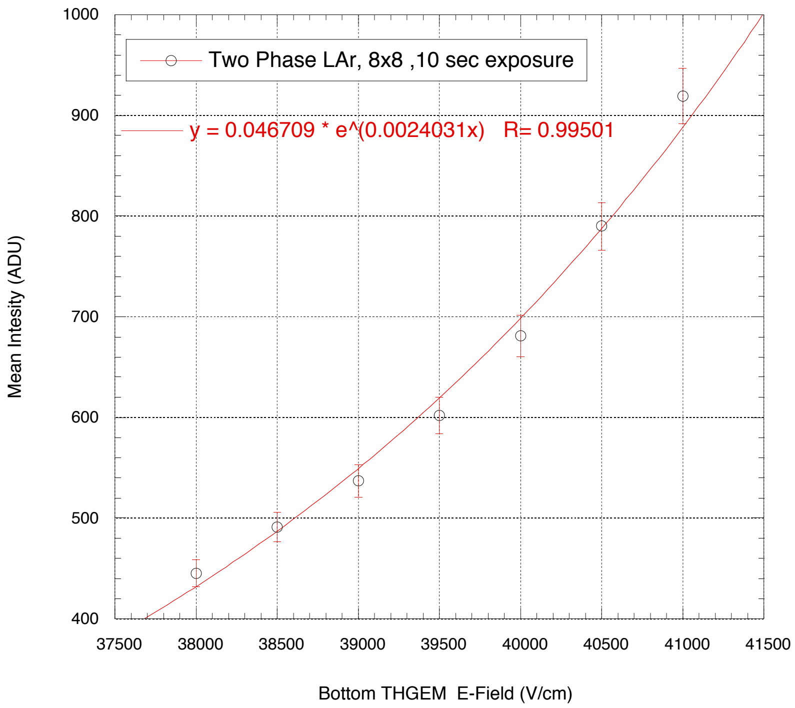

Figure 6.25: Variation of CCD intensity with bottom THGEM field in a two phase operation. The exposure was set to 10 sec and the binning was 8×8.

Conclusions

During my research as a post graduate, I have contributed to the T2K collaboration in multiple ways. While I was located in Japan, I was the ECal expert, responsible, for the good operation of the ECal. In addition, for my analysis, I have developed a neural network which is using the ECal to discriminate protons, and it is a tool available to everyone in the T2K, and nobody else have done before. I constructed a way to collect NCQES events, and it can be used for future NCQE cross section measurements, using new software and more recent MC. For this analysis I could not make cross section measurements, as I was using older MC (run 1-3). For every MC run, the method to calculate cross section systematics is different, as the MC is improving with time and the tools to calculate the systematics change. To evaluate cross section systematics, I had to re-run all the analysis from the beginning with new MC, which was an impossible task. For that reason I did not include any cross section errors, since the tools were not compatible with my MC. Though I have the required knowledge to calculate systematics, and make measurements using the MC and data.

The second part of my work, was in the LAr lab of the Liverpool University, and results of my work were published in two papers. During my first year, I have experimented with cameras in cryogenic environment, and proved it is possible to have operational cameras inside the detector, when it is filled with liquid Argon. It was a novelty, and we were the first lab to achieve that. The encouraging results of my work, helped to expand the detector and to order better more expensive cameras, with very high sensitivity, designed to operate in cryogenic environment. With the new cameras we were able to see alpha particles, and this lead to build the new 1 ton detector, Ariadne. Lastly, my work helped our LAr lab to move forward, and to participate in big future experiments, like the DUNE. With this, I conclude my thesis.

Bibliography

[1] J. N. Bahcall and M. H. Pinsonneault. What Do We (Not) Know Theoretically about Solar Neutrino Fluxes? *Physical Review Letters*, 92(12):121301, March 2004.

[2] SNO and et al ANTARES Collaboration. Measurement of atmospheric neutrino oscillations with the ANTARES neutrino telescope. *Physics Letters B*, 714:224–230, August 2012.

[3] IceCube Collaboration, M. G. Aartsen, M. Ackermann, J. Adams, J. A. Aguilar, M. Ahlers, M. Ahrens, D. Altmann, T. Anderson, C. Arguelles, and et al. Determining neutrino oscillation parameters from atmospheric muon neutrino disappearance with three years of IceCube DeepCore data. *ArXiv e-prints*, October 2014.

[4] K. Eguchi, S. Enomoto, K. Furuno, and J. et al. Goldman. First Results from KamLAND: Evidence for Reactor Antineutrino Disappearance. *Physical Review Letters*, 90(2), January 2003.

[5] A.K. Ichikawa. The t2k long-baseline neutrino experiment. Technical report, Department of Physics, Kyoto University, Kitashirakawa, Sakyo, Kyoto 606-8502,Japan., 2009.

[6] Super-K website admins. Super-kamiokande.

[7] E. Richard, K. Okumura, K. Abe, Y. Haga, Y. Hayato, and M. et al. Ikeda. Measurements of the atmospheric neutrino flux by Super-Kamiokande: Energy spectra, geomagnetic effects, and solar modulation. 94(5):052001, September 2016.

[8] Warwick University. Implementation of the second generation pid for the nd280 tracker ecals. 2012.

[9] Antony Carver. Particle identification in the nd280 electromagnetic calorimeter. 2009.

[10] D.P. Roy. Basic constituents of matter and their interactions a progress report. *TIFR/TH/99-59*, (1999).

[11] F.A. Scott. Energy spectrum of the beta-rays of radium e. *Phys. Rev.*, 48:391–395, 1935.

[12] C. Cowan et al. Detection of the free neutrino: A confirmation. *Science*, 124:103, 1956.

[13] F. Reines et al. Detection of the free anti-neutrino. *Phys. Rev.*, 117:159–173, 1960.

[14] G.Dandy et al. Observation of high-energy neutrino reactions and the existence of two kinds of neutrinos. *Phys. Rev.Lett*, 9:36–44, 1962.

[15] DONUT Collaboration, K. Kodama, N. Ushida, C. Andreopoulos, N. Saoulidou, G. Tzanakos, P. Yager, B. Baller, D. Boehnlein, W. Freeman, B. Lundberg, J. Morfin, R. Rameika, J. C. Yun, J. S. Song, C. S. Yoon, S. H. Chung, P. Berghaus, M. Kubantsev, N. W. Reay, R. Sidwell, N. Stanton, S. Yoshida, S. Aoki, T. Hara, J. T. Rhee, D. Ciampa, C. Erickson, M. Graham, K. Heller, R. Rusack, R. Schwienhorst, J. Sielaff, J. Trammell, J. Wilcox, K. Hoshino, H. Jiko, M. Miyanishi, M. Komatsu, M. Nakamura, T. Nakano, K. Niwa, N. Nonaka, K. Okada, O. Sato, T. Akdogan, V. Paolone, C. Rosenfeld, A. Kulik, T. Kafka, W. Oliver, T. Patzak, and J. Schneps. Observation of tau neutrino interactions. *Physics Letters B*, 504:218–224, April 2001.

[16] K. Sakurai, H. J. Haubold, and T. Shirai. The Variation of the Solar Neutrino Fluxes over Time in the Homestake, GALLEX(GNO) and Super-Kamiokande Experiments. *ArXiv e-prints*, November 2011.

[17] A. Bellerive, J. R. Klein, A. B. McDonald, A. J. Noble, and A. W. P. Poon. The Sudbury Neutrino Observatory. *Nuclear Physics B*, 908:30–51, July 2016.

[18] T. K. Gaisser and M. Honda. Flux of atmospheric neutrinos. *Annual Review of Nuclear and Particle Science*, 52:153–199, 2002.

[19] M. B. Smy, Y. Ashie, S. Fukuda, and at al. Fukuda. Precise measurement of the solar neutrino day-night and seasonal variation in Super-Kamiokande-I. 69(1):011104, January 2004.

[20] S. Fukuda, Y. Fukuda, and et al. Ishitsuka. Solar ^{8}B and hep Neutrino Measurements from 1258 Days of Super-Kamiokande Data. *Physical Review Letters*, 86:5651–5655, June 2001.

[21] M. B. Smy, Y. Ashie, S. Fukuda, and at al. Fukuda. Precise measurement of the solar neutrino day-night and seasonal variation in Super-Kamiokande-I. 69(1):011104, January 2004.

[22] T. Lasserre and H. W. Sobel. Reactor neutrinos. *Comptes Rendus Physique*, 6:749–757, September 2005.

[23] M. Apollonio, A. Baldini, C. Bemporad, and E. et al. Caffau. Search for neutrino oscillations on a long base-line at the CHOOZ nuclear power station. *European Physical Journal C*, 27:331–374, April 2003.

[24] F. Boehm, J. Busenitz, B. Cook, and et al. Gratta. Final results from the Palo Verde neutrino oscillation experiment. 64(11):112001, December 2001.

[25] F. P. An, J. Z. Bai, and et al. Balantekin. Observation of Electron-Antineutrino Disappearance at Daya Bay. *Physical Review Letters*, 108(17):171803, April 2012.

[26] B.Pontecorvo. Zh.eksp. *Teor.Fiz.*, 33:549, 1957.

[27] B.Pontecorvo. Sov.phys. *JETP*, 6:429, 1958.

[28] W. Yao et al. Review of particle physics. *Journal of physics G*, 33, 2006.

[29] Georgios Christodoulou. *A measurement of the electron neutrino component in the T2K beam using the tracker detectors and the electromagnetic calorimeter at the near detector ND280*. PhD thesis, Liverpool University, 2011.

[30] Daniel A. Dwyer. The neutrino mixing angle : Reactor and accelerator experiments. *Physics of the Dark Universe*, 4:31 – 35, 2014. {DARK} {TAUP2013}.

[31] C. Giunti and C.W. Kim. *Fundamentals of Neutrino Physics and Astrophysics*. OUP Oxford, 2007.

[32] G. Karagiorgi et al. Leptonic cp violation studies at miniboone in the (3+2) sterile neutrino oscillation hypothesis. *Phys. Rev.*, 2009.

[33] E. Fermi. Versuch einer Theorie der β-Strahlen. I. *Zeitschrift fur Physik*, 88:161–177, March 1949.

[34] T. D. Lee, M. Rosenbluth, and C. N. Yang. Interaction of mesons with nucleons and light particles. *Phys. Rev.*, 75:905–905, Mar 1949.

[35] M. M. Block et al. Phys. lett 1964, 12:281-285.

[36] S. P. Rosen. Symmetries and Conservation Laws in Neutrino Physics. In C. Baltay, editor, *Neutrinos - 1974*, volume 22 of *American Institute of Physics Conference Series*, pages 5–27, July 1974.

[37] P. L. Galison. *Part I. How Experiments End: Three Case Studies on the Interaction of Experiment and Theory in Twentieth - Physics. Part II. Large Weak Isospin and the W Mass.* PhD thesis, HARVARD UNIVERSITY., 1983.

[38] F. J. Hasert, S. Kabe, W. Krenz, J. Von Krogh, D. Lanske, J. Morfin, K. Schultze, H. Weerts, G. H. Bertrand-Coremans, J. Sacton, W. Van Doninck, P. Vilain, U. Camerini, D. C. Cundy, R. Baldi, I. Danilchenko, W. F. Fry, D. Haidt, S. Natali, P. Musset, B. Osculati, R. Palmer, J. B. M. Pattison, D. H. Perkins, A. Pullia, A. Rousset, W. Venus, H. Wachsmuth, V. Brisson, B. Degrange, M. Haguenauer, L. Kluberg, U. Nguyen-Khac, P. Petiau, E. Belotti, S. Bonetti, D. Cavalli, C. Conta, E. Fiorini, M. Rollier, B. Aubert, D. Blum, L. M. Chounet, P. Heusse,

A. Lagarrigue, A. M. Lutz, A. Orkin-Lecourtois, J. P. Vialle, F. W. Bullock, M. J. Esten, T. W. Jones, J. McKenzie, A. G. Michette, G. Myatt, and W. G. Scott. Observation of neutrino-like interactions without muon or electron in the gargamelle neutrino experiment. *Physics Letters B*, 46:138–140, September 1973.

[39] P. C. Bosetti, H. Deden, M. Deutschmann, P. Fritze, H. Grässler, F. J. Hasert, J. Morfin, H. Seyfert, R. Schulte, K. Schultze, K. Böckmann, H. Emans, C. Geich-Gimbel, R. Hartmann, A. Keller, T. P. Kokott, W. Meincke, B. Nellen, R. Pech, D. C. Cundy, J. Figiel, A. Grant, D. Haidt, P. O. Hulth, D. J. Kocher, D. R. O. Morrison, E. Pagiola, L. Pape, C. H. Peyrou, P. Porth, P. Schmid, W. G. Scott, H. Wachsmuth, K. L. Wernhard, S. Banerjee, K. W. J. Barnham, R. Beuselinck, I. Butterworth, E. F. Clayton, D. B. Miller, K. J. Powell, C. L. Davis, P. Grossmann, R. McGow, J. H. Mulvey, G. Myatt, D. H. Perkins, R. Pons, D. Radojicic, P. Renton, B. Saitta, V. Baruzzi, M. Bloch, M. De Beer, W. Hart, Y. Sacquin, B. Tallini, D. Vignaud, and Aachen-Bonn-CERN-London-Oxford-Saclay Collaboration. Analysis of nucleon structure functions in CERN bubble chamber neutrino experiments. *Nuclear Physics B*, 142:1–28, September 1978.

[40] F. J. Hasert et al. Observation of Neutrino Like Interactions without Muon or Electron in the Gargamelle Neutrino Experiment. *Nucl. Phys.*, B73:1–22, 1974.

[41] 37:348 D. Cline et al. Phys. Lett 1976.

[42] 37:252-255 D. Cline et al. Phys. Lett 1976.

[43] Won-Yong Lee et al. Observation of the Reaction Muon-neutrino p –> Muon-neutrino p. *Phys. Rev. Lett.*, 37:186–189, 1976.

[44] W. Freeman and D. Toussaint. Intrinsic strangeness and charm of the nucleon using improved staggered fermions. *Physics Review*, 88(5):054503, September 2013.

[45] J. Ashman et al. An Investigation of the Spin Structure of the Proton in Deep Inelastic Scattering of Polarized Muons on Polarized Protons. *Nucl. Phys.*, B328:1, 1989.

[46] K. Abe, J. Adam, H. Aihara, T. Akiri, and C. et al Andreopoulos. Measurement of the neutrino-oxygen neutral-current interaction cross section by observing nuclear deexcitation γ rays. *Phys. Rev. D*, 90:072012, Oct 2014.

[47] Jeremy Green, Nesreen Hasan, Stefan Meinel, Michael Engelhardt, Stefan Krieg, Jesse Laeuchli, John Negele, Kostas Orginos, Andrew Pochinsky, and Sergey Syritsyn. Up, down, and strange nucleon axial form factors from lattice QCD. 2017.

[48] W. Detmold, D. Pefkou, and P. E. Shanahan. Off-forward gluonic structure of vector mesons. 2017.

[49] C. H. Llewellyn Smith. Neutrino Reactions at Accelerator Energies. *Phys. Rept.*, 3:261–379, 1972.

[50] Maureen Caudill. *Neural Network Primer: Part I.* Miller Freeman, Inc, 1989.

[51] G. Cybenko. Approximation by superpositions of a sigmoidal function. *Math. Control Signals Systems*, 2:303–314, 1989.

[52] David Kriesel. *A Brief Introduction to Neural Networks*. 2007.

[53] P.-A. Amaudruz, M. Barbi, D. Bishop, N. Braam, D. G. Brook-Roberge, S. Giffin, S. Gomi, P. Gumplinger, K. Hamano, N. C. Hastings, S. Hastings, R. L. Helmer, R. Henderson, K. Ieki, B. Jamieson, I. Kato, N. Khan, J. Kim, B. Kirby, P. Kitching, A. Konaka, M. Lenckowski, C. Licciardi, T. Lindner, K. Mahn, E. L. Mathie, C. Metelko, C. A. Miller, A. Minamino, K. Mizouchi, T. Nakaya, K. Nitta, C. Ohlmann, K. Olchanski, S. M. Oser, M. Otani, P. Poffenberger, R. Poutissou, J.-M. Poutissou, W. Qian, F. Retiere, R. Tacik, H. A. Tanaka, P. Vincent, M. Wilking, S. Yen, and M. Yokoyama. The T2K fine-grained detectors. *Nuclear Instruments and Methods in Physics Research A*, 696:1–31, December 2012.

[54] F Dufour. L Haegel. T Linder. and S Ose. Systematics on out of-fiducial-volume background in the nd280 tracker.

[55] M. Friend et al. Flux prediction and uncertainty updates with na61 2009 thin target data and negative focussingmode predictions.

[56] K. Abe, N. Abgrall, H. Aihara, T. Akiri, J. B. Albert, C. Andreopoulos, S. Aoki, A. Ariga, T. Ariga, S. Assylbekov, D. Autiero, M. Barbi, G. J. Barker, G. Barr, M. Bass, M. Batkiewicz, F. Bay, S. W. Bentham, V. Berardi, B. E. Berger, S. Berkman, I. Bertram, D. Beznosko, S. Bhadra, F. d. M. Blaszczyk, A. Blondel, C. Bojechko, S. Boyd, A. Bravar, C. Bronner, D. G. Brook-Roberge, N. Buchanan, R. G. Calland, J. Caravaca Rodríguez, S. L. Cartwright, R. Castillo, M.-G. Catanesi, A. Cervera, D. Cherdack, G. Christodoulou, A. Clifton, J. Coleman, S. J. Coleman, G. Collazuol, K. Connolly, A. Curioni, A. Dabrowska, I. Danko, R. Das, S. Davis, M. Day, J. P. A. M. de André, P. de Perio, G. De Rosa, T. Dealtry, C. Densham, F. Di Lodovico, S. Di Luise, J. Dobson, T. Duboyski, F. Dufour, J. Dumarchez, S. Dytman, M. Dziewiecki, M. Dziomba, S. Emery, A. Ereditato, L. Escudero, L. S. Esposito, A. J. Finch, E. Frank, M. Friend, Y. Fujii, Y. Fukuda, V. Galymov, A. Gaudin, S. Giffin, C. Giganti, K. Gilje, T. Golan, J. J. Gomez-Cadenas, M. Gonin, N. Grant, D. Gudin, P. Guzowski, D. R. Hadley, A. Haesler, M. D. Haigh, D. Hansen, T. Hara, M. Hartz, T. Hasegawa, N. C. Hastings, Y. Hayato, C. Hearty, R. L. Helmer, J. Hignight, A. Hillairet, A. Himmel, T. Hiraki, J. Holeczek, S. Horikawa, K. Huang, A. Hyndman, A. K. Ichikawa, K. Ieki, M. Ieva, M. Ikeda, J. Imber, J. Insler, T. Ishida, T. Ishii, S. J. Ives, K. Iyogi, A. Izmaylov, B. Jamieson, R. A. Johnson, J. H. Jo, P. Jonsson, K. K. Joo, G. V. Jover-Manas, C. K. Jung, H. Kaji, T. Kajita, H. Kakuno, J. Kameda, Y. Kanazawa, D. Karlen, I. Karpikov, E. Kearns, M. Khabibullin, F. Khanam, A. Khotjantsev, D. Kielczewska, T. Kikawa, A. Kilinski, J. Y. Kim, J. Kim, S. B. Kim, B. Kirby, J. Kisiel, P. Kitching, T. Kobayashi, G. Kogan, A. Konaka, L. L. Kormos, A. Korzenev, K. Koseki, Y. Koshio, K. Kowalik, I. Kreslo, W. Kropp, H. Kubo, Y. Kudenko, S. Kumaratunga, R. Kurjata, T. Kutter, J. Lagoda, K. Laihem, A. Laing, M. Laveder, M. Lawe, K. P. Lee, C. Licciardi, I. T. Lim, T. Lindner, C. Lister, R. P. Litchfield, A. Longhin, G. D. Lopez, L. Ludovici, M. Macaire, L. Magaletti, K. Mahn, M. Malek, S. Manly, A. Marchionni, A. D.

Marino, J. Marteau, J. F. Martin, T. Maruyama, J. Marzec, P. Masliah, E. L. Mathie, C. Matsumura, K. Matsuoka, V. Matveev, K. Mavrokoridis, E. Mazzucato, N. McCauley, K. S. McFarland, C. McGrew, T. McLachlan, M. Messina, C. Metelko, M. Mezzetto, P. Mijakowski, C. A. Miller, A. Minamino, O. Mineev, S. Mine, A. Missert, M. Miura, L. Monfregola, S. Moriyama, Th. A. Mueller, A. Murakami, M. Murdoch, S. Murphy, J. Myslik, T. Nagasaki, T. Nakadaira, M. Nakahata, T. Nakai, K. Nakajima, K. Nakamura, S. Nakayama, T. Nakaya, K. Nakayoshi, D. Naples, T. C. Nicholls, C. Nielsen, K. Nishikawa, Y. Nishimura, H. M. O'Keeffe, Y. Obayashi, R. Ohta, K. Okumura, W. Oryszczak, S. M. Oser, M. Otani, R. A. Owen, Y. Oyama, M. Y. Pac, V. Palladino, V. Paolone, D. Payne, G. F. Pearce, O. Perevozchikov, J. D. Perkin, E. S. Pinzon Guerra, P. Plonski, E. Poplawska, B. Popov, M. Posiadala, J.-M. Poutissou, R. Poutissou, P. Przewlocki, B. Quilain, E. Radicioni, P. N. Ratoff, M. Ravonel, M. A. Rayner, M. Reeves, E. Reinherz-Aronis, F. Retiere, P. A. Rodrigues, E. Rondio, B. Rossi, S. Roth, A. Rubbia, D. Ruterbories, R. Sacco, K. Sakashita, F. Sánchez, E. Scantamburlo, K. Scholberg, J. Schwehr, M. Scott, D. I. Scully, Y. Seiya, T. Sekiguchi, H. Sekiya, M. Shibata, M. Shiozawa, S. Short, Y. Shustrov, P. Sinclair, B. Smith, R. J. Smith, M. Smy, J. T. Sobczyk, H. Sobel, M. Sorel, L. Southwell, P. Stamoulis, J. Steinmann, B. Still, R. Sulej, A. Suzuki, K. Suzuki, S. Y. Suzuki, Y. Suzuki, T. Szeglowski, M. Szeptycka, R. Tacik, M. Tada, S. Takahashi, A. Takeda, Y. Takeuchi, H. A. Tanaka, M. Tanaka, M. M. Tanaka, I. J. Taylor, D. Terhorst, R. Terri, L. F. Thompson, A. Thorley, S. Tobayama, W. Toki, T. Tomura, Y. Totsuka, C. Touramanis, T. Tsukamoto, M. Tzanov, Y. Uchida, K. Ueno, A. Vacheret, M. Vagins, G. Vasseur, T. Wachala, A. V. Waldron, C. W. Walter, J. Wang, D. Wark, M. O. Wascko, A. Weber, R. Wendell, G. Wikström, R. J. Wilkes, M. J. Wilking, C. Wilkinson, Z. Williamson, J. R. Wilson, R. J. Wilson, T. Wongjirad, Y. Yamada, K. Yamamoto, C. Yanagisawa, T. Yano, S. Yen, N. Yershov, M. Yokoyama, T. Yuan, A. Zalewska, L. Zambelli, K. Zaremba, M. Ziembicki, E. D. Zimmerman, M. Zito, and J. Żmuda. T2k neutrino flux prediction. *Phys. Rev. D*, 87:012001, Jan 2013.

[57] Arie Bodek and J L. Ritchie. Fermi-motion effects in deep-inelastic lepton scattering from nuclear targets. 23, 03 1981.

[58] F Dufour. L Haegel. T Lindner. and S Oser. Systematics on out of-fiducial-volume backgrounds in the nd280 tracker.

[59] J. Lagoda K. Kowalik. The simulations of the beam neutrinos interactions outside the nd280 detector.

[60] L. Haegel and for the T2K Collaboration. T2K near detector constraints for oscillation results. *ArXiv e-prints*, January 2017.

[61] K. Abe, T. Abe, H. Aihara, Y. Fukuda, Y. Hayato, K. Huang, A. K. Ichikawa, M. Ikeda, K. Inoue, H. Ishino, Y. Itow, T. Kajita, J. Kameda, Y. Kishimoto, M. Koga, Y. Koshio, K. P. Lee, A. Minamino, M. Miura, S. Moriyama, M. Nakahata, K. Nakamura, T. Nakaya, S. Nakayama, K. Nishijima, Y. Nishimura, Y. Obayashi, K. Okumura, M. Sakuda, H. Sekiya, M. Shiozawa, A. T. Suzuki, Y. Suzuki, A. Takeda, Y. Takeuchi, H. K. M. Tanaka, S. Tasaka, T. Tomura, M. R. Vagins, J. Wang, and M. Yokoyama. Letter of Intent: The Hyper-Kamiokande Experiment — Detector Design and Physics Potential —. *ArXiv e-prints*, September 2011.

[62] R. Acciarri, M. A. Acero, M. Adamowski, C. Adams, P. Adamson, S. Adhikari, Z. Ahmad, C. H. Albright, T. Alion, E. Amador, and et al. Long-Baseline Neutrino Facility (LBNF) and Deep Underground Neutrino Experiment (DUNE) Conceptual Design Report Volume 1: The LBNF and DUNE Projects. *ArXiv e-prints*, January 2016.

[63] R. Acciarri, M. A. Acero, M. Adamowski, C. Adams, P. Adamson, S. Adhikari, Z. Ahmad, C. H. Albright, T. Alion, E. Amador, and et al. Long-Baseline Neutrino Facility (LBNF) and Deep Underground Neutrino Experiment (DUNE) Conceptual Design Report, Volume 4 The DUNE Detectors at LBNF. *ArXiv e-prints*, January 2016.

[64] DUNE Collaboration, R. Acciarri, M. A. Acero, M. Adamowski, C. Adams, P. Adamson, S. Adhikari, Z. Ahmad, C. H. Albright, T. Alion, and et al. Long-Baseline Neutrino Facility (LBNF) and Deep Underground Neutrino Experiment (DUNE) Conceptual Design Report Volume 2: The Physics Program for DUNE at LBNF. *ArXiv e-prints*, December 2015.

[65] A. Marchionni. Status and New Ideas Regarding Liquid Argon Detectors. *Annual Review of Nuclear and Particle Science*, 63:269–290, October 2013.

[66] K. Mavrokoridis, R. G. Calland, J. Coleman, P. K. Lightfoot, N. McCauley, K. J. McCormick, and C. Touramanis. Argon purification studies and a novel liquid argon re-circulation system. *Journal of Instrumentation*, 6:8003, August 2011.

[67] C. Cantini, L. Epprecht, A. Gendotti, S. Horikawa, L. Periale, S. Murphy, G. Natterer, C. Regenfus, F. Resnati, F. Sergiampietri, A. Rubbia, T. Viant, and S. Wu. Performance study of the effective gain of the double phase liquid Argon LEM Time Projection Chamber. *Journal of Instrumentation*, 10:P03017, March 2015.

[68] Dr Kostas Mavrokoridis. Optical readout of a two phase liquid argon tpc using ccd camera and thgem. *NNN2014, Paris, November 2014*, 2014.

[69] M. Antonello and et al. Baibussinov. Experimental observation of an extremely high electron lifetime with the ICARUS-T600 LAr-TPC. *Journal of Instrumentation*, 9:P12006, December 2014.

[70] A. Breskin, R. Alon, M. Cortesi, R. Chechik, J. Miyamoto, V. Dangendorf, J. M. Maia, and J. M. F. Dos Santos. A concise review on THGEM detectors. *Nuclear Instruments and Methods in Physics Research A*, 598:107–111, January 2009.

[71] K. Mavrokoridis, K. J. McCormick, M. Nessi, A. Roberts, N. A. Smith, and C. Touramanis. Letter of Intent: ARIADNE, a Photographic LAr TPC at the CERN Neutrino Platform. *CERN record*, 2016.

[72] K. Mavrokoridis, F. Ball, J. Carroll, M. Lazos, K. J. McCormick, N. A. Smith, C. Touramanis, and J. Walker. Optical readout of a two phase liquid argon TPC

using CCD camera and THGEMs. *Journal of Instrumentation*, 9:P02006, February 2014.

[73] W. Walkowiak. Drift velocity of free electrons in liquid argon. *Nuclear Instruments and Methods in Physics Research Section A: Accelerators, Spectrometers, Detectors and Associated Equipment*, 449(1–2):288 – 294, 2000.

[74] S Amoruso and M Antonello et al. Analysis of the liquid argon purity in the icarus t600 tpc. *Nuclear Instruments and Methods in Physics Research Section A*, 516(1):68 – 79, 2004.

[75] E. Aprile, K.L. Giboni, and C. Rubbia. A study of ionization electrons drifting large distances in liquid and solid argon. *Nuclear Instruments and Methods in Physics Research Section A: Accelerators, Spectrometers, Detectors and Associated Equipment*, 241(1):62 – 71, 1985.